Published for the International Glaciological Society

THIS MANUSCRIPT HAS BEEN SUBMITTED TO THE JOURNAL OF GLACIOLOGY AND HAS NOT BEEN PEER-REVIEWED.

Progression of the surge in the Negribreen Glacier System from two years of ICESat-2 measurements

Journal:	*Journal of Glaciology*
Manuscript ID	Draft
Manuscript Type:	Article
Date Submitted by the Author:	n/a
Complete List of Authors:	Trantow, Thomas; University of Colorado Boulder, Herzfeld, Ute; University of Colorado Boulder
Keywords:	Glacier surges, Remote sensing, Crevasses, Laser altimetry, Arctic glaciology
Abstract:	The unique measurement capabilities of ICESat-2 allow high spatiotemporal resolution of complex ice-dynamic processes that occur during a surge. Detailed and precise mapping of height changes on surge glaciers has previously escaped observations from space due to limited resolution of space-borne altimeter data and the surface characteristics of glaciers during surge such as heavy crevassing. This makes geophysical interpretation of deformation and assessment of mass transfer difficult. In this paper, we present an approach that facilitates analysis of the evolution of geophysical processes during a surge, including height changes, crevassing, mass transfer and roughness evolution. We utilize all data from 2 years of ICESat-2 observations collected during the mature phase of the Negribreen Glacier System (NGS) surge in 2019 and 2020. The progression of the NGS surge has resulted in large-scale elevation changes and wide-spread crevassing making it an ideal case study to demonstrate ICESat-2 measurement capabilities, which are maximized when coupled with the Density Dimension Algorithm for Ice (DDA-ice). Results show the expansion of the surge in upper Negribreen which demonstrates the unique ability of ICESat-2/DDA-ice to measure a rapidly changing surge glacier and

	provide the best estimates for cryospheric changes and their contributions to sea-level rise.

SCHOLARONE™
Manuscripts

Journal of Glaciology, Vol. 00, No. 000, 0000 1

Progression of the surge in the Negribreen Glacier System from two years of ICESat-2 measurements

Thomas TRANTOW,[1] Ute C. HERZFELD,[1]

[1] *Department of Electrical, Energy and Computer Engineering, University of Colorado, Boulder, Colorado, USA*

Correspondence: Thomas Trantow <trantow@colorado.edu>

For Peer Review

ABSTRACT. The unique measurement capabilities of ICESat-2 allow high spatiotemporal resolution of complex ice-dynamic processes that occur during a surge. Detailed and precise mapping of height changes on surge glaciers has previously escaped observations from space due to limited resolution of space-borne altimeter data and the surface characteristics of glaciers during surge such as heavy crevassing. This makes geophysical interpretation of deformation and assessment of mass transfer difficult. In this paper, we present an approach that facilitates analysis of the evolution of geophysical processes during a surge, including height changes, crevassing, mass transfer and roughness evolution. We utilize all data from 2 years of ICESat-2 observations collected during the mature phase of the Negribreen Glacier System (NGS) surge in 2019 and 2020. The progression of the NGS surge has resulted in large-scale elevation changes and wide-spread crevassing making it an ideal case study to demonstrate ICESat-2 measurement capabilities, which are maximized when coupled with the Density Dimension Algorithm for Ice (DDA-ice). Results show the expansion of the surge in upper Negribreen which demonstrates the unique ability of ICESat-2/DDA-ice to measure a rapidly changing surge glacier and provide the best estimates for cryospheric changes and their contributions to sea-level rise.

1. INTRODUCTION

1.1. Glacier Surging: Relevance, Complexity and Observation from Space

Processes of ice-dynamic instability, such as glacial acceleration, have been identified by the Intergovernmental Panel of Climate Change (IPCC, AR6, Chen and others (2021)) as a source of "deep uncertainty" in our understanding of ice sheet and glacier evolution and their contribution to future sea-level rise. Glacier surging is a type of glacial acceleration and is poorly understood due to surges being relatively rare events with dramatic ice deformation occurring on short timescales resulting in a paucity of comprehensive observations. The lack of surge observations, particularly those at resolution high enough to resolve the complex surge processes, limits our community's ability to analyze this important phenomenon (Clarke, 1987; Truffer and Echelmeyer, 2003; Mayer and Herzfeld, 2000; Jiskoot, 2011; Herzfeld and others, 2013a).

A surge-type glacier will cycle quasi-periodically between a long quiescent phase of normal flow and a short surge phase when flow speeds rapidly accelerate by a factor of 10 to 200. Negribreen, a large glacier in eastern Spitsbergen, Svalbard, began to surge in 2016 for the first time in over 70 years (Lefauconnier and Hagen, 1991; Strozzi and others, 2017; Herzfeld and others, 2021). Negribreen continues to surge through 2023, though it is gradually decelerating from its peak velocities in 2017 (Haga and others, 2020; Herzfeld and others, 2022). A feed-back system of acceleration, crevassing and ice-ocean interaction has already led to accelerated mass loss of the Negribreen Glacier System (NGS). There is a possibility that the Negribreen surge may trigger pervasive mass loss and a potential disintegration of the entire glacier system, similar to the collapse of the Vavilov Ice Cap in the Russian Arctic (Willis and others, 2018).

Surges are limited geographically to particular regions of the cryosphere, clustered mostly in Alaska/Yukon, Svalbard, high mountain Asia and around the periphery of the major ice sheets (Dolgushin and Osipova, 1975; Kamb and others, 1985; Kamb, 1987; Björnsson, 1998; Molnia and Post, 1995; Herzfeld and Mayer, 1997; Mayer and Herzfeld, 2000; Murray and others, 2003; Björnsson and others, 2003; Truffer and Echelmeyer, 2003; Jiskoot and others, 2003; Jiskoot, 2011; Flowers and others, 2011; Lee and others, 2013; Sevestre and others, 2015; Bhambri and others, 2017; Trantow and Herzfeld, 2018; Kochtitzky and others, 2020; Vale and others, 2021; Banerjee and others, 2022; Yao and others, 2023; Guillet and others, 2022). While new satellite technologies have allowed detection of over 100 surge-type events from 2017-2022 (Kääb and others, 2023), very few of these events have received dedicated studies that map and document individual surges making investigation of surge mechanisms and processes a data-starved problem.

For Peer Review

Geophysical processes that are characteristic of a surge include rapid acceleration, crevassing, mass transfer within the glacier, advance of the ice front, and changes in the internal hydrological system of the glacier (Meier and Post, 1969; Kamb, 1987; Harrison and Post, 2003; Truffer and others, 2021). The first four characteristics in particular are best and most directly observed with altimetry. However, observations of surge glaciers from space are usually limited to radar imagery (e.g., Luckman and others (2002); Murray and others (2003); Guan and others (2022); Wuite and others (2022); Kääb and others (2023)), which typically focus on velocity analysis yet lack the spatial resolution to resolve crevasses, and field measurements (e.g., Kamb and others (1985); Björnsson and others (2003); Herzfeld and others (2013b, 2022)), which are rare and often lack spatial and temporal coverage.

Detailed and precise mapping of height changes of surge glaciers has previously escaped observations of space, because of limited resolution of space-borne altimeter data and heavy crevassing of the ice surface as is characteristic during a surge. This makes geophysical interpretation of deformation and assessment of mass transfer difficult.

In this paper, we present an approach that facilitates analysis of the evolution of geophysical processes during a surge, including height changes, crevassing, mass transfer in the glacier and roughness evolution. We utilize all data from 2 years of ICESat-2 observations collected during the mature phase of the Negribreen surge in 2019 and 2020. The unique measurement capabilities of ICESat-2 allows resolution of the complex ice-dynamic processes that occur during a surge in space and time in an altimeter data set.

1.2. The Study Area: Negribreen, Svalbard

The Negribreen Glacier System, a large glacier system in Arctic Svalbard (Figure 1(a)), surged in late 2016 reaching speeds of 21m/day during its peak in July 2017, equivalent to 200 times its normal quiescent velocity (Strozzi and others, 2017; Herzfeld and others, 2021). In response to this rare event, the author's Geomathematics, Remote Sensing and Cryospheric Sciences Group at the University of Colorado, Boulder, conducted three airborne survey campaigns of the glacier system in the summers of 2017, 2018 and 2019 (Herzfeld and others, 2022), whose data supplements the analysis in this paper (see Section 2.2).

The NGS consists of Negribreen, where the majority of the surge activity occurs, Rembebreen, a southern tributary glacier in the upper glacier system, and two main tributary glaciers flowing in from the north: Akademikarbreen feeding Negribreen in the upper glacier, and Ordonnansbreen further down-glacier (Figure 2). The NGS receives large amounts of inflowing ice from the Filchnerfonna accumulation zone above the NGS to the west. The divide between Filchnerfonna and the NGS as we have defined it in this paper

For Peer Review

is somewhat arbitrary as the two ice masses are connected by a series of glaciers and ice falls (e.g., Transparentbreen) and are dynamically connected, which we show in this paper. However, the vast majority of the surge activity, particularly in 2019 and 2020, occurs below the Filchnerfonna and as such we define the bounds of the NGS using the black line in Figure 2, which excludes Filchnerfonna.

Negribreen consists of polythermal ice and is marine-terminating and thus the mechanisms leading to surge behavior, along with surge evolution as a whole, differs from a surge in a temperate and/or land-terminating glacier such Bering Glacier, Alaska (Dowdeswell and others, 1984; Murray and others, 2003; Trantow, 2020). Similar to other observed surges in tidewater glaciers in Svalbard (Strozzi and others, 2017; Nuth and others, 2019), Negribreen began accelerating near the terminus after a collapse in the frontal area (location indicated in Figure 1(b))), and surge effects, such as crevassing and increased velocities, propagated upglacier affecting other parts of the greater Negribreen Glacier System (Herzfeld and others, 2021; Haga and others, 2020). High velocities and enhanced calving occurring during the surge has led to massive mass loss in the system, which has contributed to sea-level rise.

The mass loss and disintegration of the glacier system is immediately apparent by examining the time series of Landsat-8 imagery in Figure 1 from 2018-2021 (RGB imagery at 30 m resolution, Roy and others (2014)). The NGS terminus has seen massive deformation with the "tooth" of Ordonnansbreen becoming completely detached from the main system by 2021 (see Fig. 1(e)). Detailed altimeter documentation of the Ordonnansbreen tooth detachment is provided by the ICESat-2/DDA-ice time series in Section 4.3.3.

1.3. ICESat-2 and the DDA-ice

NASA's ICESat-2 satellite, launched on 15 September 2018, provides high-resolution height measurements of ice sheets and glaciers via its state-of-the-art micro-pulse photon-counting lidar technology (Markus and others, 2017; Neumann and others, 2019). ICESat-2's payload, the Advanced Topographic Laser Altimeter System (ATLAS), provides height observations at 0.7 m along-track-resolution, a significant upgrade to its predecessor, ICESat's Geoscience Laser Altimeter System (GLAS), which provided height estimates every 173 m along-track from 2003-2009 (Zwally and others, 2002).

ATLAS operates at 532 nm (green light) and consists of 3 pairs of strong and weak beams with each pair separated by 3.3 km in the across-track direction (Neumann and others, 2019; Martino and others, 2019). Each strong beam is separated from its weak counterpart by 90 m across-track and 2.5 km along-track. The ratio of transmit energies between strong and weak is approximately 4:1 in order to compensate for varying surface reflectance. The transmitter array rotates its orientation approximately every 6-months so

For Peer Review

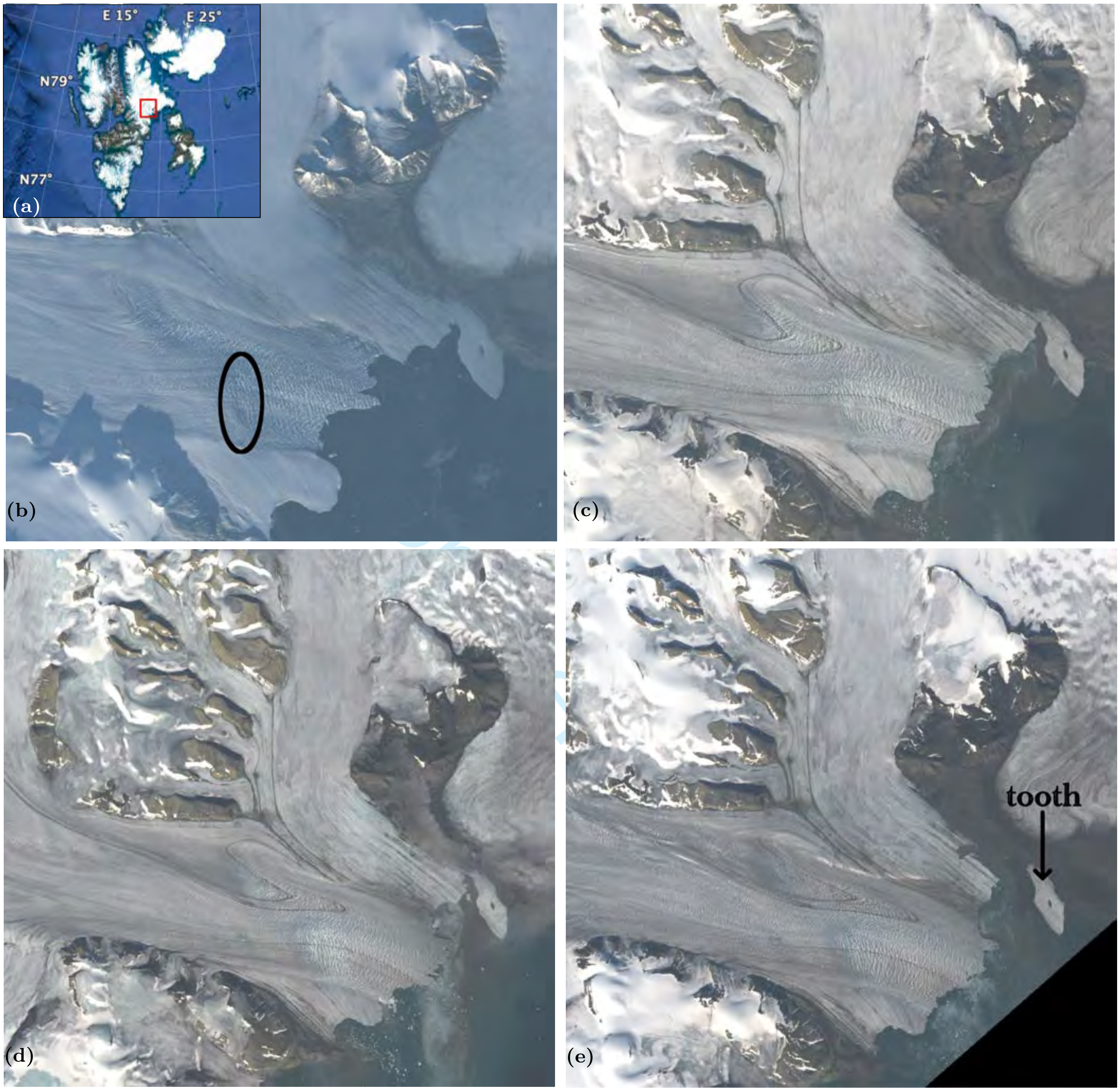

Fig. 1. Landsat-8 images of the Negribreen Glacier System 2018-2021. Location of the Negribreen Glacier System (red box) within the Svalbard archipelago. Landsat-8 RGB imagery (30 m resolution) acquired (b) 2018-09-30 with the location of the surface collapse that initiated the surge circled in black, (c) 2019-08-20, (d) 2020-07-31 and (e) 2021-08-08 with Ordanonnsbreen's tooth indicated by the black arrow.

that either the weak beams lead (flying "forwards", spacecraft orientation = 1), or the strong-beams lead (flying "backwards", spacecraft orientation = 0)(see Figure 3 and Table 1 of Herzfeld and others (2021)).

ICESat-2 flies at ~500 km altitude and orbits in a 92° inclination, thus providing measurements up to ±88° latitude. The satellite flies in an exact 91-day repeat cycle and is divided into 1387 reference ground tracks (RGTs) (Neumann and others, 2019, 2020b). All-in-all, ICESat-2 provides 6 measurement opportunities across a 6.6 km swath every 70 cm along its flight path, repeating every 91-days.

Several factors limit the ideal spatiotemporal measurement resolution of ICESat-2 in the cryosphere, the most significant being cloud cover through which green-light is severely attenuated. Other factors contributing to weak or non-existent return signals over ice include diffuse scattering, the presence of water or dirt, and pre-scheduled satellite maneuvers that either pause active measurement for maintenance or calibration purposes, or point the instrument off its normal track in order to better capture a particular phenomenon (Luthcke and others, 2021; Magruder and others, 2021). Signals are further complicated by noise emanating from the solar background or from the instrument itself (Martino and others, 2019). Furthermore, NASA's official ice-surface height product ATL06 (Smith and others, 2020), only resolves surface heights with 40 m postings at 20 m spacing and does not take full advantage of the high-resolution capabilities of ICESat-2 (Herzfeld and others, 2021).

The Density-Dimension Algorithm for Ice Surfaces (DDA-ice), however, fully exploits ICESat-2's measurement capabilities by identifying height-signals at the native resolution of 70 cm (Herzfeld and others, 2017, 2021). At this resolution, important geophysical processes can be measured such as crevassing, calving and rifting (Herzfeld and others, 2021). In the present study, we employ the DDA-ice algorithm in order to maximize ICESat-2's ability to capture geophysical processes in a rapidly changing glacier system that is actively surging.

For Peer Review

2. DATA

2.1. ICESat-2 ATL03 Data

The DDA-ice algorithm takes as input the ATLAS/ICESat-2 L2A Global Geolocated Photon Data (ATL03) (Neumann and others, 2020b). We use release 4 (revision 1) of these data in this analysis (Neumann and others, 2020a). The ATL03 data give height above the WGS 84 ellipsoid (ITRF2014 reference frame) along with latitude, longitude and time for all the photons downlinked from ICESat-2.

ATL03 data are segmented by granules that each cover 1/14th of a single orbit. Granules are given in HDF5 format and are freely available through NASA or from the National Snow and Ice Data Center (NSIDC). Granules are named using the format ATL03_[yyyymmdd][hhmmss]_[ttttccss]_[vvv_rr].h5, where[yyyymmdd][hhmmss] is the date and time of acquisition associated with the first data point in the granule, [tttt] is the reference ground track (RGT) number, [cc] the cycle number, [ss] the segment number and [vvv_rr] the version and revision numbers.

For our analysis of Negribreen, we attain all granules covering the NGS between 1 January 2019 and 31 December 2020. With the NGS lying between latitudes 78.5°N 78.8°N, the segment number is equal to either 03 if the satellite as ascending during data collection or equal to 05 if the satellite is descending. The cycle number identifies the number of 91-day cycles that have elapsed since ICESat-2 entered its science orbit. Our analysis here uses data that spans eight cycles from cycle 02 to cycle 09. Each cycle is divided into 1387 unique Reference Ground Tracks (RGTs). There are 9 RGTs that provide significant data coverage of the NGS: 91, 152, 389, 450, 594, 831, 892, 1036 and 1334. Nine RGTs spanning 8 cycles equates to 72 granules for this two-year analysis. With all six beams covering part of the glacier system for each RGT, we process a total of 432 measurement passes in this analysis. The specific granules used in this analysis are identified in the Supplementary Material (negri_data_2019_2020.xlsx).

ICESat-2's six beams are labeled as gt1l, gt2l, gt3l, gt1r, gt2r and gt3r. The strong beams can be associated with either the left (l) or right (r) side depending on the orientation of the ICESat-2 observatory, which switches every six months or so in order to maximize the solar illumination of the solar panels. At the beginning of 2019, ATLAS was in its "backward" orientation with left ground tracks corresponding to strong beams and right ground tracks corresponding to weak beams. ATLAS switched to its "forward" orientation in September 2019 resulting in strong beam identification by the right ground tracks. A switch back to the "backwards" orientation occurred in June 2020.

2.2. Airborne Altimeter and Image Data

We collected airborne altimeter data in the summers of 2017, 2018 and 2019 as part of a campaign to document the surge of Negribreen (Herzfeld and others, 2022; Herzfeld and Trantow, 2021). Our analysis here utilizes the data collected during the 2019 campaign, which under-flew several ICESat-2 tracks in upper Negribreen on 13 August 2019.

For the 2019 campaign, height measurements were attained using a LaserTech Universal Laser System (ULS) instrument that operates at 905 nm. The ULS was used in conjunction with a 1-Hz LORD 3DM-GX5-15 Virtual Reference Unit, i.e. an IMU, along with a 10-Hz Trimble R10 rover GPS in order to attain accurate height estimates. Both the ULS and GPS were attached the skids of a helicopter which was flown 100-200 m above the ice surface during operation of the laser. With an effective measurement rate of 400 Hz, the ULS provided glacier surface heights every 0.06-0.08 m along-track.

For Peer Review

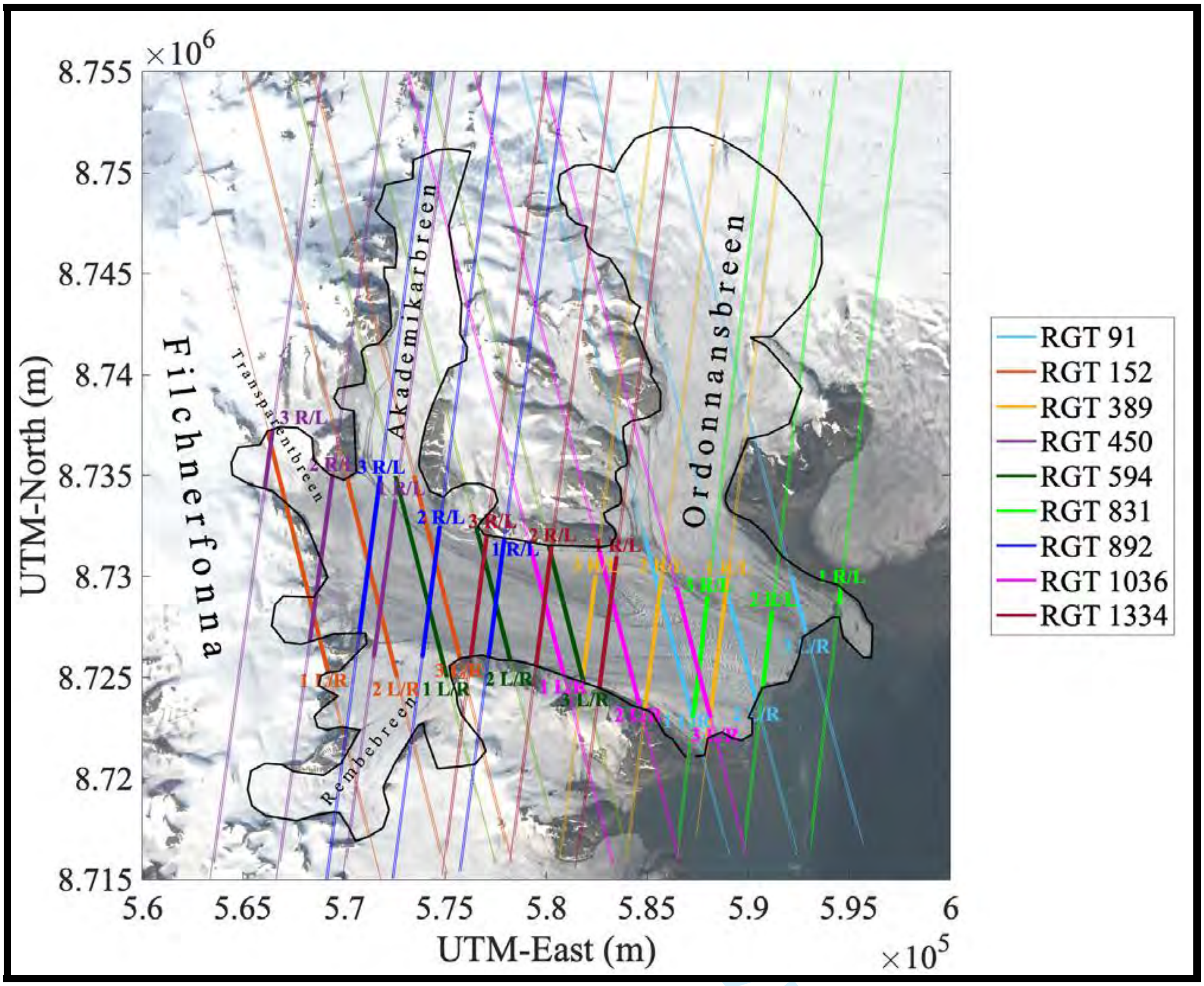

Fig. 2. ICESat-2 survey lines over the Negribreen Glacier System. The survey lines for each of ICESat-2's three beam-pairs are color coded by their Reference Ground Track (RGT) while the NGS borders are given by the black line. The thick lines correspond to the part of the track that is analyzed in this paper which is mostly equivalent to the boundaries of Negribreen Glacier. Left/Right (L/R) beam-pairs are separated by ∼90 m on-ice which is within line thickness over Negribreen in this figure. Background image from Landsat-8 acquired 2019-08-05.

Specifically, the 2019 flight campaign under-flew two beam pairs: RGT 594 (gt1l and gt1r) from 5 August 2019, and RGT 450 (gt1l and gt1r) from 18 August 2019 (Herzfeld and others, 2022). These two tracks passed over interesting crevassed areas in upper Negribreen (Fig. 2) and their dates of collection coincided with the field campaign. Crevasse characteristics along these tracks were quantified in Herzfeld and others (2021) and Herzfeld and others (2022) which found a close agreement between crevasse morphology, spacing and depth between ULS data and ICESat-2 data.

Selected photos from the 2019 campaign, taken with a handheld Nikon D5100 Single-Lens Reflex (SLR) camera, are given in Figures 3 and 4. During the campaign in August 2019, much of the lower glacier was covered in low-lying mixed-phase clouds (MPCs) (Shupe and others, 2006; de Boer and others, 2009; Shupe and others, 2011; Gierens and others, 2020) (Fig. 3(a)). MPCs in Svalbard occur in every season within 1 km of the surface, and have a complicated structure consisting of supercooled liquid and ice layers that obviously obscure the glacier ice-surface (Gierens and others, 2020). These ephemeral low-lying clouds restricted airborne surveys to the upper NGS for several, but not all, flights in 2018 and 2019.

For Peer Review

Fig. 3. Imagery from the airborne campaign flights over Negribreen in August 2019 (Part 1). (a) Low-lying clouds covering the lower glacier and terminus (photo looking downglacier, DSC_0753). (b) Young surge crevasses in upper Negribreen (acquired 13 August 2019, DSC_0898). (c) Large and complex crevasses exceeding 30 m depth in the center-front of the glacier just above the terminus (DSC_0422).

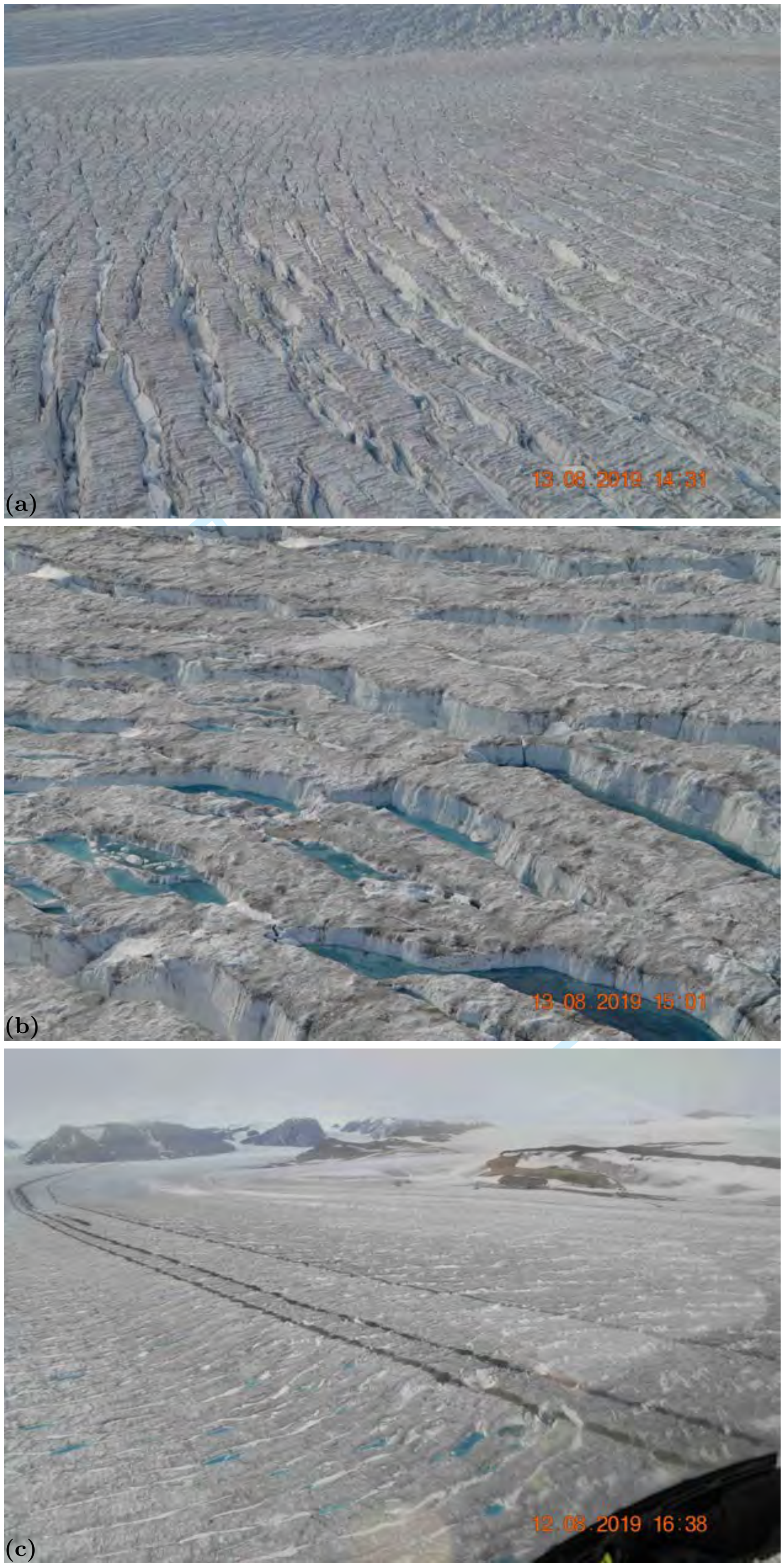

Fig. 4. Imagery from the airborne campaign flights over Negribreen in August 2019 (Part 2). (a) Snow-bridged crevasses seen most clearly in the left-foreground with the white, fresh snow covers the top of the open crevasses, DSC_0656. (b) Water-filled crevasses, DSC_0819. (c) Crevasses near the Negribreen-Akademikarbreen Medial Moraine (NAMM) are filled with water indicating a disruption in the local englacial drainage system, DSC_0344. Fresh crevassing through surge expansion affected this area along the northern NAMM in early 2020, shortly after this photo was taken.

Cambridge University Press

2.3. Sentinel-1 SAR Data

We used Synthetic Aperture Radar (SAR) imagery from the European Space Agency's (ESA's) Sentinel-1 satellite (Geudtner and others, 2014) to derive velocity estimates on Negribreen. Mean velocity estimates are derived for several characteristic time periods between 2019 and 2020 which are used to supplement the ICESat-2 analysis by providing basic information on changes in the velocity field associated with the surge.

There are two Sentinel-1 satellites labeled A and B, which in tandem provide repeat imagery every 6-days for a given location. ESA freely provides the Sentinel Application Platform (SNAP) software to derive surface velocity estimates for ice sheets and glaciers using offset tracking methods. Offset tracking methods measure feature motion between two images using patch intensity cross-correlation optimization.

Over Negribreen, Sentinel-1 operates in the Interferometric Wide (IW) swath mode acquiring data with a 250 km swath at 5 m by 20 m spatial resolution. The SNAP toolbox offset tracking method takes as input the Level-1 Ground Range Detected (GRD) product from two Sentinel-1 images. These images are separated by a temporal baseline, which in our analysis is usually equal to 12-days, i.e. the length the repeat cycle of a single Sentinel-1 satellite. The GRD products are updated with more accurate orbit data and are then coregistered based on geometry given by the ACE-30 Digital Elevation Model (DEM). We then perform offset tracking providing a 300 m by 300 m resolution velocity product with missing or low-confidence data interpolated up to 1 km.

Four characteristic velocity maps from 2019 to 2020 are provided in Figure 5. It is clear in each map that Negribreen is surging, reflected by elevated speeds (> 1 m/day), while the tributary glaciers remain at typical quiescent speeds well below 1 m/day. Velocity magnitudes are largest near the front of Negribreen and decrease across its length with elevated speeds still present near the border with Filchnerfonna in the upper glacier.

Figure 5(a) displays mean velocity magnitudes near the beginning of our study period between 2019-01-05 and 2019-03-30, with maximal velocities reaching 4 m/day. The relatively long 3-month baseline used here, compared to the 12-day baselines in the other maps, demonstrates the possible issue when using feature tracking methods at locations where large and rapid deformation is occurring. The largest deformation events on Negribreen during this time are occurring near the front of the glacier system which may explain why this velocity pattern differs from the others in this series around the front 5 km of the glacier.

For Peer Review

Figure 5(b) provides mean velocity estimates between 2019-08-11 to 2019-08-23, corresponding to the time of the August 2019 field campaign of (Herzfeld and others, 2022). Maximal surge speeds were near 6 m/day. Typically, by August, maximal surge speeds begin to slow significantly from their July maximum.

Figure 5(c) provides mean velocities between 2020-07-10 and 2020-07-22 when the glacier system is moving its fastest for the year due to an abundance of meltwater that lubricates the glacier base. Maximal velocities in July 2020 reached 10 m/day, similar to those in July 2019.

Finally, Figure 5(d) gives mean velocities between 2020-12-19 and 2020-12-31 near the end of our analysis period. This map provides typical velocities during winter time in Negribreen in 2019 and 2020 with maximal velocities around 4 m/day.

For Peer Review

3. METHODS

3.1. DDA-ice: High Resolution Surface Heights from ICESat-2 Data

We applied the DDA-ice algorithm to the raw photon data found in ATL03 to identify the ice-surface signal at sensor resolution, which is then interpolated at 5 m (or less) resolution to attain a final ice-surface height estimate that is used for further analysis. The full mathematical description of the DDA-ice is found in Herzfeld and others (2017) and Herzfeld and others (2021).

The central idea of the DDA-ice is to calculate the "density" of returned photons as an additional dimension for identifying signals in the photon cloud. Density is calculated for each photon using a radial basis function that weights neighboring photons using an 2D anisotropic Gaussian kernel biased in the horizontal direction. An auto-adaptive thresholding scheme identifies signal photons by finding the densest photons, which vary in magnitude along-track due to different reflectance properties, background noise and time-of-day. Finally, the DDA-ice uses a ground follower to provide a surface estimate by interpolating the signal photons, weighted by density, at a specified resolution. The surface resolution is increased when the algorithm suspects high surface roughness, such as crevasses, so that these features are correctly traced.

The DDA-ice uses algorithm-specific parameters to best identify the type of surface under investigation. Three important parameters that control the shape of the weighting kernel include the standard deviation of the Gaussian distribution (sigma, s), the amount of standard deviations used for weighting (cutoff, u) and the anisotropy factor (a) that specifies the ellipticity of the kernel with positive values giving a more horizontally-stretched shape. There are two main parameters that control the thresholding which include the quantile (q) and the offset factor (k). The interpolated surface estimate given by the ground follower

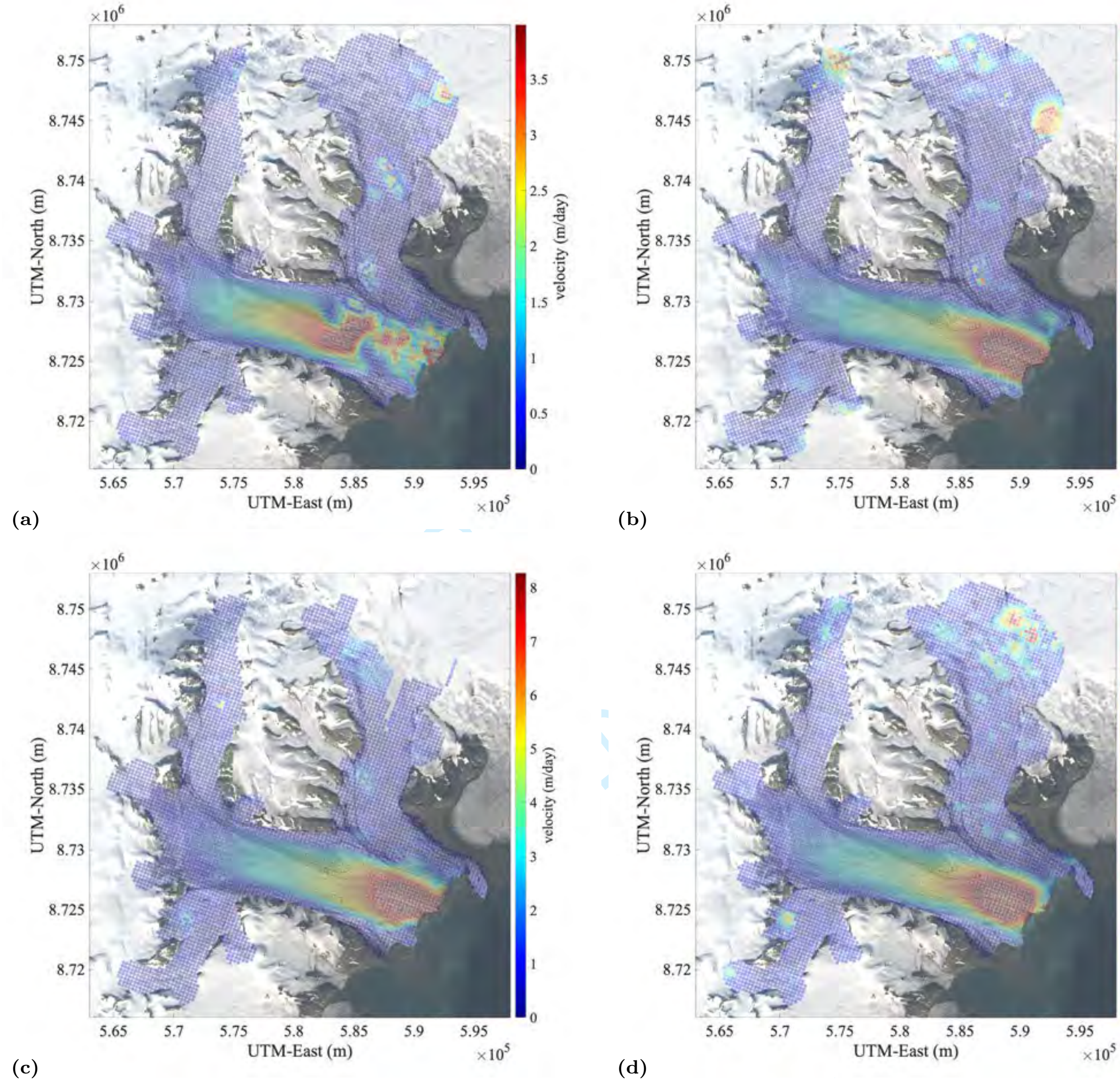

Fig. 5. Negribreen velocity maps from 2019-2020. Maps are derived from Sentinel-1 SAR data. (a) Mean surface velocities between 2019-01-05 to 2019-03-30 (m/day). Over a longer ∼3 month baseline, velocity information can become lost or skewed in areas of high deformation as seen near the terminus. (b) Mean surface velocities between 2019-08-11 to 2019-08-23 (m/day). This baseline spans the 2019 airborne campaigns in August 2019. (c) Mean surface velocities between 2020-07-10 to 2020-07-22 (m/day) with peak surge speeds exceeding 8 m/day. July typically sees the fastest ice-surface speeds in Negribreen. (d) Mean surface velocities between 2020-12-19 to 2020-012-31 (m/day) at the end of the study period in December 2020 which shows typical velocities during the winter months of 2019 and 2020.

has a resolution, R, and provides increased resolution around rough surfaces by a factor of r. The increased resolution is triggered by the roughness parameter, S, that specifies a standard deviation limit for the vertical distribution of thresholded signal photons. Finally, the estimated depth of crevasses is controlled by the crevasse-quantile parameter, Q. The specific parameter values we use in this analysis of Negribreen are given in Table 1.

3.2. ICESat-2/DDA-ice Data Processing

We ran the DDA-ice on all ICESat-2 ATL03 data over Negribreen from January 2019 through 2020 using the parameters from Table 1, which are close to the "default" parameters given in Herzfeld and others (2021). The same parameter values were used for both the strong and the weak beams. We began by processing all the strong beam data for a given cycle, which consists of three beams per pass with 9 passes (individual RGTs) per cycle. After each run we manually filtered out all the cloudy data by looking at the DDA-ice results so as to be sure that we retain only ice-surface signals.

For each beam pass we calculated the along-track "ice-signal fraction" as an indicator of the cloudiness of each measurement pass over the NGS (Column 2 in Table 2). The ice-surface fraction takes the length along-track for which a valid ice-surface height was estimated and divides it by the total along-track survey length. The total along-track survey length (in meters) for each beam pass over the NGS is given in Column 3 of Table 2).

For Peer Review

symbol	meaning	value
s	standard deviation	3
u	cutoff	1
a	anisotropy	5
q	threshold quantile	0.75
k	threshold bias offset	0
l	slab thickness (m)	30
R	resolution of ground follower (m)	5
r	factor to reduce the R parameter	5
Q	crevasse depth quantile	0.5
S	standard deviation threshold of thresholded signal to trigger small step size in ground follower (m)	1.75

Table 1. DDA-ice parameters for Negribreen runs in this analysis. The same parameters were used for both the strong and weak beams. Ground-follower resolution when ice surface is rough: With $R = 5$ and $r = 5$, then the crevasse-follower resolution is 1 m.

For Peer Review

RGT and beam	Ice-signal fraction ratio for each pass	NGS coverage length (m)
RGT 91 gt1l	0, 1, N/A, 0, 0.9759, 0, 0.4475, 0.9415	14835
RGT 91 gt1r	0, 1, N/A, 0, 0.8015, 0, 0, 0.9330	14910
RGT 91 gt2l	0, 1, N/A, 0, 0.9275, 0, 0.3188, 0.6482	27255
RGT 91 gt2r	0, 1, N/A, 0.0127, 0.7699, 0, 0, 0.9604	27240
RGT 91 gt3l	0, 1, N/A, 0, 0.8893, 0, 0.1431, 0.9997	19795
RGT 91 gt3r	0, 1, N/A, 0.0026, 0.6979, 0, 0, 1	19625
RGT 152 gt1l	0, 1, N/A, 0.9983, 1, 1, 0, 0.8267	12405
RGT 152 gt1r	0, 1, N/A, 0.9832, 0.8015, 0, 0, 0	12945
RGT 152 gt2l	0, 1, N/A, 1, 1, 1, 0, 0	13205
RGT 152 gt2r	0, 1, N/A, 1, 0.7699, 0, 0, 0	13140
RGT 152 gt3l	0.4680, 1, N/A, 1, 1, 1, 0, 0.7419	17070
RGT 152 gt3r	0, 1, N/A, 1, 0.6979, 0, 0, 0	16865
RGT 389 gt1l	1, 1, 0, 0, 0, 0.9147, 0, 0.4372	24510
RGT 389 gt1r	1, 1, 0, 0, 0, 0.8347, 0, 0.7558	25855
RGT 389 gt2l	1, 1, 0, 0, 0, 0.9030, 0.3192	28570
RGT 389 gt2r	1, 1, 0, 0, 0, 0.9113, 0, 0.8746	28580
RGT 389 gt3l	1, 1, 0, 0, 0, 0.9489, 0.9366	15200
RGT 389 gt3r	1, 1, 0, 0, 0, 0.8728, 0, 0.9913	14885
RGT 450 gt1l	0.3259, 0, 1, 0, 1, 1, 0.5635, 1	34085
RGT 450 gt1r	0.7462, 0, 1, 0.9976, 1, 1, 0.5886, 1	33945
RGT 450 gt2l	0.2556, 0, 1, 0, 1, 1, 0.9637, 1	10085
RGT 450 gt2r	0.4030, 0, 1, 1, 1, 1, 0.8338, 1	9955
RGT 450 gt3l	0, 0, 1, 0, 1, 1, 1, 1	2995
RGT 450 gt3r	0, 0, 0.9933, 1, 1, 1, 1, 1	2930

Table 2. Coverage statistics of each RGT and beam over the NGS for 2019-2020 (part 1). This table is a summary of the dat sheet negri_data_2019_2020.xlsx.

For Peer Review

RGT and beam	Ice-signal fraction ratio for each pass	NGS coverage length (m)
RGT 594 gt1l	1, 0.6278, 1, 0.8892, 0.9373, 1, 0	21205
RGT 594 gt1r	1, 0, 0.9998, 0.9624, 1, 1, 1, 0	21275
RGT 594 gt2l	1, 0.6083, 1, 0.9372, 0.9366, 1, 0	19410
RGT 594 gt2r	1, 0, 1, 0.6994, 1, 1,1, 0	19345
RGT 594 gt3l	1, 0.852, 1, 0.9488, 0.9588, 1, 0	9245
RGT 594 gt3r	1, 0, 1, 0.7857, 1, 1, 1 ,0	9130
RGT 831 gt1l	0,1, 0, 1, 1, 0, 0, 0.9821	1510
RGT 831 gt1r	0, 0, 0, 1, 1, 0, 0, 0	1505
RGT 831 gt2l	0, 1, 0, 1, 1, 0, 0, 1	11210
RGT 831 gt2r	0, 0, 0, 1, 1, 0 , 0, 1	11196
RGT 831 gt3l	0.0899, 1, 0.5379, 1, 1, 0, 0, 1	29625
RGT 831 gt3r	0, 0, 0.3165, 1, 1, 0, 0, 1	29625
RGT 892 gt1l	1, 0, 1, 0, 1, 0, 0.9918, 1	7295
RGT 892 gt1r	1, 0, 1, 0, 1, 0, 0.9178, 1	7410
RGT 892 gt2l	1, 0.1214, 0.6287, 0, 1, 0, 0.7826, 1	12800
RGT 892 gt2r	1, 0, 0.3504, 0, 1, 0, 0.6948, 1	13135
RGT 892 gt3l	1, 0.4993, 0.4898, 0, 1, 0, 0.8043, 1	29030
RGT 892 gt3r	1, 0, 0.4618, 0, 1, 0, 0.7361, 1	29920
RGT 1036 gt1l	0.8343, 0.1976, 0, 0, 1, 0, 0.7521, 0	11565
RGT 1036 gt1r	0, 0, 0, 0, 1, 0, 0.8224, 0	10810
RGT 1036 gt2l	0, 0, 0, 0, 1, 0, 0.9581, 0	8235
RGT 1036 gt2r	0, 0, 0, 0, 1, 0, 0.8395, 0	8265
RGT 1036 gt3l	0, 0.0678, 0, 0, 1, 0.7024, 0	18880
RGT 1036 gt3r	0, 0.2084, 0, 0, 1, 0, 0.6544, 0	19640
RGT 1334 gt1l	1, 0.2680, 0.9997, 0, 0, 1, 0, 0.3898	24382
RGT 1334 gt1r	1, 0, 1, 0, 0, 1, 0, 0.6998	24200
RGT 1334 gt2l	1, 0.6567, 1, 0, 0, 1, 0, 0.6323,	10020
RGT 1334 gt2r	1, 0, 1, 0, 0, 1, 0, 0.8037	9995
RGT 1334 gt3l	1, 0.7915, 0.9862, 0, 0, 1, 0, 0.9958	9435
RGT 1334 gt3r	1, 0, 0.9799, 0, 0, 1, 0, 1	9830

Table 3. Coverage statistics of each RGT and beam over the NGS for 2019-2020 (part 2). This table is a summary of the dat sheet negri_data_2019_2020.xlsx.

For Peer Review

Next, we processed all the weak-beam data for which the associated strong-beam pair yielded a non-zero ice-signal fraction. Typically, the weak-beam provided a non-zero ice-surface fraction when the associated strong-beam gave an ice-signal fraction greater than 0.9.

3.3. Surface Height Change Determination

We analyze ice-surface height change across each of the 54 ICESat-2 ground tracks across Negribreen in 2019 and 2020 in order to estimate mass transfer occurring during the surge evolution. At the resolution of the DDA-ice interpolated ground estimate (1-5m) however, high-resolution morphology, particularly crevasses, complicate the bulk height change estimate. For example, young surge crevasses forming and evolving in upper Negribreen (Figure 4(b)), which can reach depths of 30 m, act to underestimate the mean surface height of the glacier surface, especially when ground follower resolution is refined over the crevasses. That is, the cross-sectional area of the crevasse voids at the surface is small compared to the total cross-sectional area across the width of the glacier. Height change analysis is further complicated if the geophysical signal we are tracking corresponds to crevasse deepening of crevasses advection. Therefore, for height-change estimates in the case of young surge crevasses in upper Negribreen, we estimate surface height of the glacier surface by using the 90th percentile height for every 30 m along-track bin.

Crevasses in lower Negribreen are more complex and have undergone several deformational processes at this point in the surge. While originally they may have resembled the young crevasses in upper Negribreen, large-scale dynamics near the front of the glacier have transformed these mature crevasses to appear markedly different from those in Upper Negribreen as seen in Figure 3(c). Here, the cross-sectional area of crevasse voids is significantly large compared to the total cross-sectional area. We therefore calculate surface heights for height-change analysis in this region by taking the 50th percentile surface height for every 30 m along-track bin. This gives the average surface height within the 30 m bin and smooths out processes that change individual crevasse characteristics that may complicated surface height change determination.

3.4. Roughness and Crevasse Characteristics

From ICESat-2/DDA-ice surface heights, vario functions are calculated to derive surface roughness values, which are characteristic of the spatial structure of the ice surface (Herzfeld, 2008; Herzfeld and others, 2021). Every 200 m along-track, we calculate discrete first-order vario function vectors, $\boldsymbol{v^k} = [v_1, ..., v_j, ..., v_N]$, within 400 m windows centered at location x_k, which act on n pairs of height estimates, $z(x_i)$ and $z(x_i + h)$ separated by some lag distance h grouped in bins defined by the vector $\boldsymbol{h}$, whose bounds are indexed by j:

For Peer Review

$$v_j^k = \frac{1}{2n}\sum_{i=1}^{n}\left(z(x_i) - z(x_i + h)\right)^2 \tag{1}$$

where x_i is the along-track location of a height estimate (z) and h is the separation, or lag, distance between pairs of points with $h_{j-1} < h \leq h_j$, for $j = 1, ..., N$, with $h_0 = 0$. We use $N = 10$ discrete lag distance bins of length 40 meters to characterize the surface at a given point x_k, implying $\boldsymbol{h} = [0, 40, 80, ..., 400]$.

In cases where there are underlying regional trends in the data, such as a glacier's surface slope, it is more useful to use the residual variogram to quantify roughness (Herzfeld, 2008). Using the mean value m at a center point x_k, given by

$$m_j^k = \frac{1}{n}\sum_{i=1}^{n}\left(z(x_i) - z(x_i + h)\right) \tag{2}$$

the residual variogram V for a reference center point x_k is defined as

$$V_j^k = v_j^k - \frac{1}{2}m_j^k \tag{3}$$

where lag distance bins $h_{j-1} < h \leq h_j$, for $j = 1, ..., N$ are used in both equations 2 and 3.

We derive an estimate of surface roughness at point x_k, ζ_k, by taking the maximum of $\boldsymbol{V^k}$ (i.e. the infinity norm):

$$\zeta(x_k) = |\boldsymbol{V^k}|_\infty = max(\boldsymbol{V^k}) \tag{4}$$

The parameter ζ is equivalent to the 1D *res_pond* parameter in Herzfeld (2008), though in the current analysis we refer to this quantity simply as roughness (of the glacier surface). This parameter is also derived using 2D (residual) vario functions applied to satellite imagery of a surging Bering Glacier, Alaska, in Trantow and Herzfeld (2018).

Additional crevasse and crevasse field characteristics, i.e. crevasse spacing and depth, are calculated from the DDA-ice height outputs for selected ICESat-2 tracks. Crevasse spacing and depth are determined using a simple deterministic algorithm Herzfeld and others (2013b, 2021, 2022), which identifies individual crevasses when the so called *jump_height* between crevasse top and crevasse bottom exceeds 2 meters.

For Peer Review

3.5. Roughness Change Determination

We calculate mean rates of roughness change in 2019-2020 using the roughness measure, ζ (or res_pond), derived in Equation 4. While we are interested in the year-to-year dynamical component of roughness change, it is important to consider its significant seasonal component. During the winter months of snow accumulation, approximately October through April, crevasses of moderate and narrow widths can become covered, or bridged, by snow. These snow-covered crevasses can persist throughout the summer in locations of low deformation as seen in Figure 4(a). In this case, only the widest crevasses will be detected by the DDA-ice, which finds the primary signal. The DDA-bifurcate-seaice algorithm (Herzfeld and others, 2023) is able to detect secondary signals such as those beneath the water surface, but is not employed in this analysis as it is not yet reliably adapted to land-ice applications. Because many crevasses are bridged by snow in winter, analysis of roughness change is derived using data from summer months only when snow-bridges are the least prevalent (roughly May through October). During peak melt season in July and August however, crevasses exist that are filled with water at locations where the surge deformation has destroyed normal englacial drainage paths that route water from the glacier surface to the base (see image in Figure 4(b)) (Kamb and others, 1985; Harrison and Post, 2003). Water-filled crevasses are present throughout the glacier system but affect only a small number of the total crevasses (Herzfeld and others, 2022), and therefore should not significantly affect the overall roughness estimates in this analysis.

For Peer Review

4. RESULTS

4.1. Surface Height and Surface Height Change

4.1.1. Surface Heights and Data Coverage for each ICESat-2 Cycle

Along-track ice-surface height estimates yielded by the DDA-ice ground follower at 1-5 m resolution, as determined by the algorithmic parameters in Table 1, are given for the four cycles in 2019 (Figure 6) and the four cycles in 2020 (Figure 7). Heights in the NGS range from ∼0 m (sea-surface height) at the terminus to over 800 m in the upper tributary glaciers.

The most sparse coverage of the glacier system occurs during the late-summer/autumn months, particularly in the lower part of the glacier system, when low-level mixed-phase clouds (MPCs) have their highest occurrence (Shupe and others, 2006; de Boer and others, 2009; Shupe and others, 2011; Gierens and others, 2020) (see Figure 3(a)). During all but a couple cycles, Akademikarbreen is more densely covered than Ordonnansbreen likely due to the local orography which strongly influences the occurrence and characteristics of MPCs (Gierens and others, 2020).

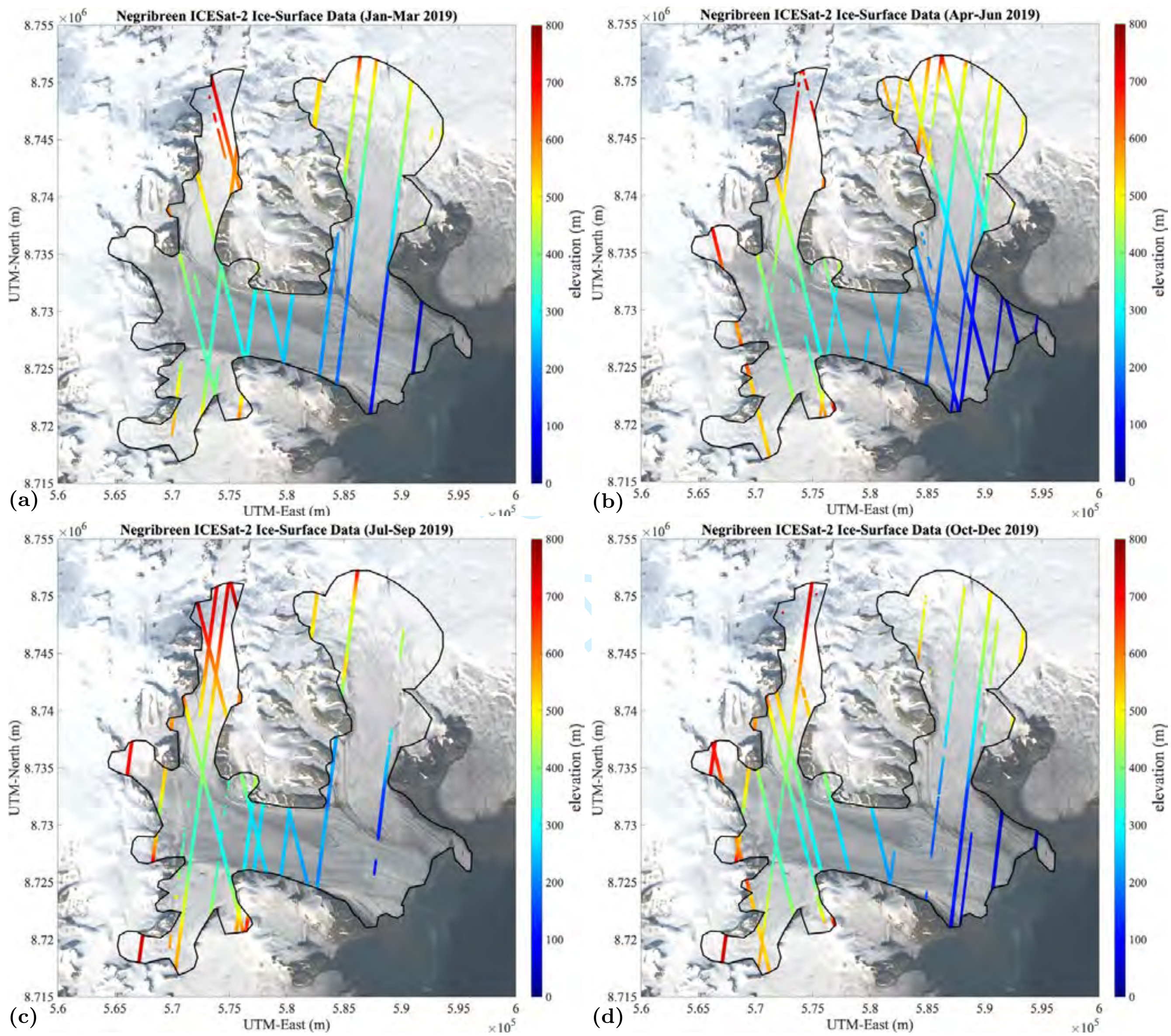

Fig. 6. 2019 Negribreen ice-surface height data from the DDA-ice for single ICESat-2 cycles (91 days). (a) January-March 2019, (b) April-June 2019, (c) July-September 2019, (d) October-December 2019.

4.1.2. Surface Height Rate of Change (2019-2020)

Figure 8 gives the average surface height rate of change from 2019 to 2020 following the processes outlined in Section 3.3. While this calculation provides mean height changes in meters per year, it is important to note that the majority of the change occurs in the summer months, with very little height change between January and April. This is seen more clearly in the times series plots of Section 4.3.

Cambridge University Press

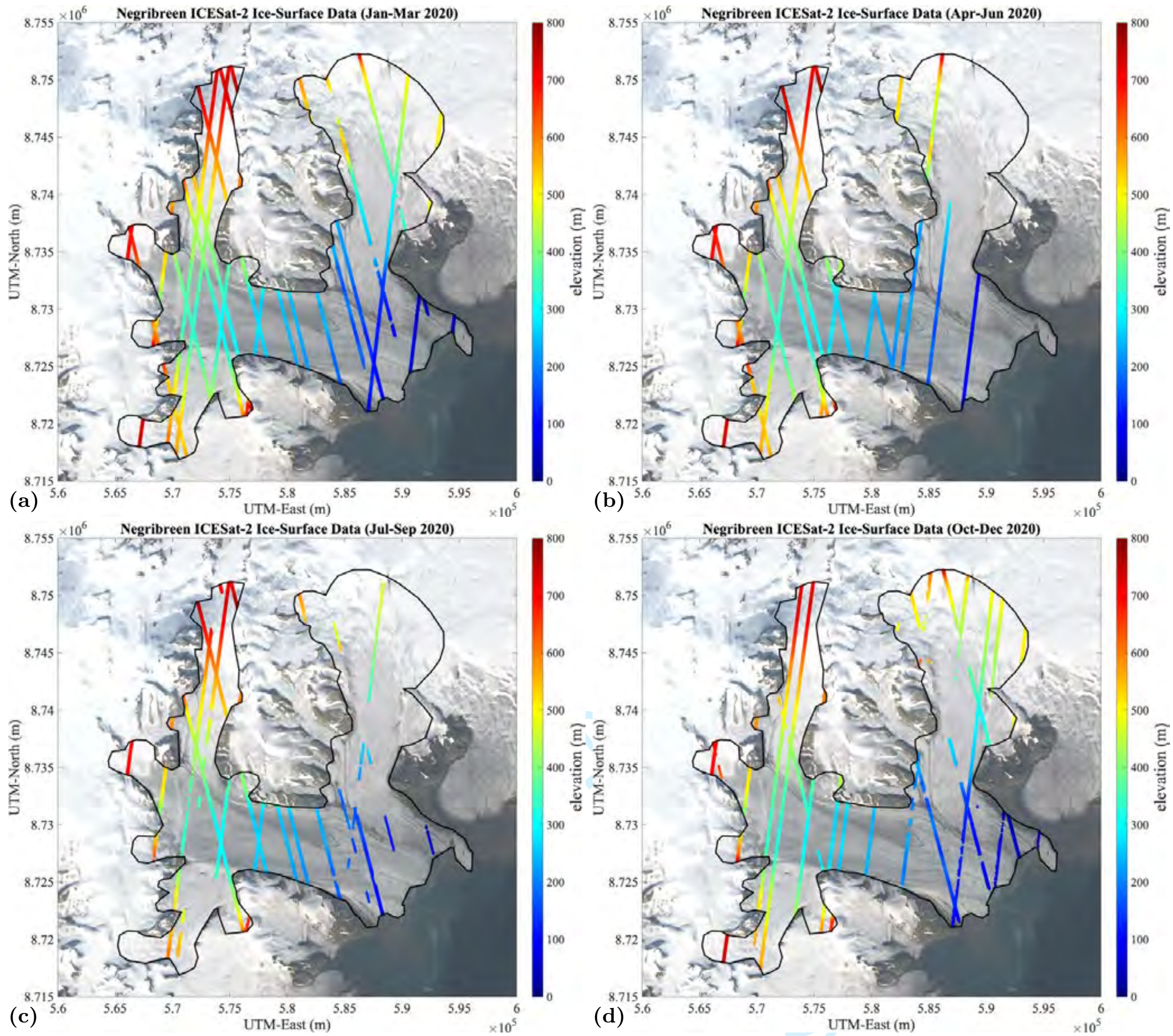

Fig. 7. 2020 Negribreen ice-surface height data from the DDA-ice for single ICESat-2 cycles (91 days). (a) January-March 2020, (b) April-June 2020, (c) July-September 2020, (d) October-December 2020.

Figure 8 shows general thinning in the upper glacier above 5.85×10^5m UTM-East and general thickening in the lower glacier below, implying a mass transfer from the upper glacier to the lower glacier. Surface heights grew between 2019 to 2020 in the front ∼1/3 of the glacier at a rate reaching 30 m/year near Negribreen's terminus. A chaotic pattern of tightly spaced surface lowering and surface gains exceeding ± 30 m/yr near the center-front of the glacier reflects the generation and advection of massive and complex crevasses (see image in Figure 3(c)).

Surface lowering occurs in the upper ∼2/3 of Negribreen, while surface heights remain mostly constant on tributary glaciers such as Akademikarbreen and Rembebreen, which is seen clearly at the crossing of the medial moraines in Figure 8. Aside from a slight lowering near its terminus, Ordonnansbreen also saw little changes in surface height from 2019 to 2020 despite the significant height changes occurring just across the medial moraine on the surging Negribreen.

There is, however, a clear surface lowering of around 8 m/yr on Transparentbreen, which connects Negribreen to the Filchnerfonna accumulation zone above the NGS. Thus, the surge of Negribreen is affecting additional parts of the glacier system, expanding beyond the main glacier, across Transparentbreen and into the large catchment area above the glacier (Filchnerfonna). Transparentbreen appears to be the only tributary glacier in the NGS experiencing significant height-change during the surge expansion from 2019 to 2020.

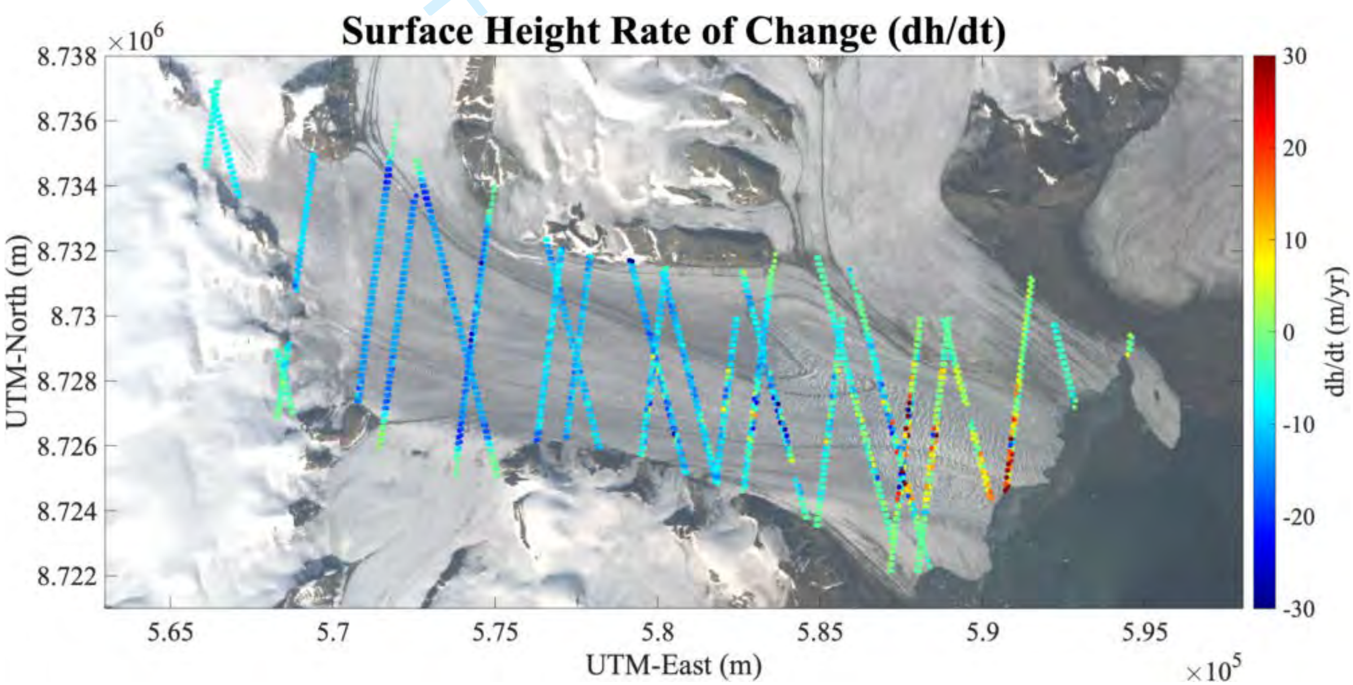

Fig. 8. Rates of change of glacier surface height during the 2019-2020 part of the recent Negribreen surge. Surface height change rate in meters per year.

4.2. Surface Roughness and Roughness Change

Crevassed regions are indicated by high surface roughness (Herzfeld, 2008; Herzfeld and others, 2014; Trantow and Herzfeld, 2018; Herzfeld and others, 2021, 2022). Negribreen's ice-surface roughness, given by ζ in Equation 4 (res_pond), for the four ICESat-2 cycles of 2019 and 2020 is shown in Figures 9 and 10 respectively. The medial moraines provide a clear boundary between the rough and surging Negribreen and the relatively smooth surfaces of the non-surging tributary glaciers. In general, roughness is larger further downglacier as the surging ice experiences more deformation events moving through the glacier system with the strongest events experienced near the glacier front where surge velocities are largest (Figure 5).

Figure 11 gives the mean rate of change of dynamically-induced roughness over the 2019-2020 period of the NGS surge following the approach discussed in Section 3.5. Negribreen began surging in 2016 near the glacier front and has expanded upglacier as the surge matures (Haga and others, 2020; Herzfeld and others, 2022). We see that for the most part, surface roughness has decreased in the lower glacier reflecting reduced surge activity at that location. There are locations in the lower glacier however, that have seen increased roughness indicating the continued occurrence of strong, but isolated, surge deformation events.

In contrast, large portions of the upper glacier experienced increased roughness over the study time interval (e.g., yellow regions in Figure 11), which reflects the expansion of the surge up-glacier in Negribreen. Large increases in surface roughness also occurred in the ice falls between the Filchnerfonna and Negribreen, which illustrates further expansion of surge effects beyond Negribreen and into the accumulation zone above the glacier.

For Peer Review

4.3. Time Series of ICESat-2 Surface Height Profiles

In this section, we analyze time series of selected ICESat-2 profiles that allow derivation of glaciological changes associated with the surge of the NGS in 2019-2020. We present a subset ICESat-2 profiles, identified by their associated RGT and beam, based on the glaciological insight that their result provided. The full collection of ICESat-2 time series for each of the 54 ICESat-2 profiles can be found in the supplementary material (negri.change.suppl.pdf).

4.3.1. Detection of New Surge Crevasses and Changes in Existing Crevasse Fields

ICESat-2 data analyzed with the DDA-ice facilitate identification of crevasses (Herzfeld and others, 2017, 2021, 2022). Here we utilize this crevasse detection capability to analyze and map the progression of the surge through the NGS in 2019-2020.

All crevasse fields observed and analyzed here evolved morphologically through expansion or contraction, advection down-glacier, formation of a snow-bridge and/or filling with water. An example of crevasse expansion is given by the occurrence of new crevasse fields formed in upper Negribreen along RGT 594 gt1l as seen in Figure 12(b) between 8.727 and 8.728 $\times 10^5$ UTM-North where a smooth, uncreavssed ice-surface is reported in early 2019 (orange and yellow lines), and at the same location new crevasses have opened by November 2019 (green line). This particular finding indicates that additional crevasse fields formed in the southern part of upper Negribreen in late 2019, south of an existing larger crevasse field closer

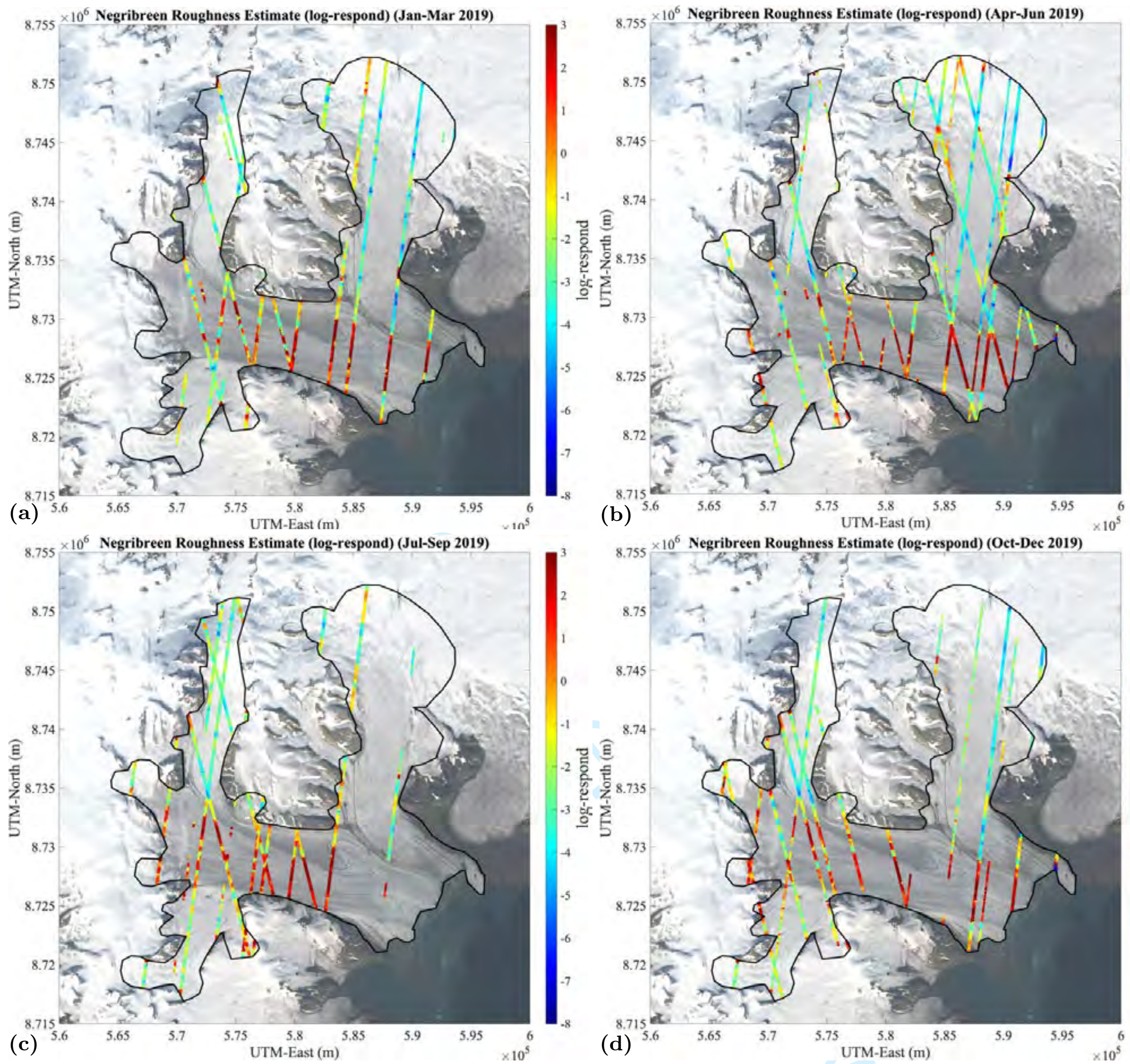

Fig. 9. 2019 Negribreen roughness data per cycle as given by the logarithm of the *logpond* parameter. (a) January-March 2019, (b) April-June 2019, (c) July-September 2019, (d) October-December 2019.

to the boundary with Akademikarbreen. The latter crevasse field was overflown during the airborne field campaigns in 2018 and 2019 (Herzfeld and others, 2021), and RGT 594 gt1l as a whole was utilized in the validation campaign of Herzfeld and others (2022). Another example of the detection of crevasse expansion is found along RGT 594 gt2l in Figure 12(d) near 8.726 $\times 10^5$ m UTM-North where large crevasses formed along Negribreen's southern margin between February and April 2020.

Further evidence of the expansion in upper Negribreen is given by the time series of RGT 450 in Figure 13(a)-(d). Large crevasses reaching 10 m depths near the southern margin formed in early 2020 similar to those detected in the nearby RGT 594 data (Figure 12). Note that beam-pair 1 of RGT 450 is also

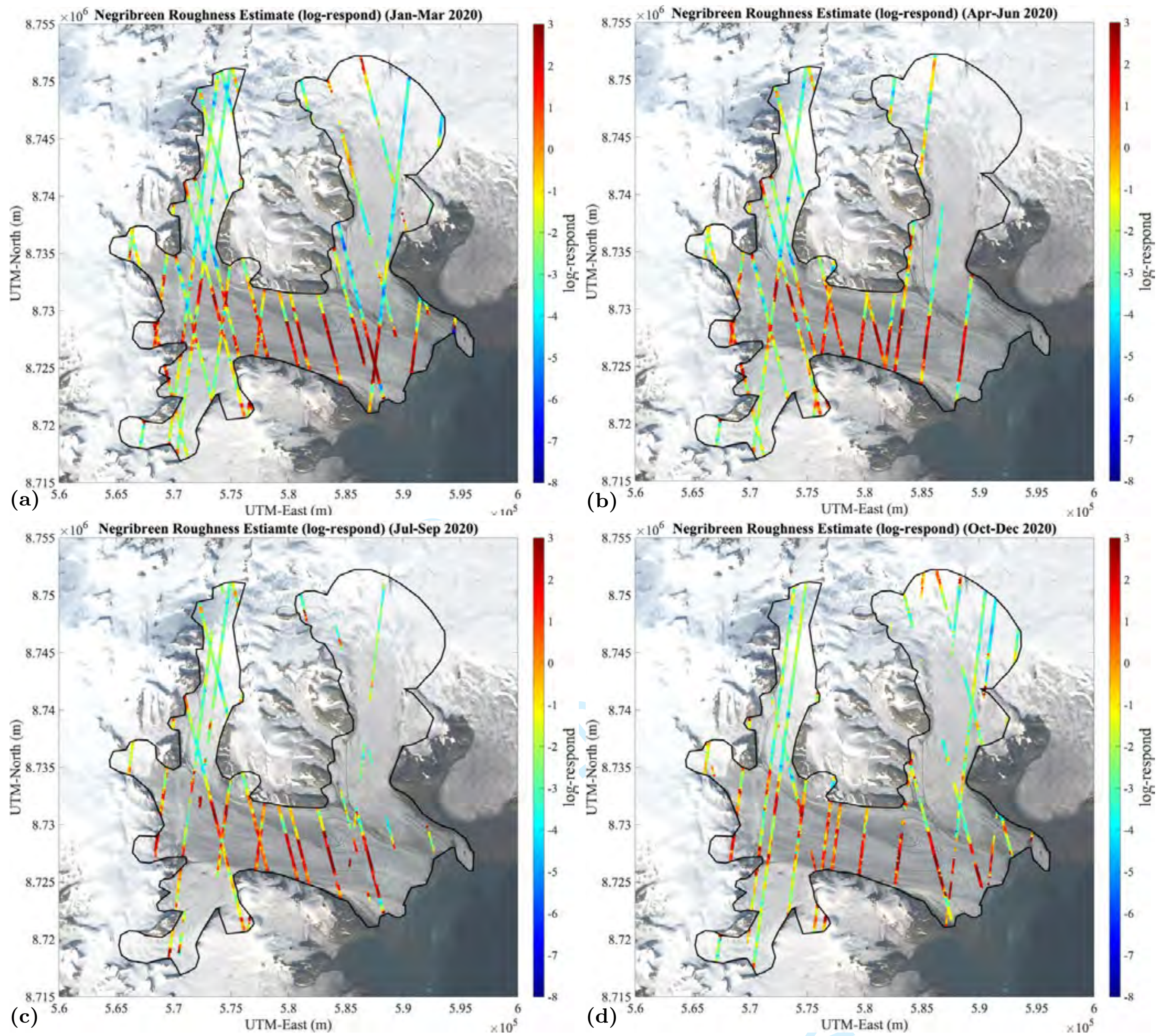

Fig. 10. 2020 Negribreen roughness data per cycle as given by the logarithm of the *logpond* parameter. (a) January-March 2020, (b) April-June 2020, (c) July-September 2020, (d) October-December 2020.

surveyed and analyzed in Herzfeld and others (2022), which shows consistent detection of $\sim$10 m deep crevasses in both the ICESat-2/DDA-ice and the airborne laser altimeter (ULS) data in 2019. In addition, 13(e)-(f), which plots RGT 152 gt3r, shows crevasse expansion across both the northern and southern margin between early 2019 (orange line) and 2020 (green, blue, brown lines). RGT 152 gt3r also presents an example of isolated crevassing and crevasse enlargement in the center of upper Negribreen near 8.729 $\times 10^5$ m UTM-North.

The apparent disappearance of crevasses from 2019 to 2020, such as those in Figure 12(f) near 8.729 $\times 10^5$ m UTM-North, may be from crevasse contraction, advection down-glacier without up-glacier

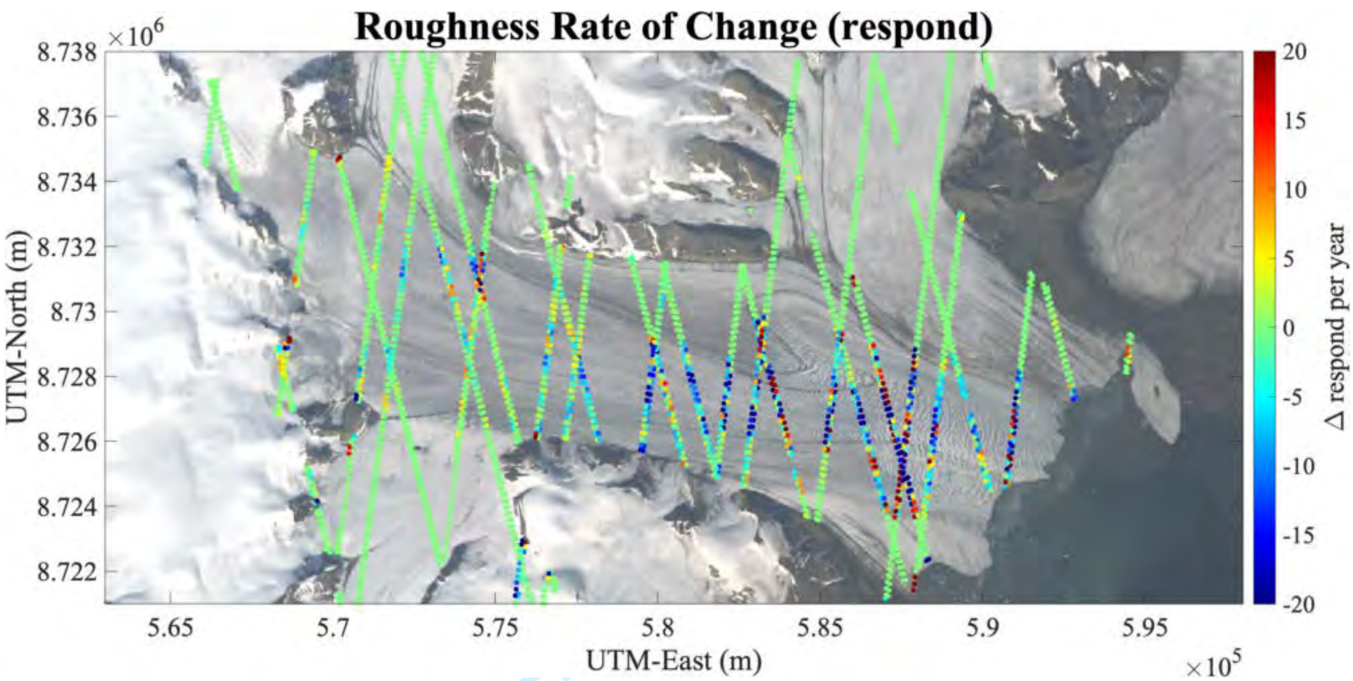

Fig. 11. Rates of change of roughness during the 2019-2020 part of the recent Negribreen surge. Roughness (logpond) change rate in Δpond per year.

For Peer Review

replacement of similar crevasses, snow-bridge formation or becoming filled with water. Imagery may be used to determine the exact process involved. The airborne photograph in Figure 3(a), taken near 8.729 $\times 10^5$ m UTM-North, shows that the crevasses under consideration, i.e. those found in and to the left of the medial moraine in the image, have become bridged by snow.

Returning to RGT 594 gt1l, we proceed to investigate changes in the width and depth of crevasses in the large crevasse field seen in Figure 12(b) between 8.730 and 8.732 $\times 10^5$ UTM-North. Mean surface height change (surface lowering) along this 2 km segment was -11.66 m between August 2019 and August 2020. Mean crevasse spacing increased from 55.45 m to 57.6 m, mean depth decreased from 10.71 m to 9.82 m, and maximum depth decreased from 16.01 m to 15.82 m. These changes in the crevasse characteristics are typical of changes in a crevasse fields that formed during earlier years of the surge in 2017 or 2018, as recorded during our field campaigns. This result is consistent with the plot of Figure 11 that reveals this region to be the only one in upper Negribreen that saw a decrease in surface roughness from 2019 to 2020. Over time, crevasses tend to widen a little, become shallower, and the crevasse edges are more rounded, as erosion progresses (Herzfeld and others, 2013b).

In general, we find that the local maximum of crevasse depth increases from up-glacier to down-glacier regions of Negribreen. From ∼16 m depth along RGT 594 gt1l in upper Negribreen, maximal depths increase to ∼22 m near the mid-glacier along RGT gt3l (Figure 12(f)) and exceed 30 m in the lower glacier near the terminus.

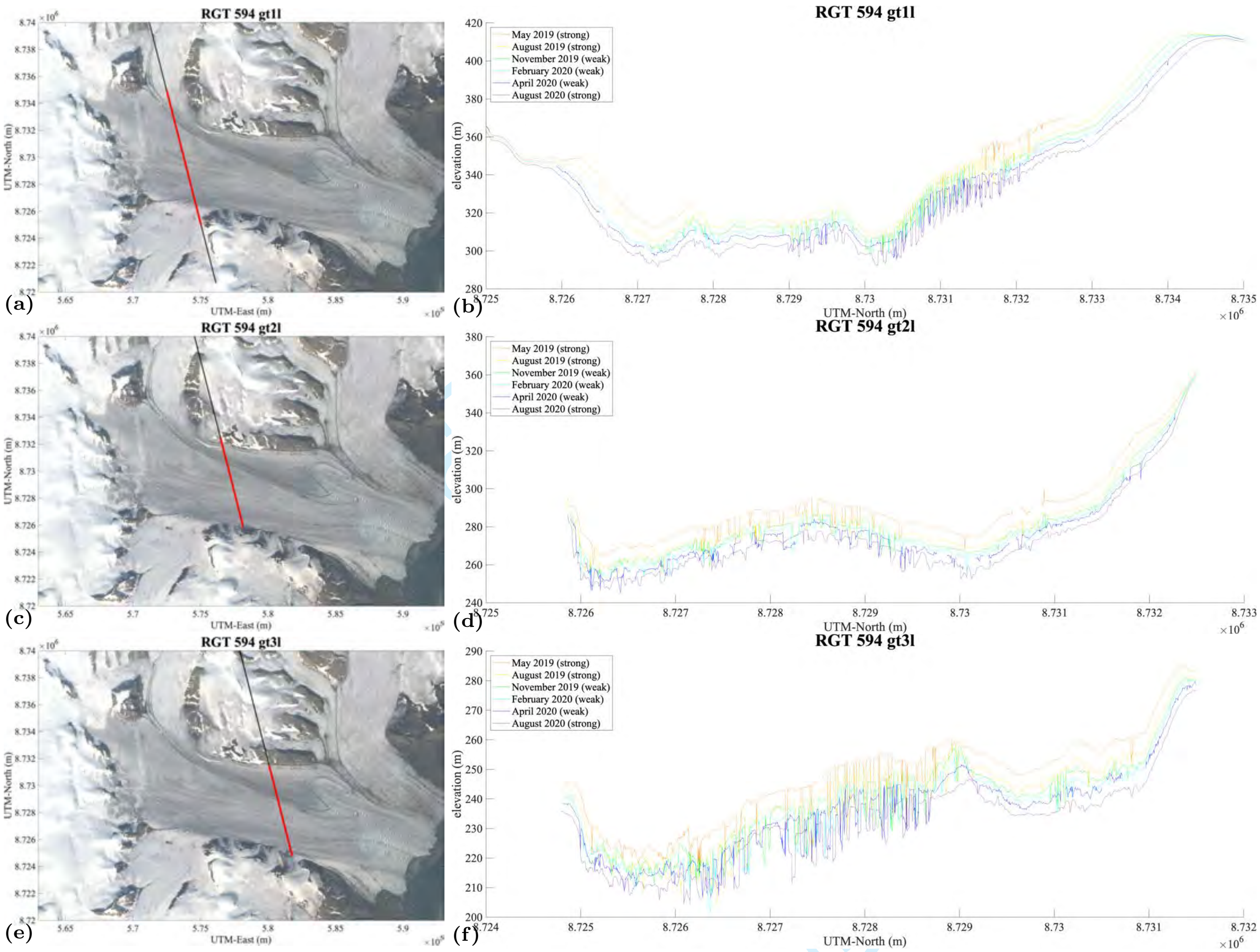

Fig. 12. DDA-ice results for RGT 594 over the Negribreen's major surge-affected area, 2019-2020. (a)-(b) RGT 594 gt1l, (c)-(d) RGT 594 gt2l, and (e)-(f) RGT 594 gt3l.

4.3.2. Surge Expansion Along and Across the Shear Margin

The Negribreen-Akademikarbreen Medial Moraine (NAMM) is easily identified in airborne and satellite imagery as the dark dividing line between the surging ice of Negribreen and the non-surging ice to the north. From its formation point at the Negribreen-Akademikarbreen junction, the NAMM advects down-glacier, past the Lykkenhøgda hills at mid-glacier and along the Negribreen-Ordonnansbreen border in the lower glacier, leaving an obvious stripe through Negribreen near its northern margin. The NAMM provides an example of the folded moraine that can be used to identify a glacier as a surge glacier (Post, 1972; Lefauconnier and Hagen, 1991). The fold results from a shift in the dynamic equilibrium between a surge glacier (here, Negribreen) and a neighboring, non-surging glacier (Ordonnansbreen).

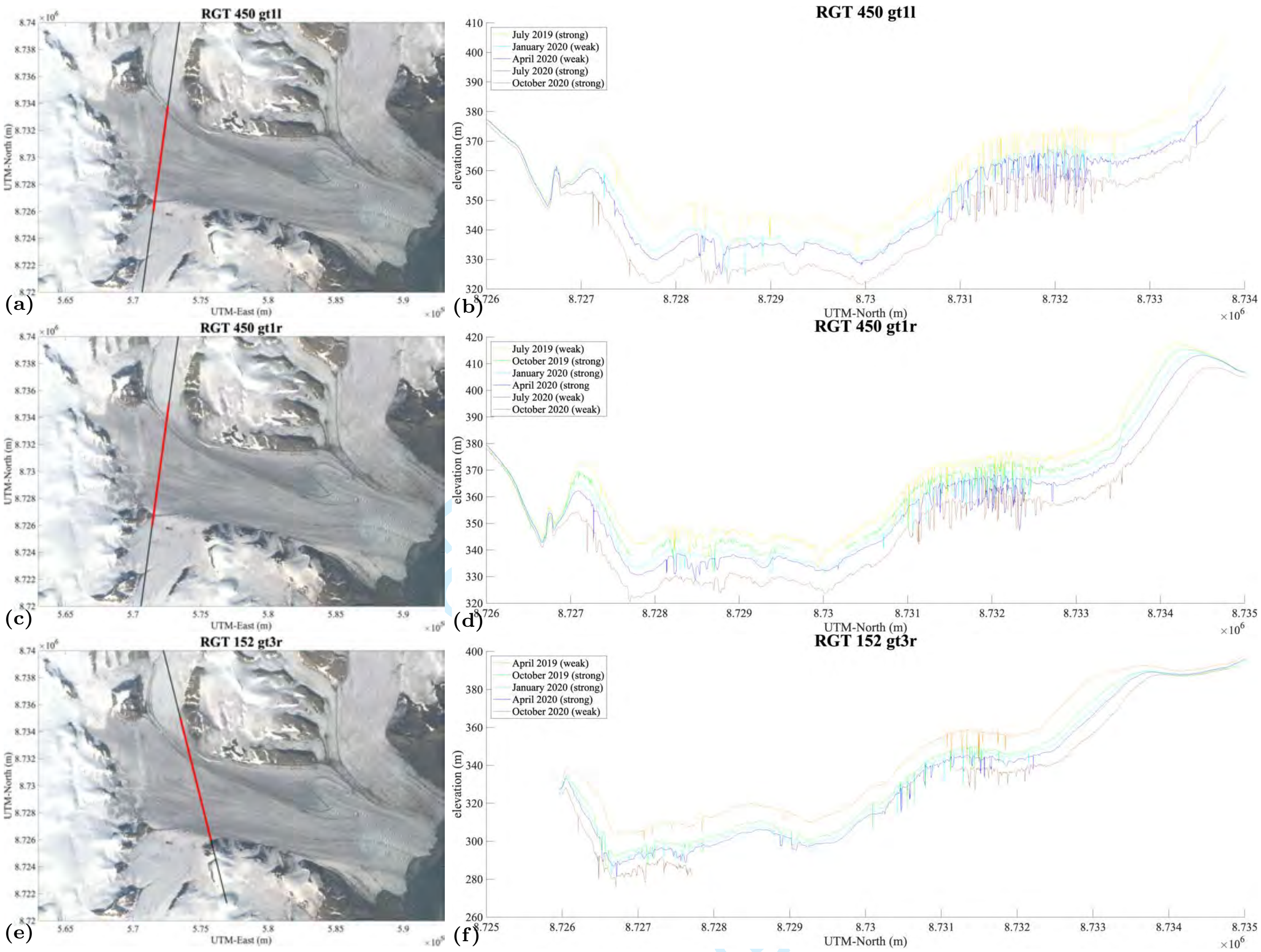

Fig. 13. Further expansion of crevasses in upper Negribreen as given by ICESat-2's RGT 450 and 152, 2019-2020. (a)-(b) RGT 450 gt1l, (c)-(d) RGT 450 gt1r and (e)-(f) RGT 152 gt3r.

Throughout Negribreen's longitudinal extent, large shear stresses exist around the NAMM due to its boundary between the surging ice of Negribreen and the non-surging ice of the northern tributary glaciers. In 2017 and 2018, Herzfeld and others (2022) documented the disintegration of the lower NAMM, i.e., the Negribreen-Ordonnansbreen shear margin, along which the terminus retreated via processes of rifting and calving at a pace faster than observed elsewhere in the glacier (visualized as a "retreating bay" at the terminus). The formation of bays and melange areas occur at former areas of so-called chaotic crevasse types (Herzfeld and others, 2013a), which are often found at locations with large shear stresses.

In the current analysis of surge progression, we detect the development of additional large crevasses in northern Negribreen in the upper-mid glacier around the NAMM (i.e. up-glacier of the largest "retreating bay" observed in 2017) in 2020. Figures 14(a)-(d) display a transverse expansion of crevassing (outward toward the NAMM), recorded in RGT 892 gt1l and gt1r. In August 2019 (yellow lines) deep crevasses

($\sim$10 m) are measured across the majority of the glacier with a northern extent around 8.729×10^6m UTM-North. By August 2020 (purple lines), one year later, these large 10 m deep crevasses are seen to expand transversely (northward) approximately 5 km to the extent of 8.7295×10^6m UTM-North. These new crevasses appear to be wider than the older ones to the south and are an indication of the intensification of the shear margin.

In August 2019, before this noted expansion, large amounts of water were observed in the crevasses near the northern NAMM as seen in Figure 4(c). The presence of clear blue meltwater in crevasses is indicative of a local disruption in the englacial drainage system which can occur in when the surge progresses into a region. Once the drainage pathway reestablishes, the water observed in the crevasses suddenly and rapidly drains to the subglacial system causing a rapid acceleration of the local ice via basal sliding through decreased friction between the glacier base and the underlying bedrock (Cuffey and Paterson, 2010). A local surge in the ice, part of the larger surge complex experienced throughout the glacier system since 2016, results in large crevasses such as those detected here around the NAMM.

In Figure 14(e)-(h), gt2l and gt2r of RGT 1334 show the same transverse (northern) expansion of crevassing across the NAMM at the mid-glacier. The large 10 m deep crevasses expand toward the NAMM beginning at 8.7288×10^6m UTM-North September 2019 (yellow lines), up to 8.7289×10^6m UTM-North by June 2020 (blue lines) and to 8.729×10^6m UTM-North by December 2020 (brown line, visible only in gt2l due to partial cloud cover). Again, these changes are reflected in Figure 11 where increased roughness is observed from 2019 to 2020 at locations near the NAMM in upper Negribreen. Additional evidence of crevasse expansion along and across the NAMM is given in 13(e)-(f) for RGT 152 gt3r which surveys Negribreen just up-glacier of RGT 1334 gt1l/r.

Our ICESat-2 results of fresh crevassing in mid and upper Negribreen around the NAMM indicate an expansion of shear margin disintegration up-glacier from a retreating bay at the terminus. Taken together, the NAMM disintegration and the retreating bays at the terminus illustrate the evolution of a shear margin with a very strong velocity gradient along a folded moraine (see velocity maps in Figure 5). This result demonstrates how time series of ICESat-2 data, analyzed with the DDA-ice, can be employed to derive quantitative information about complex surge processes, here, transverse deformation across a medial moraine forming a shear margin with increasingly large stress gradients as the surge evolves. To our knowledge, this is a new capability of satellite-based observation.

For Peer Review

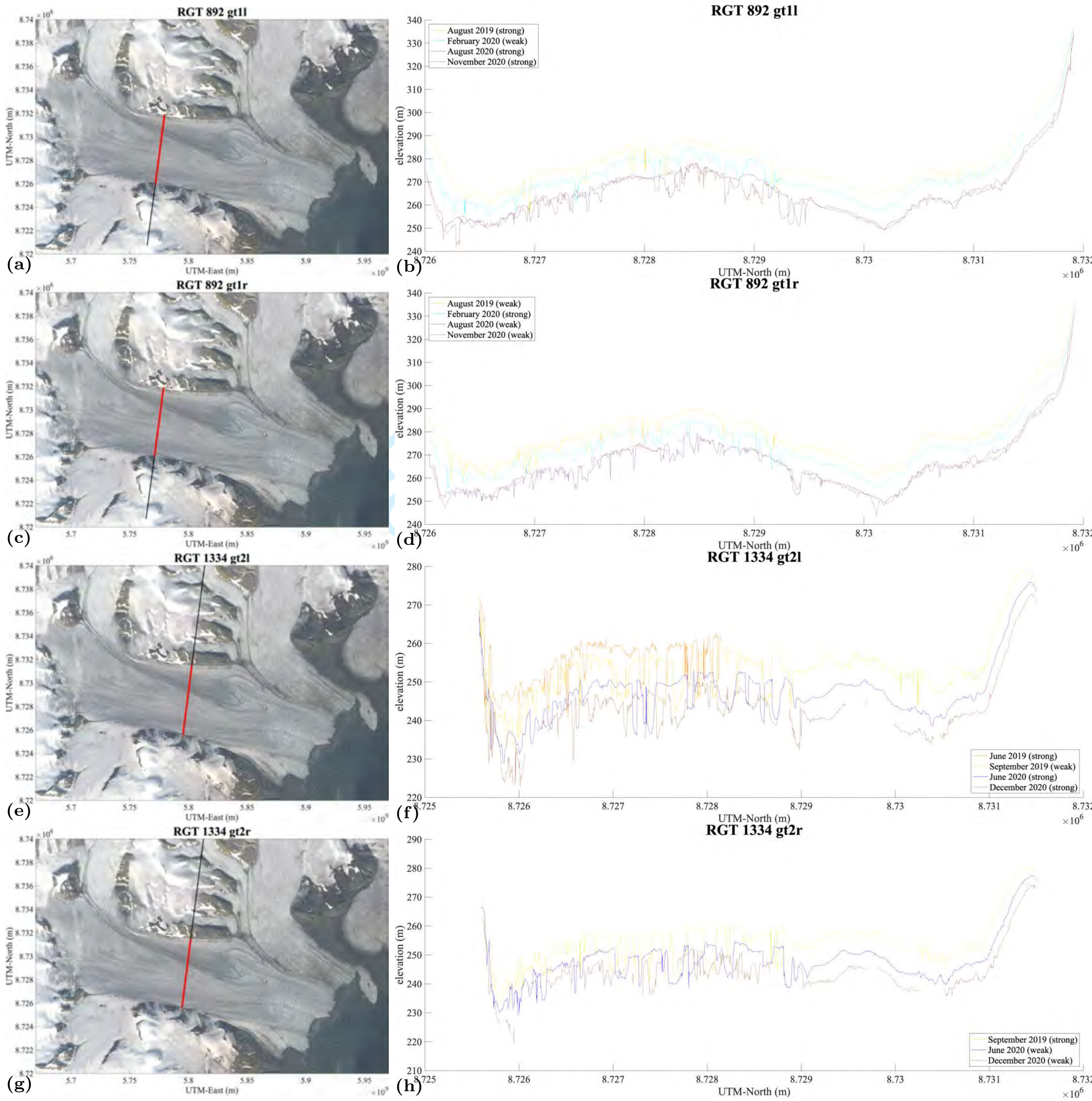

Fig. 14. DDA-ice results near the Negribreen-Akademikarbreen Medial Moraine (NAMM), 2019-2020. (a)-(b) RGT 892 gt1l, (c)-(d) RGT 892 gt1r, (e)-(f) RGT 1334 gt2l, and (g)-(h) RGT 1334 gt2r.

4.3.3. Disintegration of the Ordonnansbreen Tooth

The Ordonnansbreen tooth, a small area of ice indicated by a black arrow in Figure 1(e), has been detaching from Ordonnansbreen's north terminus since the surge began in 2016. As noted earlier, Ordonnansbreen has been moving at quiescent speeds throughout our total observation time (2016-2021)), as seen in the velocity maps of Figure 5.

The detaching tooth, along with the greater disintegration of the ice along the nearby medial moraine (lower NAMM), is visualized in the time series of Landsat-8 RGB imagery from 2018-2021 in Figure 1. In 2018 (Fig. 1(b)) the tooth is attached to the northern part of the Ordonnansbreen terminus. The tooth's connection with the terminus shrinks by August 2019 (Fig. 1(c)) and becomes totally disconnected by July 2020 (Fig. 1(d)). Ordonnansbreen's terminus rapidly retreats between July 2020 and August 2021 (Fig. 1(e)), greatly increasing the distance between the shore-fast tooth and the calving front. While the Landsat-8 imagery helps visualize this process in two spatial dimensions, only with the ICESat-2 data do we get surface height and rifting-depth information to elucidate the third dimension of this rapidly changing glacial feature.

We see the separation of Ordonnansbreen's tooth in the time series of RGT 91 gt3l and gt3r (Figure 15), which both cross the terminus of Ordonnansbreen. The orange line in Figure 15, representing the ice-surface in April 2019, shows continuous ice extending from the shore line at 8.73×10^6m UTM-North to the calving front near 8.7274×10^6m UTM-North. By January 2020, a ∼10 m deep rift developed near 8.7299×10^6m UTM-North that penetrates all the way to the ocean surface, disconnecting the majority of the tooth from the main glacier (see cyan-colored line in Figure 15). The rift geometry at this location appears to have remained relatively fixed between January 2020 (cyan) and July 2020 (purple, gt3l only) indicating little surge activity during this time. By September 2020 (brown lines), the rift between Ordonnansbreen and the tooth increased significantly from ∼400 m to over 1.5 km in the direction of the RGT 91 survey line. The September 2020 results in RGT 91 gt3r (Figure 15(d)) in particular, indicate the presence large icebergs and an even greater separation distance nearing 5 km between the tooth and the main glacier. These results indicate that the process of tooth detachment occurs most rapidly during peak glacier velocities in late summer implying that the initial rift likely developed sometime around July or August 2019.

Looking at the entirety of the RGT 91 gt3l/r survey lines, we observe an ice-surface lowering of 4-5 m across the Ordonnansbreen terminus during the 15 months between April 2019 and July 2020, i.e., approximately 20% of its total thickness, indicating rapid height and mass loss. This ice-surface continued to lower by ∼1 m across the entire width during the 3 months between July and September 2020. Therefore, while the majority of Ordonnansbreen remains in a quiescent state, the Negribreen surge still has a significant effect on the evolution of its neighboring tributary glacier through dramatic surface lowering, rifting and calving at the terminus. The surge effects here, along with the major deformation along its

For Peer Review

medial moraine with Negribreen (lower NAMM), leave the future state of Ordonnansbreen uncertain as the NGS surge continues to progress.

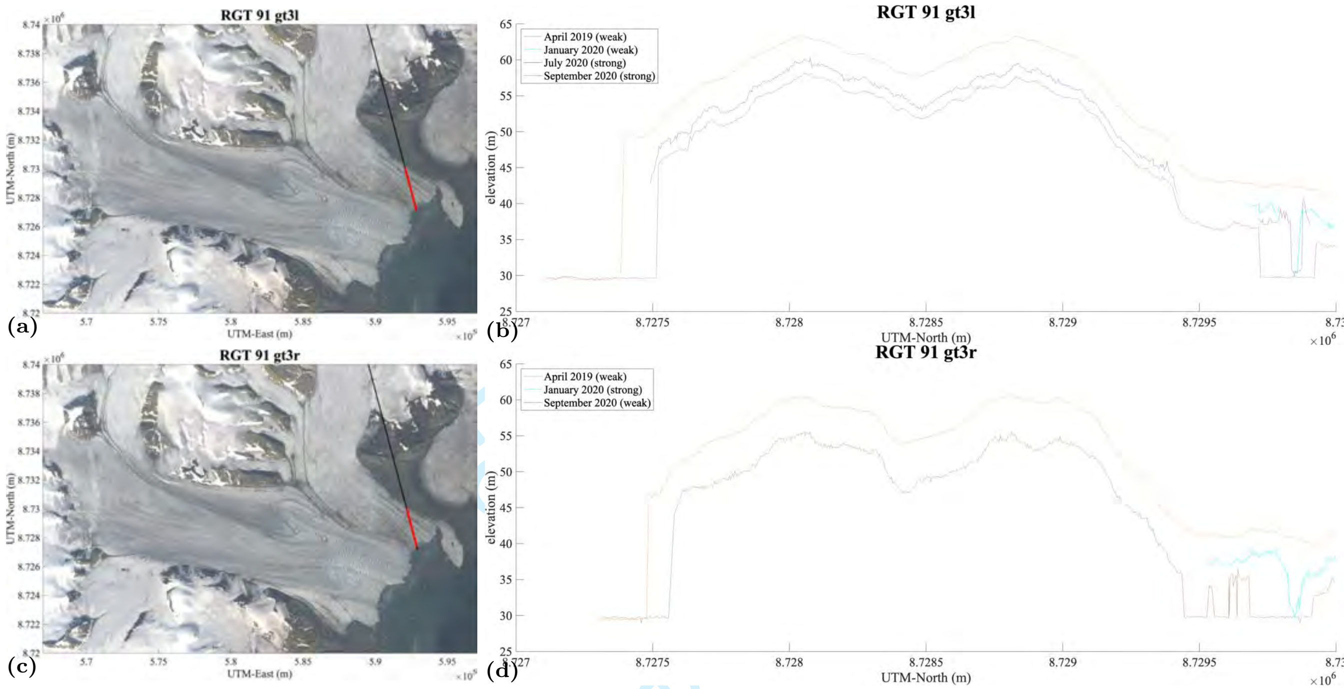

Fig. 15. DDA-ice results over Ordonnansbreen's terminus and the Ordonnansbreen tooth, 2019-2020. (a)-(b) RGT 91 gt3l shows the disintegration of Ordonnansbreen's terminus at its northern edge, i.e., at the tooth, above 8.729e6 UTM-North. (c)-(d) RGT 91 gt3r also displays the signal of a disintegrating northern terminus of Ordonnansbreen. Both time series also show significant surface lowering across the terminus width.

4.3.4. Changes in the Ice Falls between the Filchnerfonna and Upper Negribreen

The ice falls between Filchnerfonna and upper Negribreen have been areas of pervasive change during the 2019-2020 part of the surge in the NGS, as observed during our 2019 field campaign (Herzfeld and others, 2022). While ice falls are characterized by heavy crevassing due to steep topography, the imprint of the surge manifests through fresh crevasse openings along with the widening and deepening of existing crevasses. Figure 16 shows distinct signs of activity in the ice falls, indicative of expansion of the surge-affected area beyond the NGS. Surge activity is most pronounced in the southern ice falls where increased crevassing occurs (Figures 16(b),(d)). Increased crevassing is not as prevalent along the inflowing Transparentbreen, which is less steep than the other inflowing glaciers from Filchnerfonna, however, there is a pronounced surface lowering across its entire width. The rate of surface-height lowering here is increasing as seen by the spacing of the later 2020 lines (purple, brown) compared to the earlier 2019 lines (yellow, green), indicating building surge effects on Transparentbreen.

An important observation in the context of expansion of the surge beyond the NGS, our results motivate the question whether the surge in the NGS may induce a disintegration of the surrounding glacial area, potentially destabilizing the Filchnerfonna. A less dramatic interpretation is that significant surface lowering in the NGS leads to draw-down of ice flowing through the ice falls. Either way, the surge in the NGS is affecting adjacent ice areas at the border of its accumulation zone.

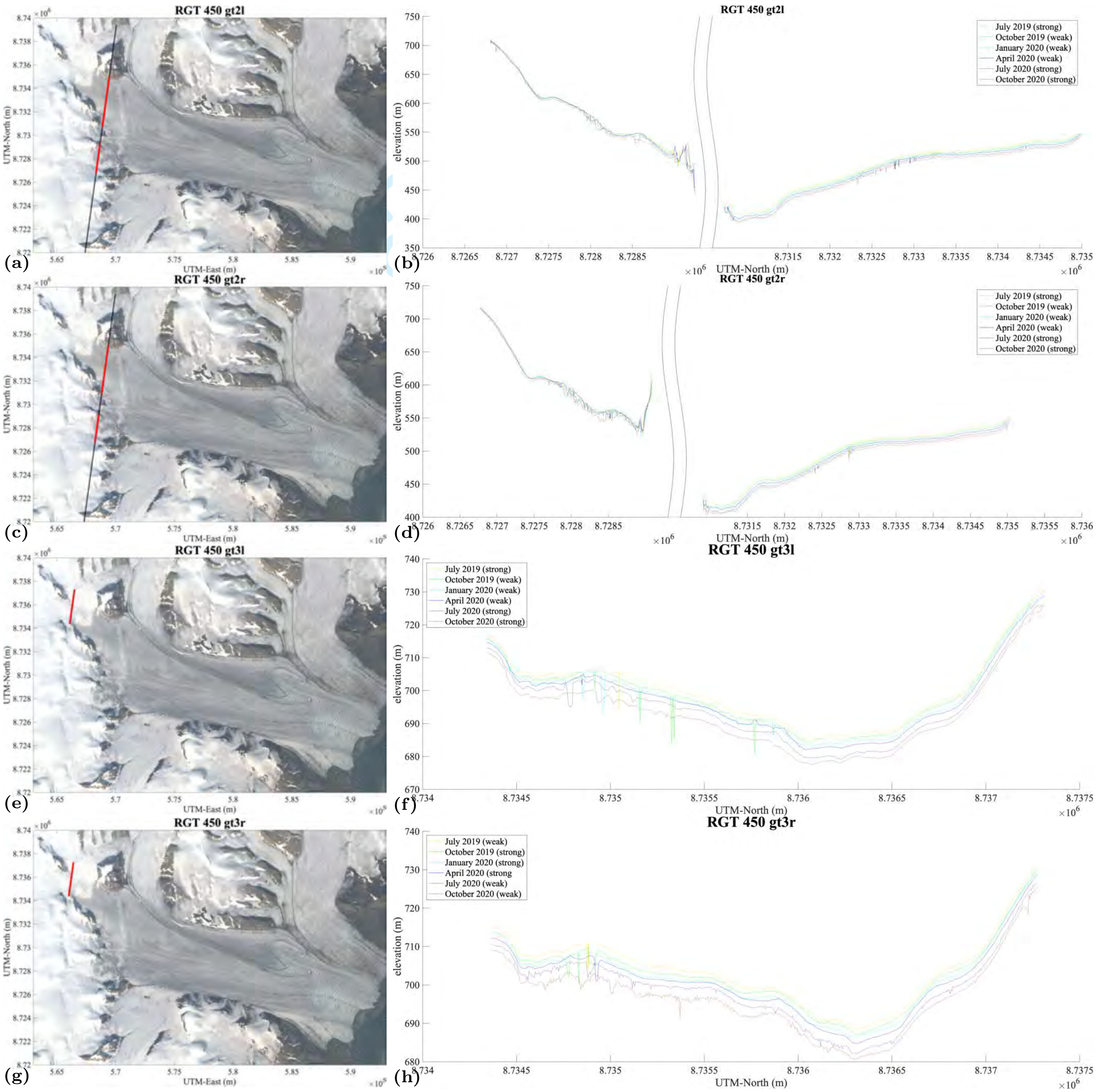

Fig. 16. DDA-ice results near the inflow from Filchnerfonna, 2019-2020. (a)-(b) RGT 450 gt2l surveying both the southern ice falls and Transparentbreen in the north, (c)-(d) RGT 450 gt2r surveying the ice falls and Transparentbreen, (e)-(f) RGT 450 gt3l surveying only Transparentbreen, and (g)-(h) RGT 450 gt3r also surveying only Transparentbreen.

4.3.5. General Mass Transfer Observations

The surface height changes of 2019-2020 given by Figure 8, reflect significant mass transfer from the reservoir area in upper and mid Negribreen down-glacier to the receiving area in the lower glacier within 5 km of the terminus. The ice-mass transferred to the receiving area is eventually transported to the Arctic Ocean via heavy calving during the surge. These mass transfer observations are further detailed in the analysis of surface height time series of the proceeding sections.

In total, the ICESat-2 results gives a clear indication that the mass transfer is surge induced rather than climatically induced. As seen most clearly in Figures 12(b) and 13(d), surface height profiles overlie each other at the beginning and end of each track (i.e., on the non-surging tributary glaciers on the sides of Negribreen) but significant height change is apparent along the interior of the profile. If surface lowering were climatically caused (mass loss through melting), then similar height changes between 2019 and 2020 would be observed across the entire profile.

5. CONCLUSIONS

In this paper, we have derived information on geophysical processes that occurred during the surge of Negribreen Glacier System based on analysis of 2 years of ICESat-2 ATLAS data from 2019 and 2020, processed with the DDA-ice. ICESat-2 data, analyzed with the DDA-ice, provide a unique and novel capability to obtain geophysical information on high resolution height changes during a glacier surge from spaceborne altimeter observations. The NGS provides an ideal study region as the main acceleration phase of the surge overlaps with the observation phase of the ICESat-2 mission. Negribreen's surge started in 2016, with peak acceleration in 2017, while ICESat-2 launched on 15 September 2018. Here we have analyzed all ICESat-2 data collected between January 2019 and December 2020 over Negribreen to demonstrate our approach. The analysis is supplemented with velocity maps from Sentinel-1 SAR imagery and airborne data from our August 2019 campaign to Negribreen.

Geophysical information on the evolution of the surge is derived from the ICESat-2/DDA-ice high resolution data, including: crevassing, height changes, mass transfer toward the terminus and roughness changes indicative of evolving crevasse fields. Height-change rates in 2019-2020 range from -30m/yr in the reservoir areas of upper Negribreen, to +30 m/yr in the receiving area in the lower glacier near the terminus. Roughness change maps indicate an expansion of the surge in upper Negribreen, particularly near the shear margins, while surge activity in the lower glacier lessened from 2019 to 2020.

For Peer Review

Time series analysis of ICESat-2 profiles, analyzed with the DDA-ice, indicates formation of new crevasse fields and expansion of existing crevasse fields, as the surge progresses and affects larger areas of the NGS. The increased surge activity from 2019 to 2020 in the upper glacier is especially seen on the inflowing glaciers from the Filchnerfonna accumulation zone, and along the Negribreen-Akademikarbreen Medial Moraine, which divides the surging ice of Negribreen and the non-surging ice of the northern tributary glaciers.

The fresh surge crevassing along and across the NAMM in the mid and upper glacier in 2019-2020 indicates disintegration along the shear margin and reflects a continuation of the deformational process that resulted in a "retreating bay", an area of open water filled with melange that formed as a result of a strong force gradient along the shear margin between the surging ice of Negribreen and non-surging ice of neighboring Ordonnansbreen, near the terminus in 2017. Occurrence of water in crevasses that reaches almost to the ice surface height was observed near the upper NAMM in August 2019, just before the new crevasses were formed. Furthermore, our analysis of surge progression in 2019-2020 provided detailed height information on the separation process of a segment of lower Ordonnansbreen ("Ordonnansbreen tooth") from the main glacier along a rift that had formed during the surge.

Large-scale mass transfer, extensive roughness changes, and the striking disintegration along the NAMM, and of Ordonnansbreen's tooth and the lower glacier as a whole, clearly illustrate the rapid surface change and mass loss a glacier can experience during a surge. These results demonstrate the novel capability of ICESat-2, analyzed with the DDA-ice, to provide high-resolution height data uniquely capable of documenting these complex surge processes from space.

For Peer Review

DATA AVAILABILITY

(1) ICESat-2 data products, e.g. ATL03, are freely available through NASA at https://earthdata.nasa.gov/ (release 4 used in this paper) and is provided by the National Snow and Ice Data Center (NSIDC). (2) Data collected as part of the Negribreen Airborne Geophysical Campaigns, collected by the authors and their extended team, are available through the NSF Arctic Data Center and can be accessed at https://arcticdata.io/data/10.18739/A2QF8JK7T (Herzfeld and Trantow, 2021). (3) Sentinel-1 SAR data are freely available through the the European Space Agency's Copernicus Open Access Hub (https://scihub.copernicus.eu/). (4) Landsat-8 data are freely available through the U.S. Geological Survey, e.g., through the USGS Global Visualization Viewer (GloVis) (https://glovis.usgs.gov/).

ACKNOWLEDGEMENTS

Thanks are due to our pilot and technician, Harald Sandal and Gustav Svanstrom, Airlift, Norway, of the 2019 Negribreen campaign, to Matt Lawson, Geomathematics Group, University of Colorado Boulder, for help with data collection in 2019, to Jack Kohler, Geir Ove Aspnes, Jørn Dybdahl, Norwegian Polar Institute, to Chris Borstad, University Center in Svalbard (UNIS), now University of Montana, to Thomas Nylen and UNAVCO Boulder for GPS support, to Inger Jennings (SIOS) and Kristin Woxholth, Longyearbyen, for help with logistical support, to the ICESat-2 Project, especially Thomas Neumann, Kaitlin Harbeck, David Hancock and Anthony Martino for collaboration and support regarding ICESat-2, to Huilin Han and Rachel Middleton, Geomathematics Group, University of Colorado Boulder, for derivation of some of the velocity maps from Sentinel-1 SAR data and to the European Space Agency for providing the SNAP tool for velocity-map calculation.

Research and data collection were supported by the U.S. National Aeronautics and Space Administration (NASA) Earth Sciences Division under awards 80NSSC20K0975, 80NSSC18K1439 and NNX17AG75G and by the U.S. National Science Foundation (NSF) under awards OPP-1745705 and OPP-1942356 (Office of Polar Programs) and OAC-1835256 (Office of Advanced Cyberinfrastructure); Principal Investigator for all awards is Ute Herzfeld. The helicopter was provided by the Norwegian Polar Institute and operated by Airlift. Collection of airborne data was conducted with permission of the National Security Authority of Norway, the Civil Aviation Authority of Norway and the Governor of Svalbard, registered as Research in Svalbard Project RIS-10827 "NEGRIBREEN SURGE". The data collection was also partly supported through a 2018 Access Pilot Project (2017_0010) of the Svalbard Integrated Observing System (SIOS). All this support is gratefully acknowledged.

For Peer Review

SUPPLEMENTAL MATERIAL

The supplementary material for this article can be found at [link TBD]. There are two documents provided:

1. negri_data_2019_2020.xlsx: A CSV file providing information on the ATL03 granule, acquisition date and run names for each DDA-ice run (one for each beam per pass from 2019-2020). This file contains the information in Table 2 as well.

2. negri.change.suppl.pdf: A figure file containing a full collection of enlarged ICESat-2 time series plots for all beams and RGTs.

REFERENCES

Banerjee D, Garg V and Thakur PK (2022) Geospatial investigation on transitional (quiescence to surge initiation) phase dynamics of Monacobreen tidewater glacier, Svalbard. *Advances in Space Research*, **69**(4), 1813–1839

Bhambri R, Hewitt K, Kawishwar P and Pratap B (2017) Surge-type and surge-modified glaciers in the Karakoram. *Scientific reports*, **7**(1), 15391

Björnsson H (1998) Hydrological characteristics of the drainage system beneath a surging glacier. *Nature*, **395**(6704), 771

Björnsson H, Pálson F, Siggurdsson O and Flowers G (2003) Surges of glaciers in Iceland. *Annals of Glaciology*, **36**, 82–90

Chen D, Rojas M, Samset B, Cobb K, Diongue Niang A, Edwards P, Emori S, Faria S, Hawkins E, Hope P, Huybrechts P, Meinshausen M, Mustafa S, Plattner GK and Tréguier AM (2021) *Climate Change 2021: The Physical Science Basis. Contribution of Working Group I to the Sixth Assessment Report of the Intergovernmental Panel on Climate Change*, 147–286. Cambridge University Press, Cambridge, United Kingdom and New York, NY, USA (doi: 10.1017/9781009157896.003)

Clarke G (1987) Fast glacier flow: Ice streams, surging, and tidewater glaciers. *Journal of Geophysical Research*, **92**, 8835–8842

Cuffey K and Paterson WSB (2010) *The Physics of Glaciers*. Elsevier, 4th edition

de Boer G, Eloranta EW and Shupe MD (2009) Arctic mixed-phase stratiform cloud properties from multiple years of surface-based measurements at two high-latitude locations. *Journal of the Atmospheric Sciences*, **66**(9), 2874–2887

Dolgushin L and Osipova G (1975) Glacier surges and the problem of their forecast. *Symposium on snow and ice in mountain regions*, **104**, 292–304

Dowdeswell J, Drewry D, Liestøl O and Orheim O (1984) Radio echo-sounding of Spitsbergen glaciers: problems in the interpretation of layer and bottom returns. *Journal of Glaciology*, **30**(104), 16–21

Flowers GE, Roux N, Pimentel S and Schoof CG (2011) Present dynamics and future prognosis of a slowly surging glacier. *The Cryosphere*, **5**, 299–313

Geudtner D, Torres R, Snoeij P, Davidson M and Rommen B (2014) Sentinel-1 system capabilities and applications. In *Geoscience and Remote Sensing Symposium (IGARSS), 2014 IEEE International*, 1457–1460, IEEE

Gierens R, Kneifel S, Shupe MD, Ebell K, Maturilli M and Löhnert U (2020) Low-level mixed-phase clouds in a complex Arctic environment. *Atmospheric Chemistry and Physics*, **20**(6), 3459–3481

Guan W, Cao B, Pan B, Chen R, Shi M, Li K, Zhao X and Sun X (2022) Updated surge-type glacier inventory in the West Kunlun Mountains, Tibetan Plateau, and implications for glacier change. *Journal of Geophysical Research: Earth Surface*, **127**(1), e2021JF006369

For Peer Review

Guillet G, King O, Lv M, Ghuffar S, Benn D, Quincey D and Bolch T (2022) A regionally resolved inventory of High Mountain Asia surge-type glaciers, derived from a multi-factor remote sensing approach. *The Cryosphere*, **16**(2), 603–623

Haga ON, McNabb R, Nuth C, Altena B, Schellenberger T and Kääb A (2020) From high friction zone to frontal collapse: dynamics of an ongoing tidewater glacier surge, Negribreen, Svalbard. *Journal of Glaciology*, **66**(259), 742–754

Harrison W and Post A (2003) How much do we really know about glacier surging? *Annals of Glaciology*, **36**(1), 1–6

Herzfeld U, McDonald B and Weltman A (2013a) Bering Glacier and Bagley Ice Valley surge 2011: Crevasse classification as an approach to map deformation stages and surge progression. *Annals of Glaciology*, **54(63)**, 279–286 (doi: 10/3189/2013AoG63A338)

Herzfeld U, Trantow T, Lawson M, Hans J and Medley G (2021) Surface heights and crevasse types of surging and fast-moving glaciers from ICESat-2 laser altimeter data — Application of the density-dimension algorithm (DDA-ice) and validation using airborne altimeter and Planet SkySat data. *Science of Remote Sensing*, **3**, 1–20 (doi: 10.1016/j.srs.2020.100013)

Herzfeld U, Trantow T, Buckley E, Farrell S and Lawson M (2023) Automated detection and depth measurement of melt ponds on sea ice from ICESat-2 ATLAS data — the DDA-bifurcate-seaice. *IEEE Transactions of Geoscience and Remote Sensing*, 1–16 (doi: 10.1109/TGRS.2023.326807), published April 18, 2023

Herzfeld UC (2008) Master of the obscure — Automated geostatistical classification in presence of complex geophysical processes. *Mathematical Geosciences*, **40**(5), 587–618 (doi: 10.1007/s11004-008-9174-4)

Herzfeld UC and Mayer H (1997) Surge of Bering Glacier and Bagley Ice Field, Alaska: an update to August 1995 and an interpretation of brittle-deformation patterns. *Journal of Glaciology*, **43**(145), 427–434

Herzfeld UC and Trantow T (2021) Airborne Laser Altimeter, Global Positioning System (GPS), Inertial Measurement Unit (IMU) and Imagery Campaign of the Surging Negribreen Glacier, Svalbard, in July 2017 and July 2018. https://arcticdata.io/catalog/view/doi:10.18739/A23J39249 (doi: 10.18739/A23J39249)

Herzfeld UC, McDonald B, Stachura M, Hale RG, Chen P and Trantow T (2013b) Bering Glacier surge 2011: Analysis of laser altimeter data. *Annals of Glaciology*, **54(63)**, 158–170 (doi: 10.3189/2013AoG63A348)

Herzfeld UC, McDonald B, Wallin BF, Krabill W, Manizade S, Sonntag J, Mayer H, Yearsley WA, Chen PA and Weltman A (2014) Elevation changes and dynamic provinces of Jakobshavn Isbræ, Greenland, derived using generalized spatial surface roughness from ICESat GLAS and ATM data. *Journal of Glaciology*, **60**(223), 834–848

Herzfeld UC, Trantow TM, Harding D and Dabney PW (2017) Surface-height determination of crevassed glaciers – Mathematical principles of an autoadaptive density-dimension algorithm and validation using ICESat-2 simulator (SIMPL) data. *IEEE Transactions on Geoscience and Remote Sensing*, **55**(4), 1874–1896 (doi: 10.1109/TGRS.2016.2617323)

For Peer Review

Herzfeld UC, Lawson M, Trantow T and Nylen T (2022) Airborne validation of icesat-2 atlas data over crevassed surfaces and other complex glacial environments: Results from experiments of laser altimeter and kinematic gps data collection from a helicopter over a surging arctic glacier (negribreen, svalbard). *Remote Sensing*, **14**(5), 1185

Jiskoot H (2011) Glacier surging. *Encyclopedia of Snow, Ice and Glaciers*, 415–428

Jiskoot H, Murray T and Luckman A (2003) Surge potential and drainage-basin characteristics in East Greenland. *Annals of Glaciology*, **36**, 142–148

Kääb A, Bazilova V, Leclercq PW, Mannerfelt ES and Strozzi T (2023) Global clustering of recent glacier surges from radar backscatter data, 2017–2022. *Journal of Glaciology*, 1–9

Kamb W, Raymond C, Harrison W, Engelhardt H, Echelmeyer K, Humphrey N, Brugman M and Pfeffer T (1985) Glacier surge mechanism: 1982-1983 surge of Variegated Glacier, Alaska. *Science*, **227**(4686), 469–479

Kamb WB (1987) Glacier Surge Mechanism Based on Linked Cavity Configuration of the Basal Water Conduit System. *Journal Geophys. Res.*, **92**(B9), 9083–9100

Kochtitzky W, Winski D, McConnell E, Kreutz K, Campbell S, Enderlin EM, Copland L, Williamson S, Main B and Jiskoot H (2020) Climate and surging of Donjek glacier, Yukon, Canada. *Arctic, Antarctic, and Alpine Research*, **52**(1), 264–280

Lee H, Shum C, Tseng K, Huang Z and Sohn H (2013) Elevation changes of Bering Glacier System, Alaska, from 1992 to 2010, observed by satellite radar altimetry. *Remote Sensing of the Environment*, **132**, 40–48 (doi: dx.doi.org/10.1016/j.rse.2013.01.007)

Lefauconnier B and Hagen JO (1991) *Surging and calving glaciers in eastern Svalbard*. Norsk Polarinstitutt

Luckman A, Murray T and Strozzi T (2002) Surface flow evolution throughout a glacier surge measured by satellite radar interferometry. *Geophysical research letters*, **29**(23), 10–1

Luthcke S, Thomas T, Pennington T, Rebold T, Nicholas J, Rowlands D, Gardner A and Bae S (2021) Icesat-2 pointing calibration and geolocation performance. *Earth and Space Science*, **8**(3), e2020EA001494

Magruder L, Neumann T and Kurtz N (2021) Icesat-2 early mission synopsis and observatory performance. *Earth and Space Science*, **8**(5), e2020EA001555

Markus T, Neumann T, Martino A, Abdalati W, Brunt K, Csatho B, Farrell S, Fricker H, Gardner A, Harding D and others (2017) The Ice, Cloud, and land Elevation Satellite-2 (ICESat-2): Science requirements, concept, and implementation. *Remote Sensing of Environment*, **190**, 260–273

Martino AJ, Neumann TA, Kurtz NT and McLennan D (2019) Icesat-2 mission overview and early performance. In *Sensors, systems, and next-generation satellites XXIII*, volume 11151, 68–77, SPIE

Mayer H and Herzfeld U (2000) Structural glaciology of the fast-moving Jakobshavn Isbræ, Greenland, compared to the surging Bering Glacier, Alaska, USA. *Annals of Glaciology*, **30**(1), 243–249

Meier M and Post A (1969) What are glacier surges? *Canadian Journal of Earth Sciences*, **6**(4), 807–817

For Peer Review

Molnia B and Post A (1995) Holocene history of Bering Glacier, Alaska: A prelude to the 1993-1994 surge. *Physical Geography*, **16**(2), 87–117

Murray T, Strozzi T, Luckman A, Jiskoot H and Christakos P (2003) Is there a single surge mechanism? Contrasts in dynamics between glacier surges in Svalbard and other regions. *Journal of Geophysical Research: Solid Earth*, **108**(B5)

Neumann T, Brenner A, Hancock D, Robbins J, Saba J, Gibbons A, Lee J, Luthcke S and Rebold T (2020a) ATLAS/ICESat-2 L2A Global Geolocated Photon Data, Version 5 (doi: 10.5067/ATLAS/ATL03.004)

Neumann T, Brenner A, Hancock D, Robbins J, Saba J, Harbeck K, Gibbons A, Lee J, Luthcke S and Rebold T (2020b) *ICESat-2 Algorithm Theoretical Basis Document for Global Geolocated Photons, April 2020*. NASA ICESat-2 Project (doi: 10.5067/ESL18THQ8RNT), 207p

Neumann TA, Martino AJ, Markus T, Bae S, Bock MR, Brenner AC, Brunt KM, Cavanaugh J, Fernandes ST, Hancock DW and others (2019) The Ice, Cloud, and Land Elevation Satellite–2 mission: A global geolocated photon product derived from the Advanced Topographic Laser Altimeter System. *Remote Sensing of Environment*, **233**, 111325 (doi: 10.1016/j.rse.2019.111325)

Nuth C, Gilbert A, Köhler A, McNabb R, Schellenberger T, Sevestre H, Weidle C, Girod L, Luckman A and Kääb A (2019) Dynamic vulnerability revealed in the collapse of an Arctic tidewater glacier. *Scientific reports*, **9**(1), 5541

Post A (1972) Periodic surge origin of folded medial moraines on Bering Piedmont Glacier, Alaska. *Journal of Glaciology*, **11**(62), 219–226

Roy DP, Wulder M, Loveland TR, Woodcock C, Allen R, Anderson M, Helder D, Irons J, Johnson D, Kennedy R and others (2014) Landsat-8: Science and product vision for terrestrial global change research. *Remote sensing of Environment*, **145**, 154–172

Sevestre H, Benn DI, Hulton NR and Bælum K (2015) Thermal structure of Svalbard glaciers and implications for thermal switch models of glacier surging. *Journal of Geophysical Research: Earth Surface*, **120**(10), 2220–2236

Shupe MD, Matrosov SY and Uttal T (2006) Arctic mixed-phase cloud properties derived from surface-based sensors at SHEBA. *Journal of the atmospheric sciences*, **63**(2), 697–711

Shupe MD, Walden VP, Eloranta E, Uttal T, Campbell JR, Starkweather SM and Shiobara M (2011) Clouds at Arctic atmospheric observatories. Part I: Occurrence and macrophysical properties. *Journal of Applied Meteorology and Climatology*, **50**(3), 626–644

Smith B, Hancock D, Harbeck K, Roberts L, Neumann T, Brunt K, Fricker H, Gardner A, Siegfried M, Adusumilli S, Csatho B, Holschuh N, Nilsson J and Paolo F (2020) *ICESat-2 Algorithm Theoretical Basis Document for Land Ice Along-Track Height Product, February 20, 2020*. NASA ICESat-2 Project, Greenbelt, Maryland, U.S.A. (doi: 10.5067/A8SP5FCJLWR0), 107p

For Peer Review

Strozzi T, Paul F, Wiesmann A, Schellenberger T and Kääb A (2017) Circum-Arctic changes in the flow of glaciers and ice caps from satellite SAR data between the 1990s and 2017. *Remote Sensing*, **9**(9), 947

Trantow T (2020) *Surging in the Bering-Bagley Glacier System, Alaska – Understanding Glacial Acceleration through New Methods in Remote Sensing, Numerical Modeling and Model-Data Comparison*. Ph.D. thesis, University of Colorado

Trantow T and Herzfeld UC (2018) Crevasses as indicators of surge dynamics in the Bering Bagley Glacier System, Alaska: Numerical experiments and comparison to image data analysis. *Journal of Geophysical Research: Earth Surface* (doi: 10.1029/2017JF004341)

Truffer M and Echelmeyer KA (2003) Of isbrae and ice streams. *Annals of Glaciology*, **36**(1), 66–72

Truffer M, Kääb A, Harrison WD, Osipova GB, Nosenko GA, Espizua L, Gilbert A, Fischer L, Huggel C, Burns PAC and others (2021) Glacier surges. In *Snow and ice-related hazards, risks, and disasters*, 417–466, Elsevier

Vale AB, Arnold NS, Rees WG and Lea JM (2021) Remote detection of surge-related glacier terminus change across High Mountain Asia. *Remote Sensing*, **13**(7), ISSN 2072-4292 (doi: 10.3390/rs13071309)

Willis MJ, Zheng W, Durkin IV WJ, Pritchard ME, Ramage JM, Dowdeswell JA, Benham TJ, Bassford RP, Stearns LA, Glazovsky AF and others (2018) Massive destabilization of an arctic ice cap. *Earth and Planetary Science Letters*, **502**, 146–155

Wuite J, Libert L, Nagler T and Jóhannesson T (2022) Continuous monitoring of ice dynamics in Iceland with Sentinel-1 satellite radar images. *Jökull*, **72**, 1–20

Yao X, Zhou S, Sun M, Duan H and Zhang Y (2023) Surging glaciers in High Mountain Asia between 1986 and 2021. *Remote Sensing*, **15**(18), 4595

Zwally H, Schutz B, Abdalati W, Abshire J, Bentley C, Brenner A, Bufton J, Dezio J, Hancock D, Harding D, Herring T, Minster B, Quinn K, Palm S, Spinhirn J and Thomas R (2002) ICESat's laser measurements of polar ice, atmosphere, ocean, and land. *Journal of Geodynamics*, **34**(3-4), 405–445

For Peer Review

Supplementary Material for Manuscript titled “Progression of the surge in the Negribreen Glacier System from two years of ICESat-2 Measurements”

Thomas Trantow [1,*], **Ute C. Herzfeld** [1]

[1] Department of Electrical, Energy and Computer Engineering, University of Colorado, Boulder, Colorado, USA

The supplementary material in this document provides a complete collection of the ICESat-2/DDA-ice time series for each RGT and beam listed in Table 2 of the paper. Time series plots already present in the paper, along with those absent from the main manuscript, are enlarged in here for visibility. In addition, Figure 2 of the main manuscript is given below (Figure 1) for a visual reference for location of the ICESat-2 RGT beams over the Negribreen Glacier System.

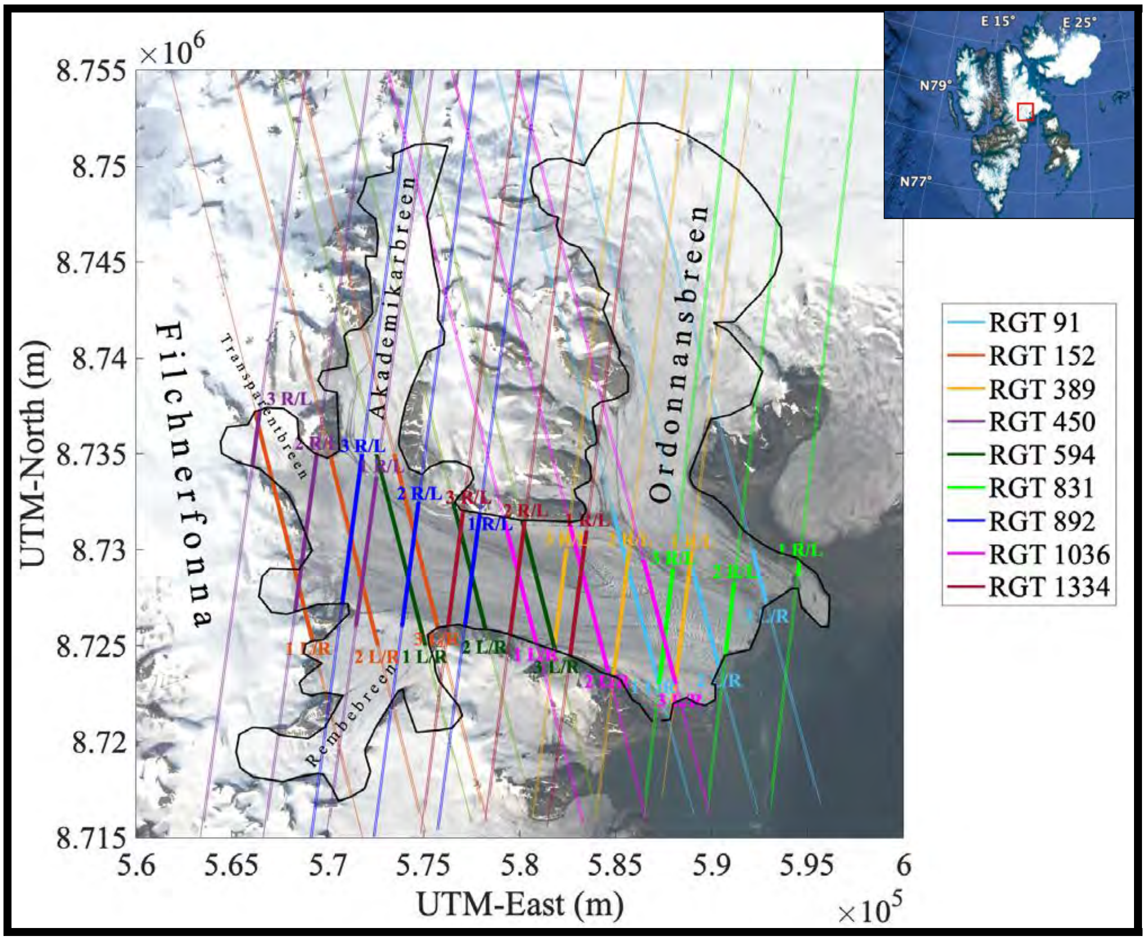

Figure 1: **ICESat-2 survey lines over the Negribreen Glacier System.** NGS location in the Svalbard archipelago indicated by a red box in the upper right inset. The survey lines for each of ICESat-2's three beam-pairs are color coded by their Reference Ground Track (RGT) while the NGS borders are given by the black line. The thick lines correspond to the part of the track that is analyzed in this paper which is mostly equivalent to the boundaries of Negribreen Glacier Proper. Left/Right (L/R) beam-pairs are separated by ∼90 m on-ice which is within line thickness over Negribreen proper in this figure. Background image from Landsat-8 acquired 2019-08-05.

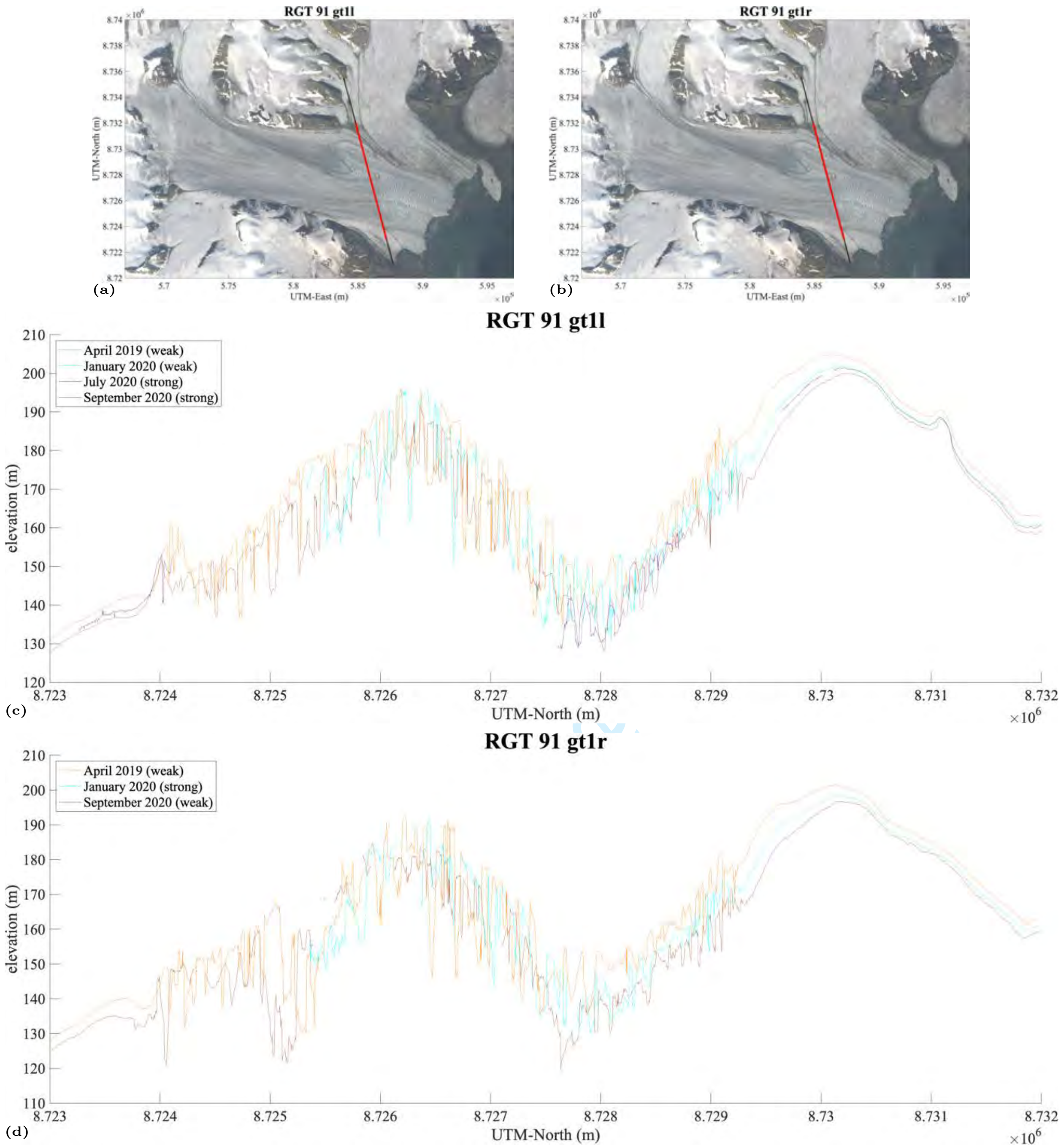

Figure 2: **ICESat-2/DDA-ice surface height time series for RGT 91 beam pair 1 over Negribreen, 2019-2020.** (a) Location of RGT 91 gt1l segment over Negribreen, (b) Location of RGT 91 gt1r segment over Negribreen, (c) surface height time series of RGT 91 gt1l, and (d) surface height time series of RGT 91 gt1r.

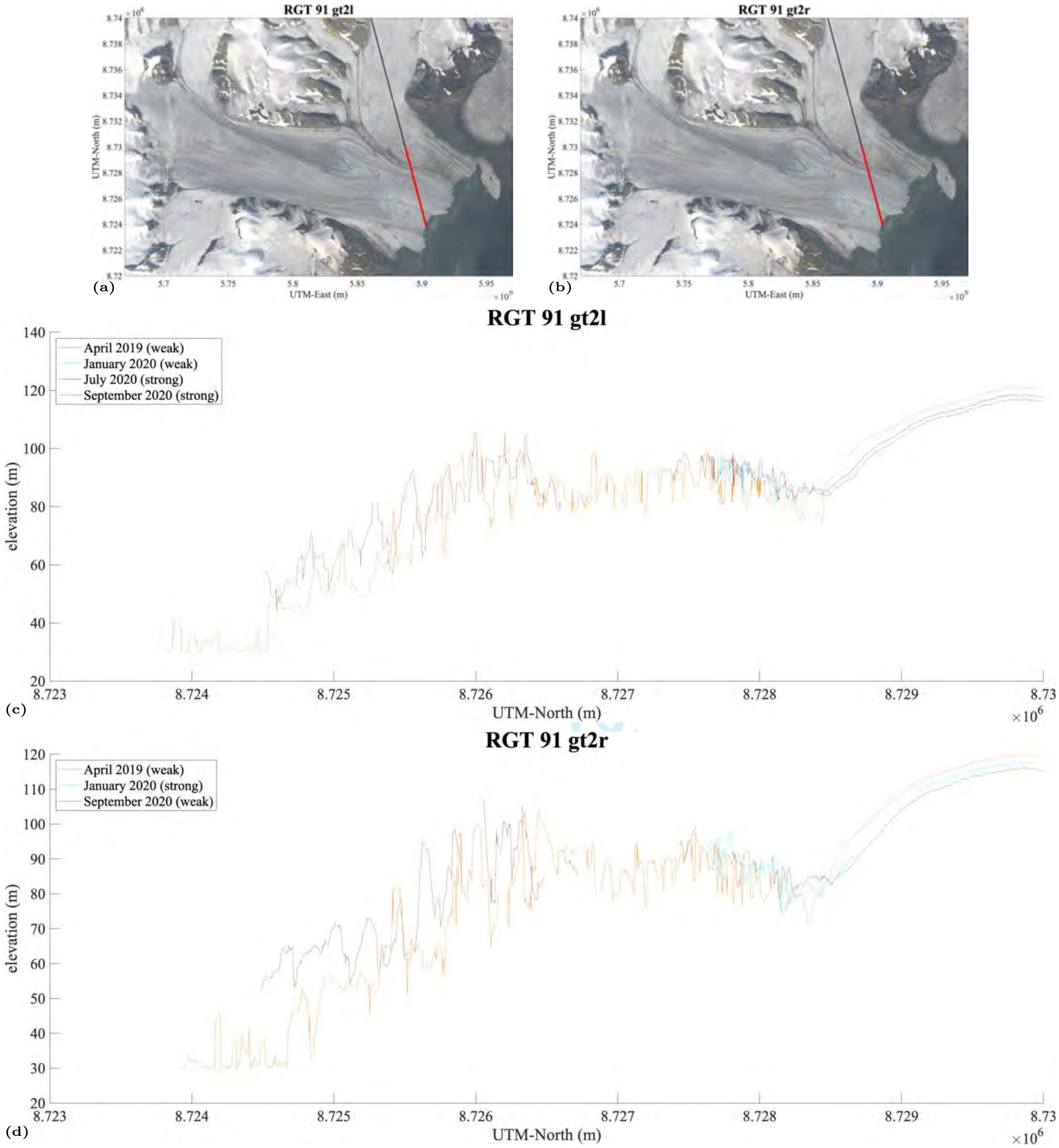

Figure 3: **ICESat-2/DDA-ice surface height time series for RGT 91 beam pair 2 over Negribreen, 2019-2020.** (a) Location of RGT 91 gt2l segment over Negribreen, (b) Location of RGT 91 gt2r segment over Negribreen, (c) surface height time series of RGT 91 gt2l, and (d) surface height time series of RGT 91 gt2r.

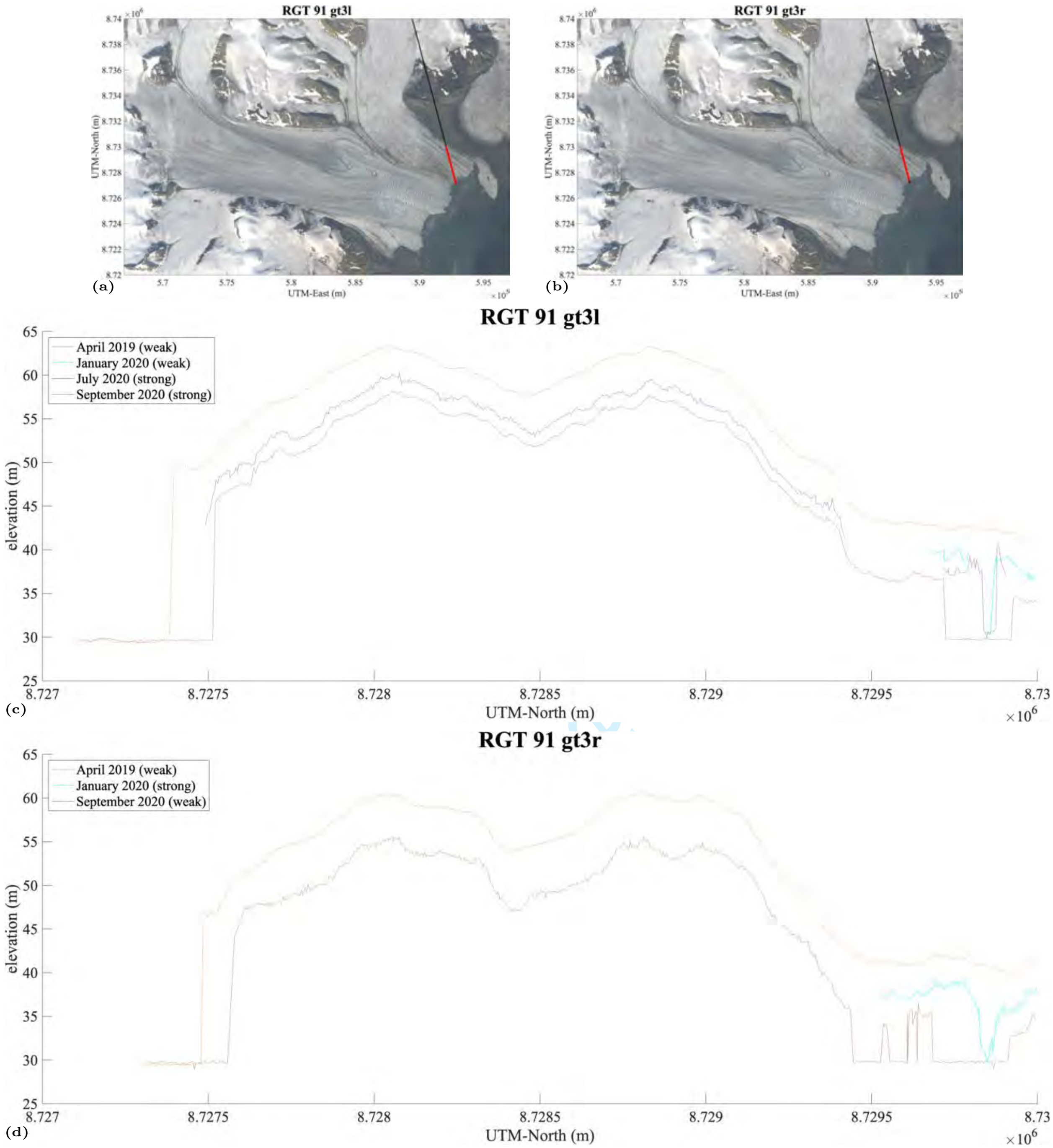

Figure 4: **ICESat-2/DDA-ice surface height time series for RGT 91 beam pair 3 over Negribreen, 2019-2020.** (a) Location of RGT 91 gt3l segment over Negribreen, (b) Location of RGT 91 gt3r segment over Negribreen, (c) surface height time series of RGT 91 gt3l, and (d) surface height time series of RGT 91 gt3r.

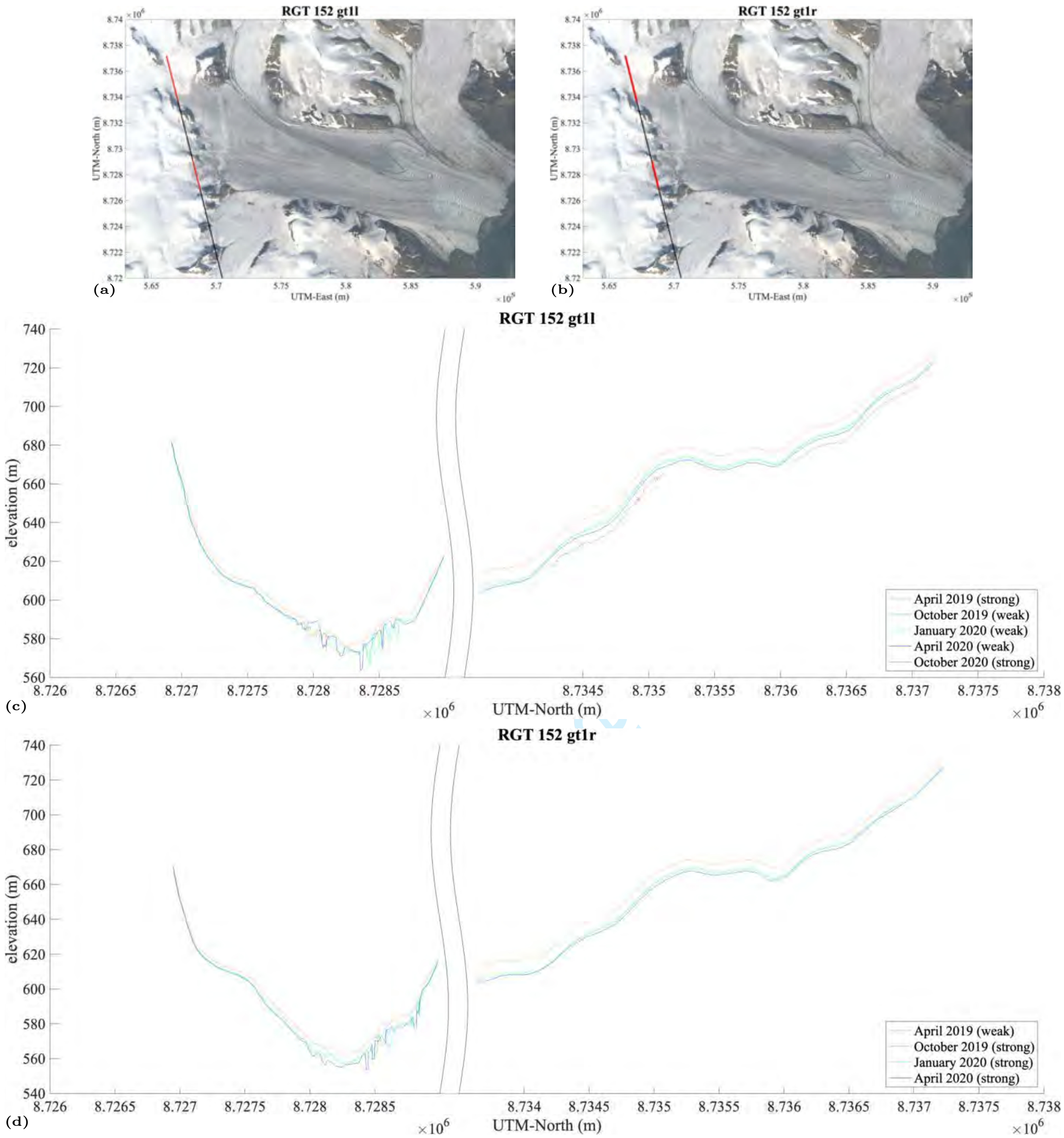

Figure 5: **ICESat-2/DDA-ice surface height time series for RGT 152 beam pair 1 over Negribreen, 2019-2020.** (a) Location of RGT 152 gt1l segment over Negribreen, (b) Location of RGT 152 gt1r segment over Negribreen, (c) surface height time series of RGT 152 gt1l, and (d) surface height time series of RGT 152 gt1r.

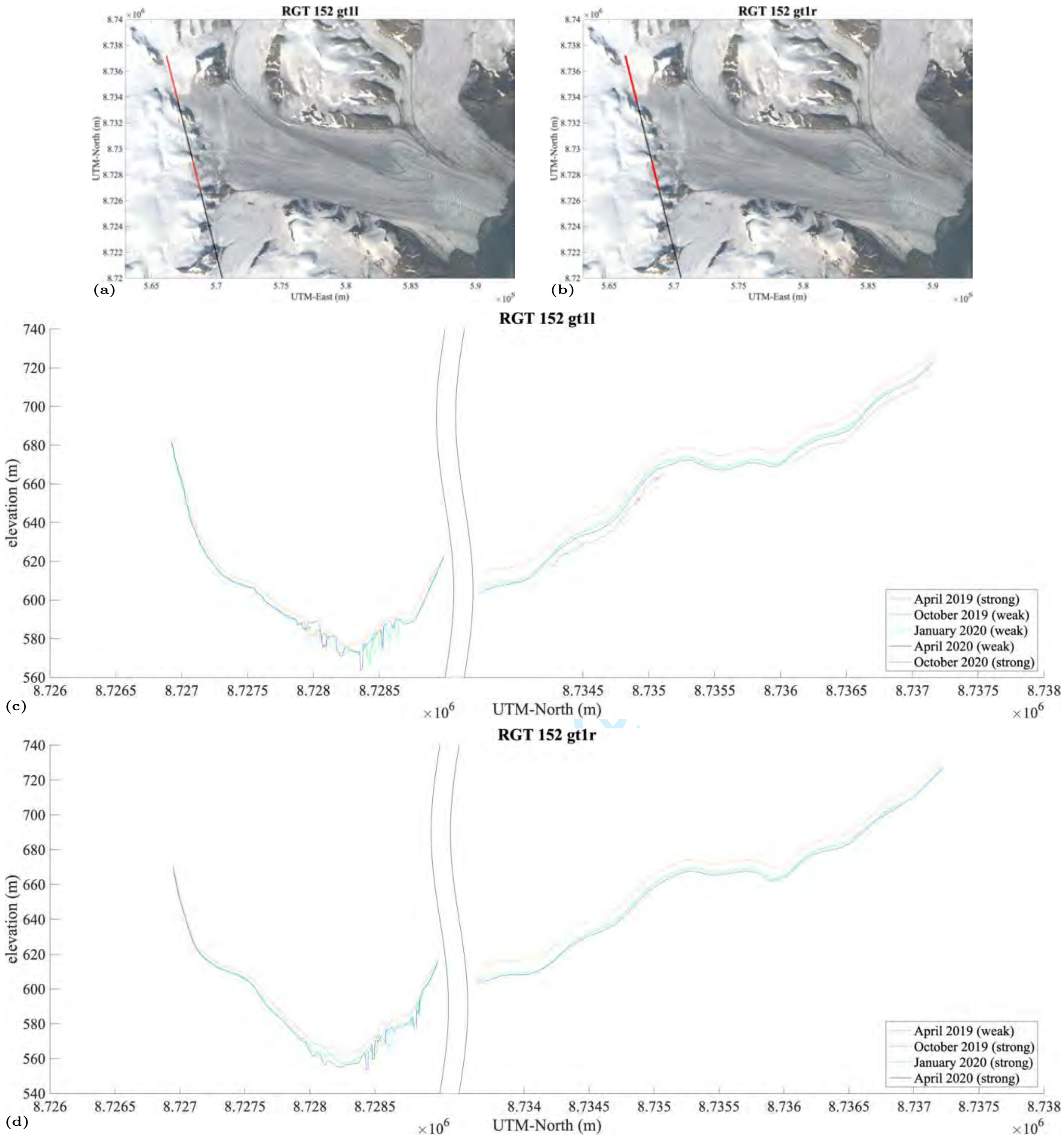

Figure 6: **ICESat-2/DDA-ice surface height time series for RGT 152 beam pair 2 over Negribreen, 2019-2020.** (a) Location of RGT 152 gt2l segment over Negribreen, (b) Location of RGT 152 gt2r segment over Negribreen, (c) surface height time series of RGT 152 gt2l, and (d) surface height time series of RGT 152 gt2r.

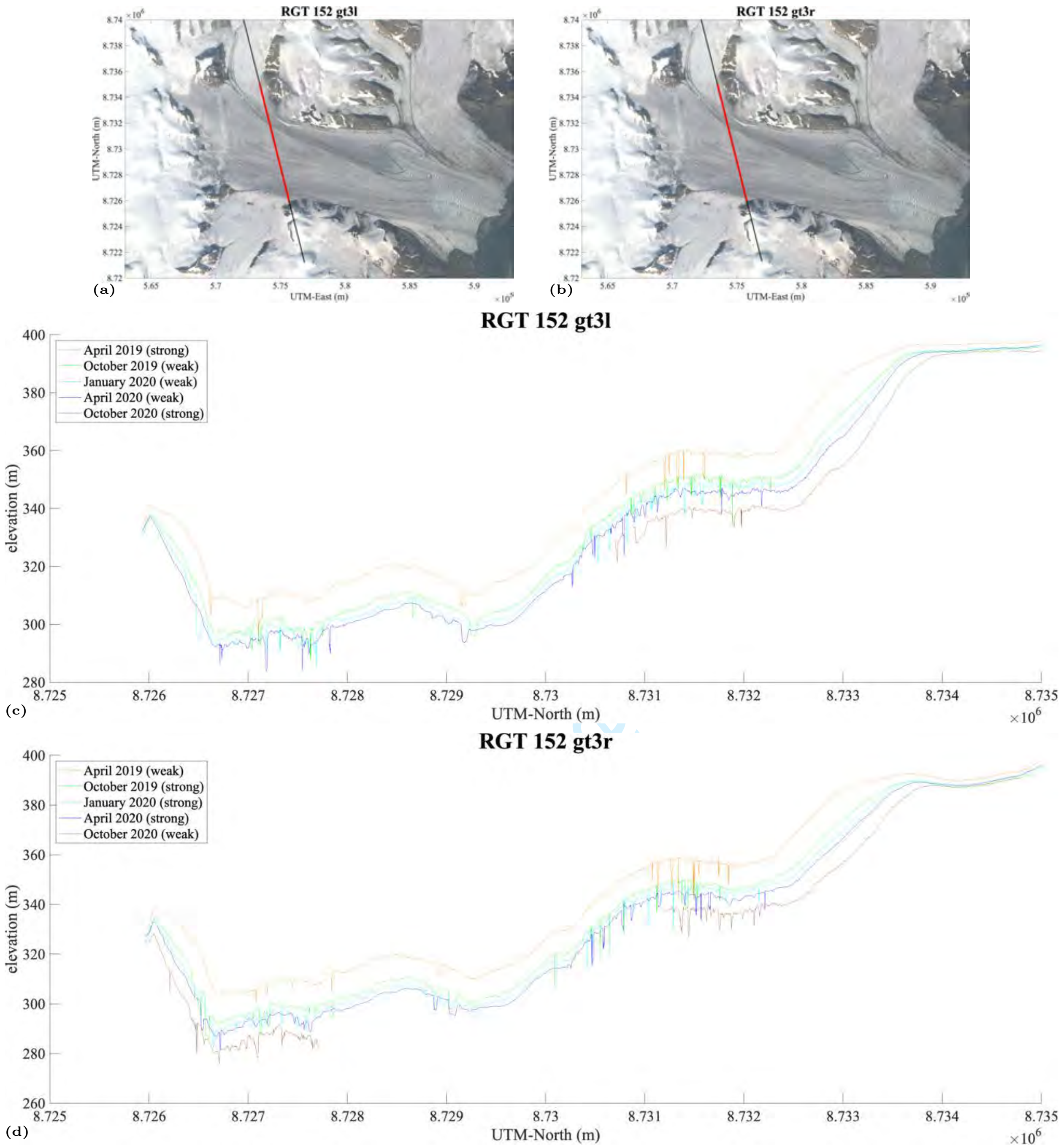

Figure 7: **ICESat-2/DDA-ice surface height time series for RGT 152 beam pair 3 over Negribreen, 2019-2020.** (a) Location of RGT 152 gt3l segment over Negribreen, (b) Location of RGT 152 gt3r segment over Negribreen, (c) surface height time series of RGT 152 gt3l, and (d) surface height time series of RGT 152 gt3r.

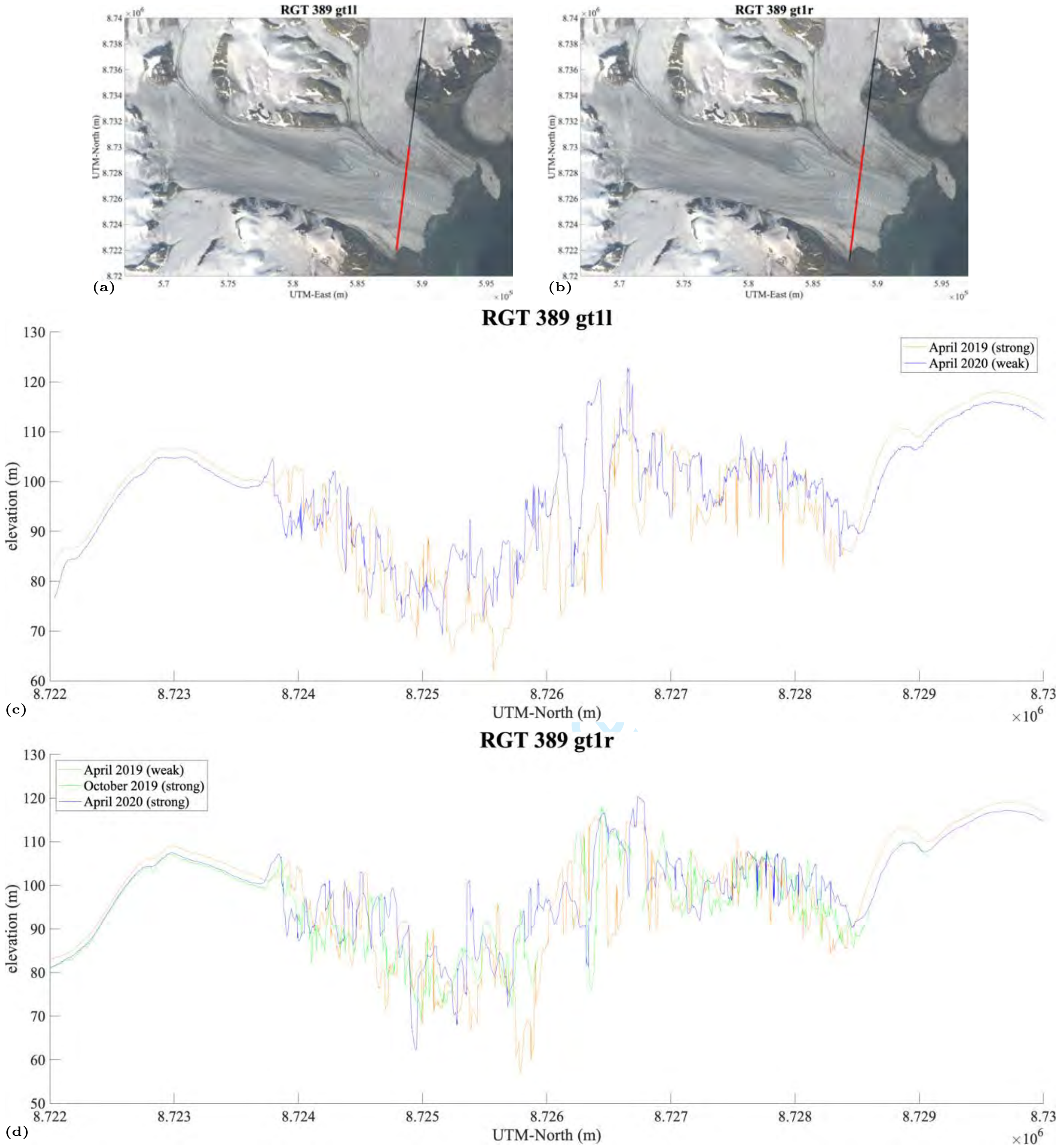

Figure 8: **ICESat-2/DDA-ice surface height time series for RGT 389 beam pair 1 over Negribreen, 2019-2020.** (a) Location of RGT 389 gt1l segment over Negribreen, (b) Location of RGT 389 gt1r segment over Negribreen, (c) surface height time series of RGT 389 gt1l, and (d) surface height time series of RGT 389 gt1r.

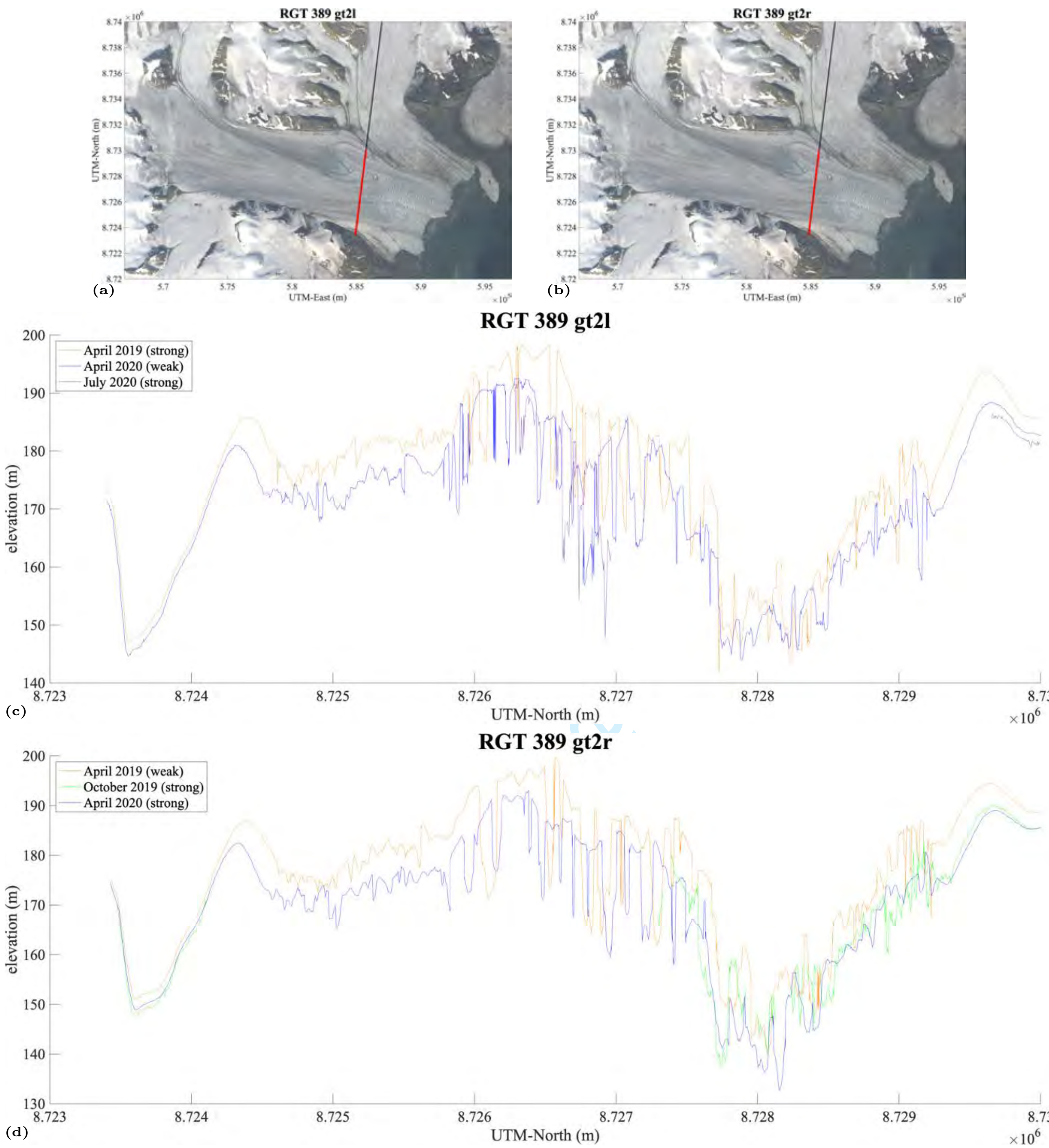

Figure 9: **ICESat-2/DDA-ice surface height time series for RGT 389 beam pair 2 over Negribreen, 2019-2020.** (a) Location of RGT 389 gt2l segment over Negribreen, (b) Location of RGT 389 gt2r segment over Negribreen, (c) surface height time series of RGT 389 gt2l, and (d) surface height time series of RGT 389 gt2r.

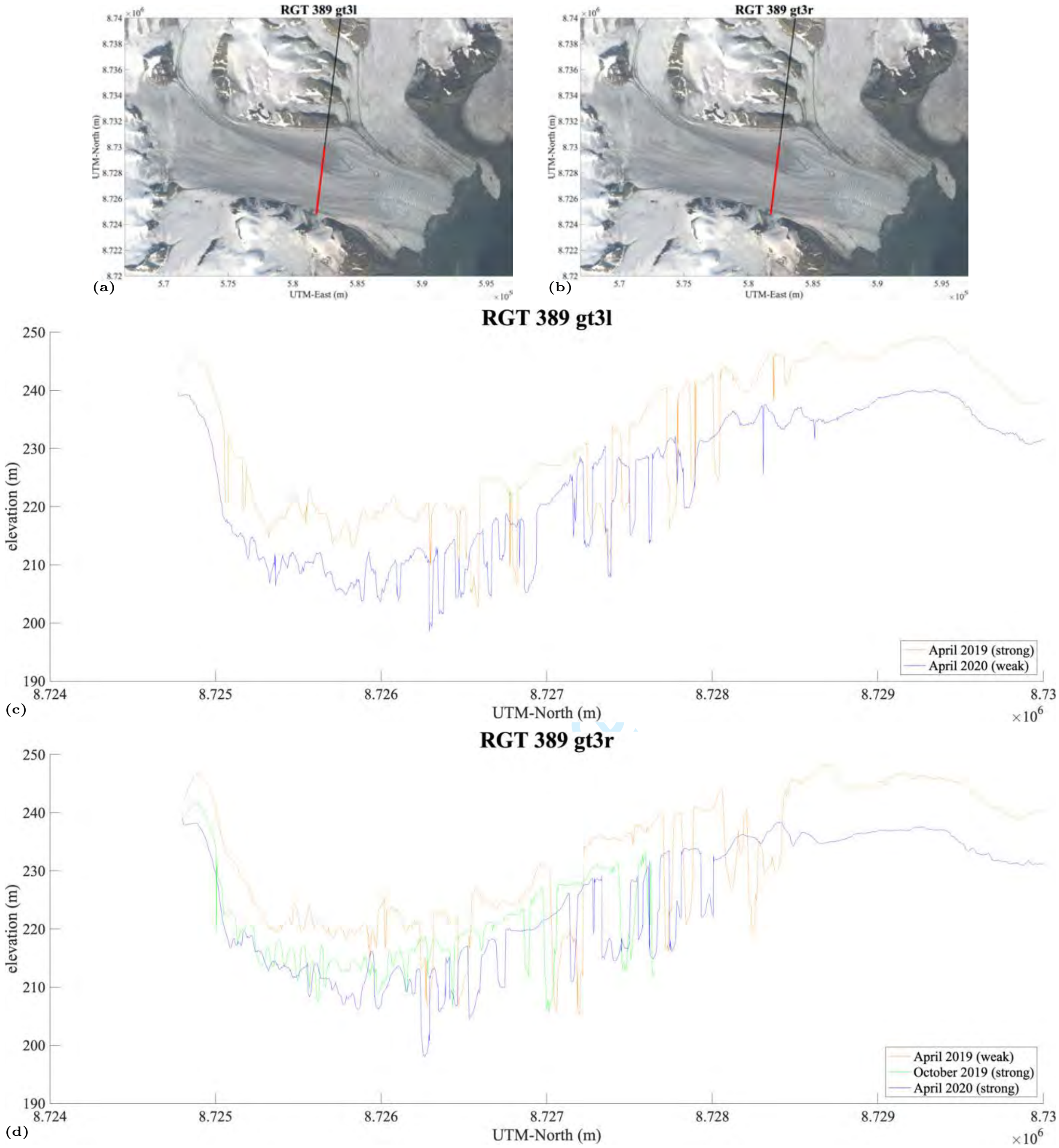

Figure 10: **ICESat-2/DDA-ice surface height time series for RGT 389 beam pair 3 over Negribreen, 2019-2020.** (a) Location of RGT 389 gt3l segment over Negribreen, (b) Location of RGT 389 gt3r segment over Negribreen, (c) surface height time series of RGT 389 gt3l, and (d) surface height time series of RGT 389 gt3r.

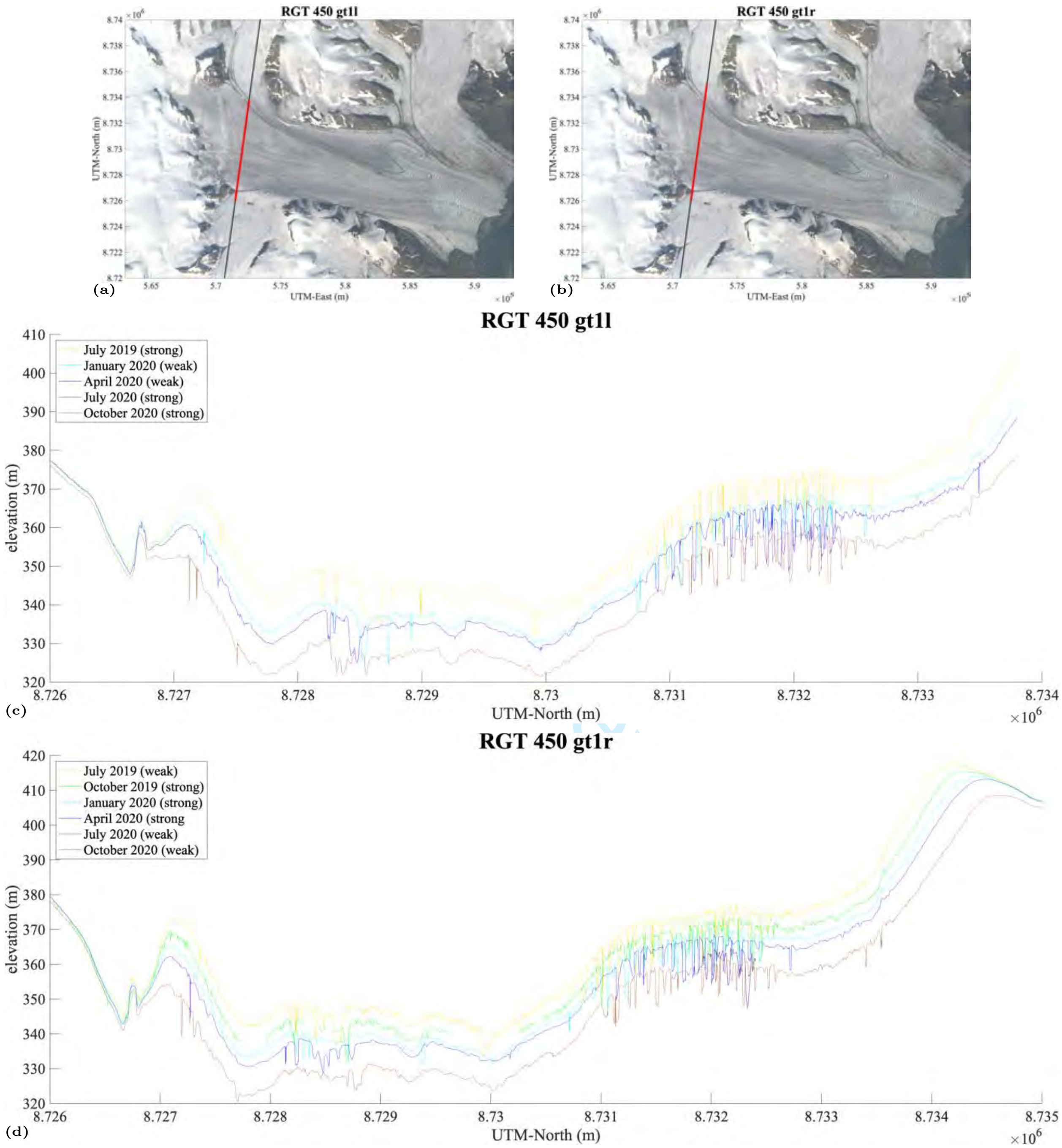

Figure 11: **ICESat-2/DDA-ice surface height time series for RGT 450 beam pair 1 over Negribreen, 2019-2020.** (a) Location of RGT 450 gt1l segment over Negribreen, (b) Location of RGT 450 gt1r segment over Negribreen, (c) surface height time series of RGT 450 gt1l, and (d) surface height time series of RGT 450 gt1r.

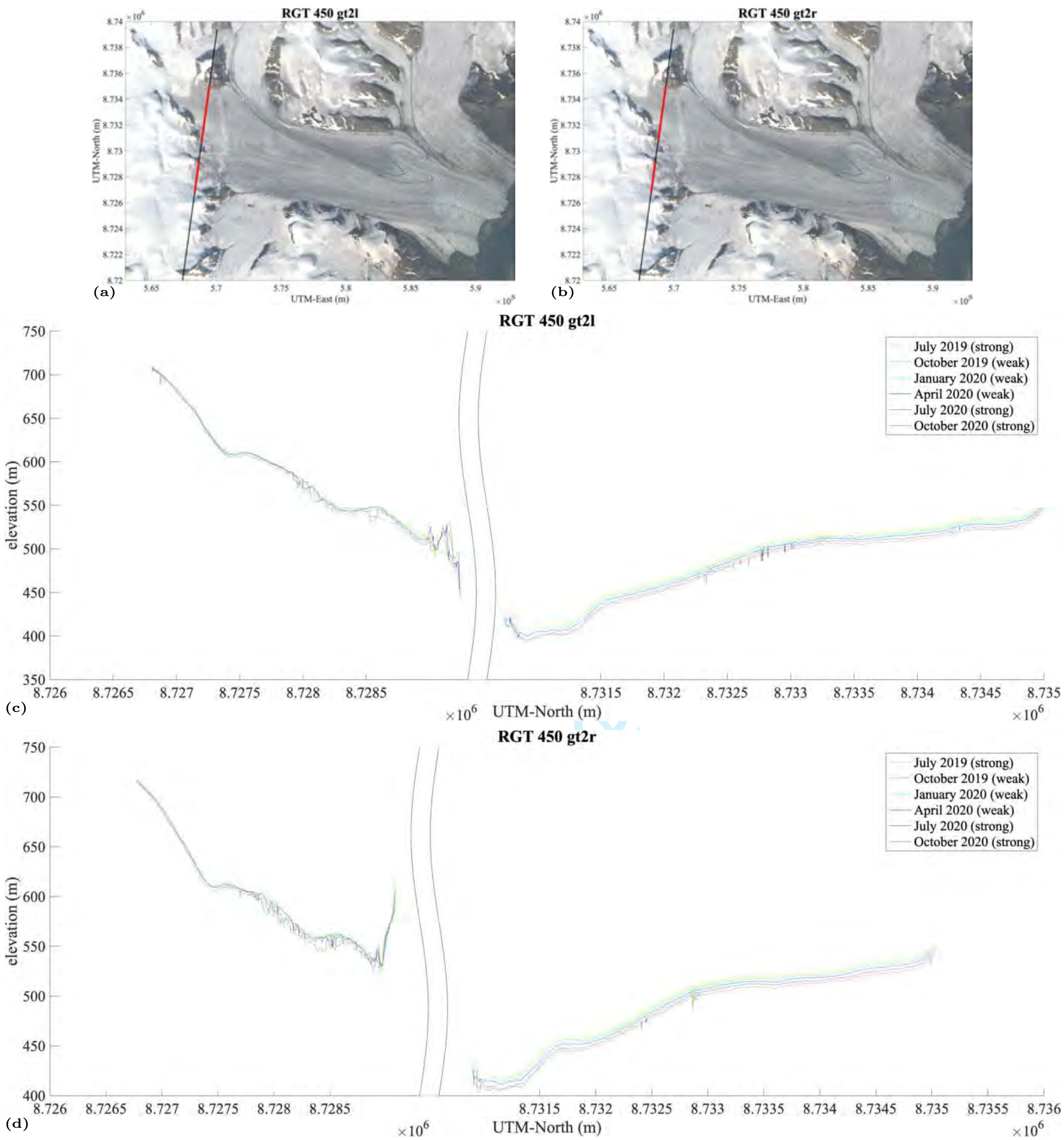

Figure 12: **ICESat-2/DDA-ice surface height time series for RGT 450 beam pair 2 over Negribreen, 2019-2020.** (a) Location of RGT 450 gt2l segment over Negribreen, (b) Location of RGT 450 gt2r segment over Negribreen, (c) surface height time series of RGT 450 gt2l, and (d) surface height time series of RGT 450 gt2r.

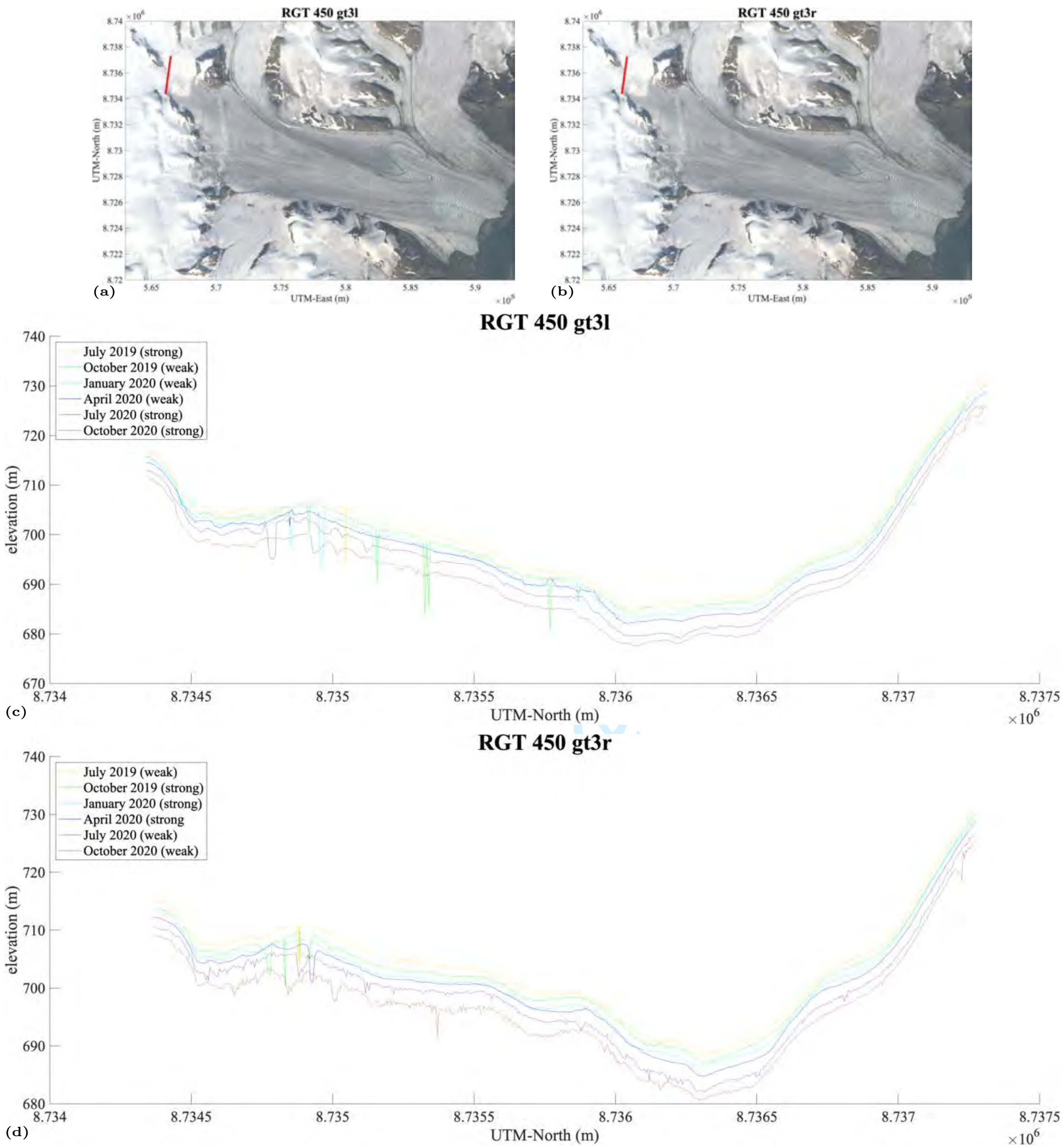

Figure 13: **ICESat-2/DDA-ice surface height time series for RGT 450 beam pair 3 over Negribreen, 2019-2020.** (a) Location of RGT 450 gt3l segment over Negribreen, (b) Location of RGT 450 gt3r segment over Negribreen, (c) surface height time series of RGT 450 gt3l, and (d) surface height time series of RGT 450 gt3r.

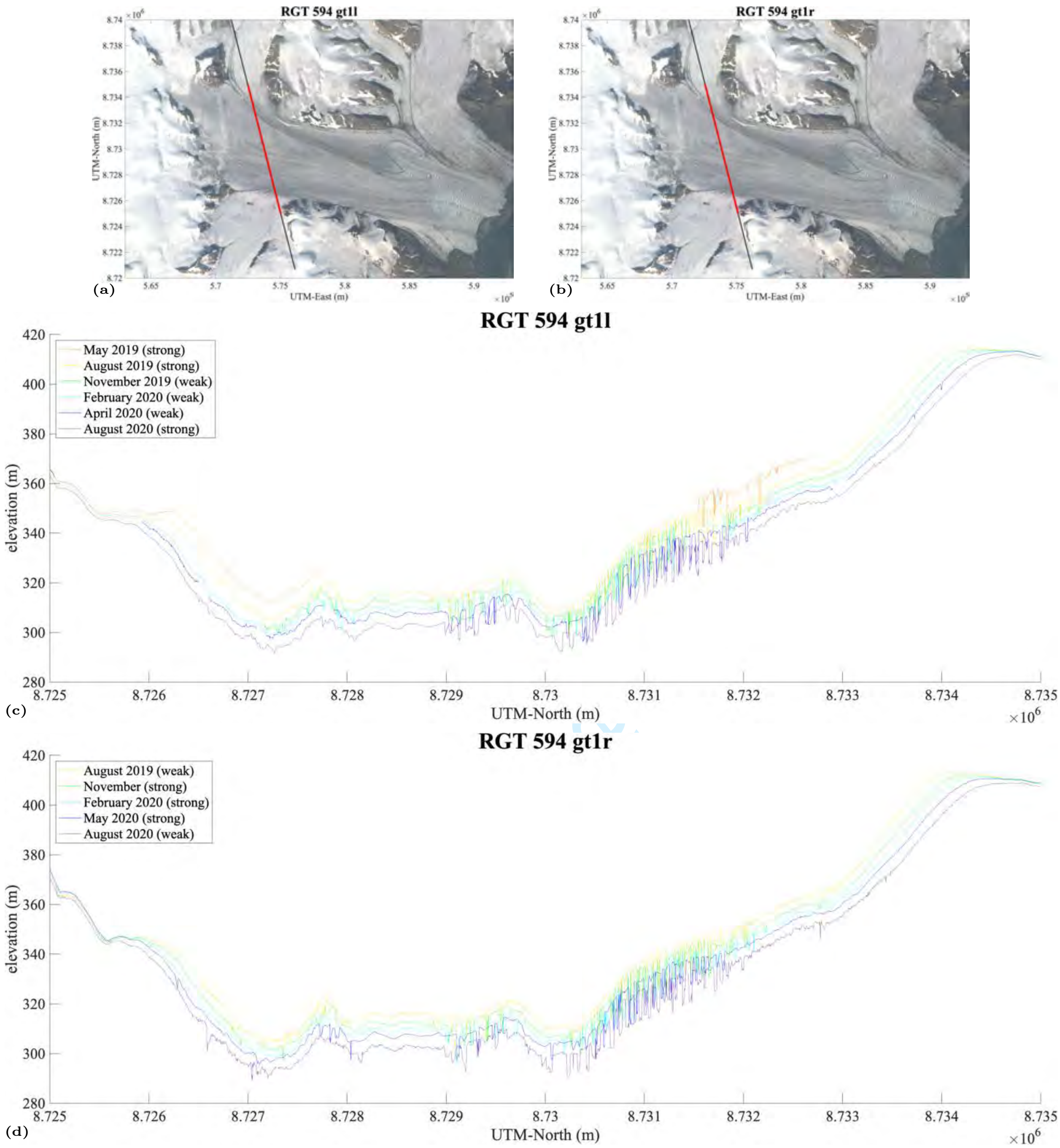

Figure 14: **ICESat-2/DDA-ice surface height time series for RGT 594 beam pair 1 over Negribreen, 2019-2020.** (a) Location of RGT 594 gt1l segment over Negribreen, (b) Location of RGT 594 gt1r segment over Negribreen, (c) surface height time series of RGT 594 gt1l, and (d) surface height time series of RGT 594 gt1r.

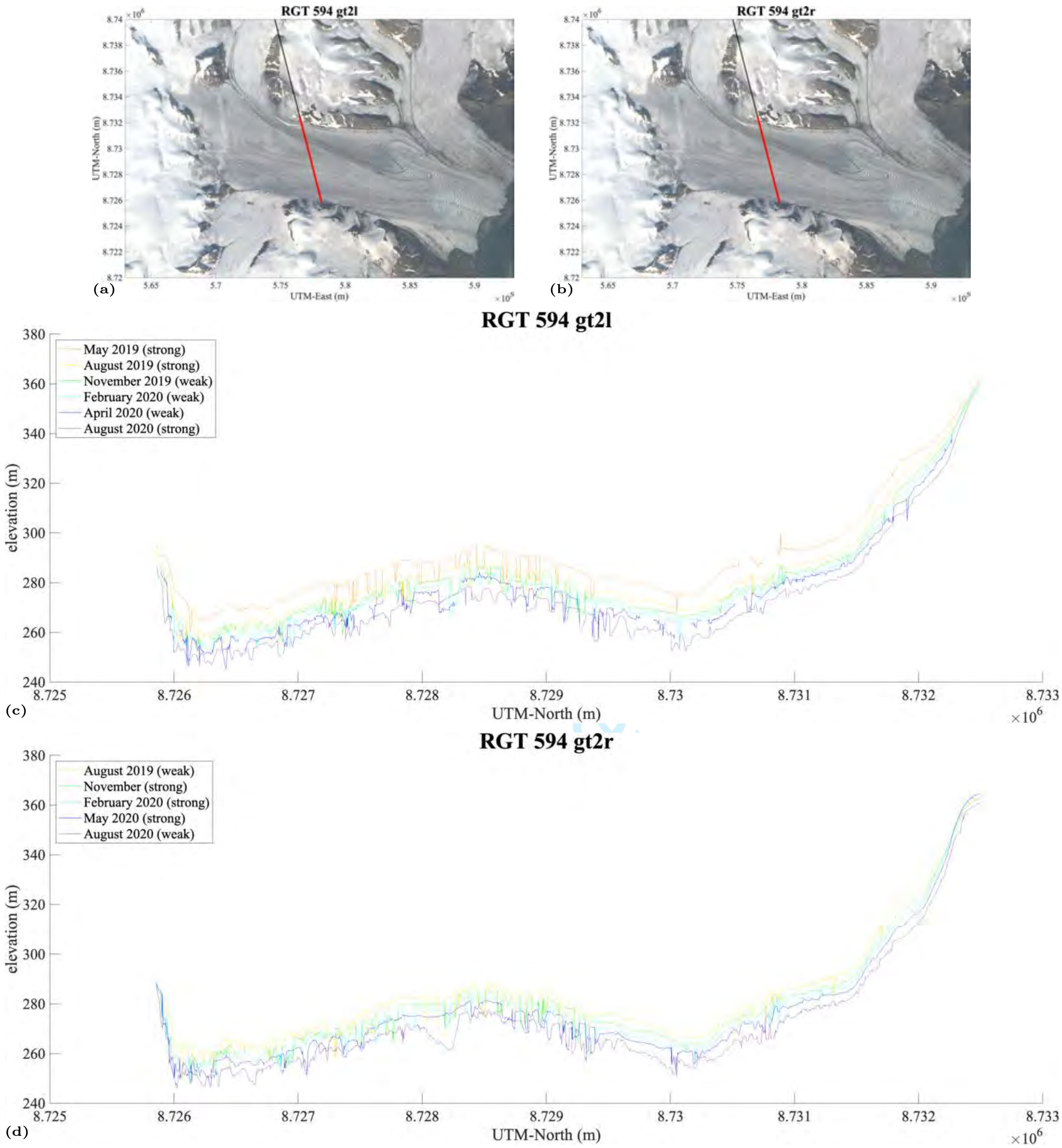

Figure 15: **ICESat-2/DDA-ice surface height time series for RGT 594 beam pair 2 over Negribreen, 2019-2020.** (a) Location of RGT 594 gt2l segment over Negribreen, (b) Location of RGT 594 gt2r segment over Negribreen, (c) surface height time series of RGT 594 gt2l, and (d) surface height time series of RGT 594 gt2r.

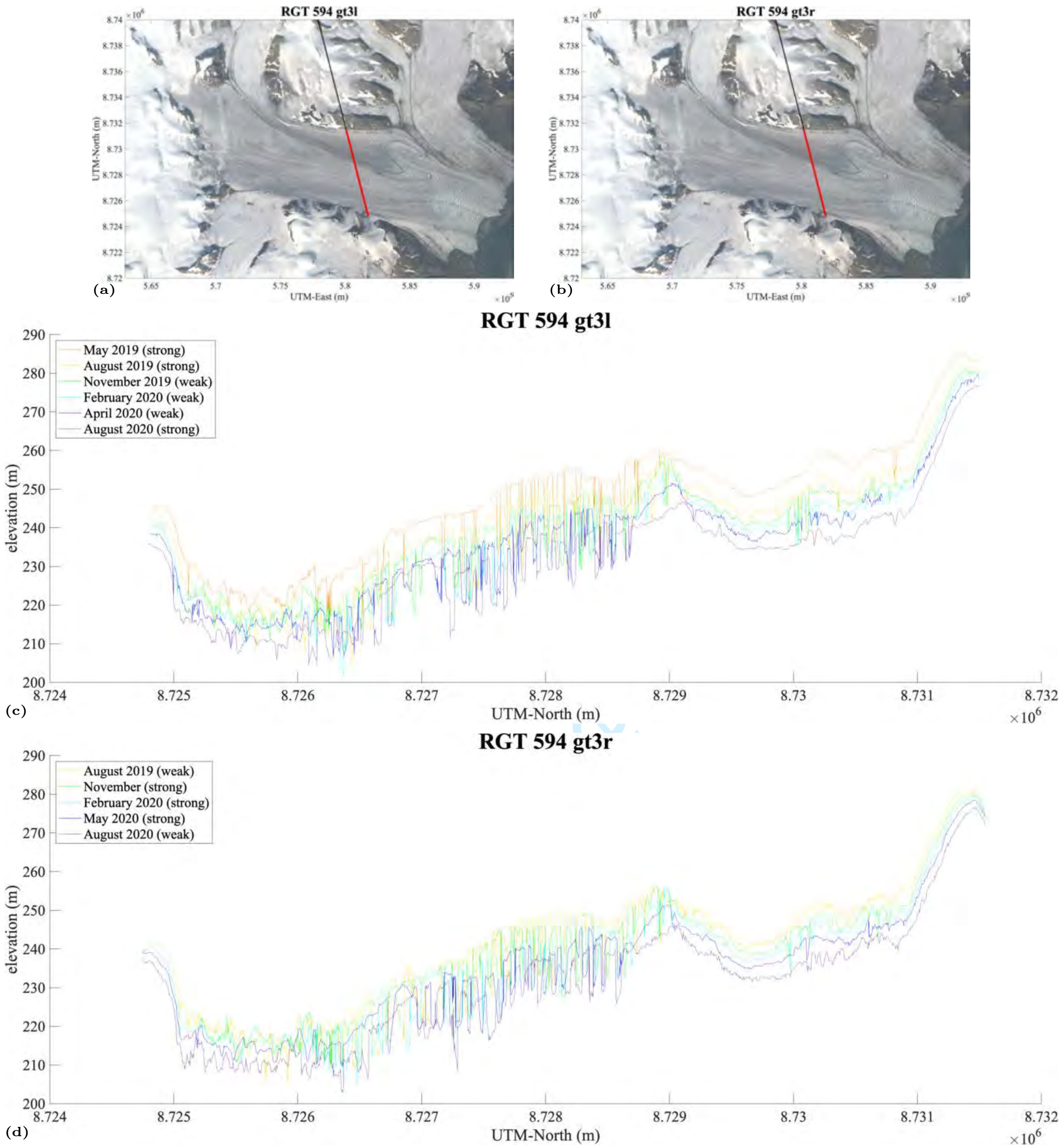

Figure 16: **ICESat-2/DDA-ice surface height time series for RGT 594 beam pair 3 over Negribreen, 2019-2020.** (a) Location of RGT 594 gt3l segment over Negribreen, (b) Location of RGT 594 gt3r segment over Negribreen, (c) surface height time series of RGT 594 gt3l, and (d) surface height time series of RGT 594 gt3r.

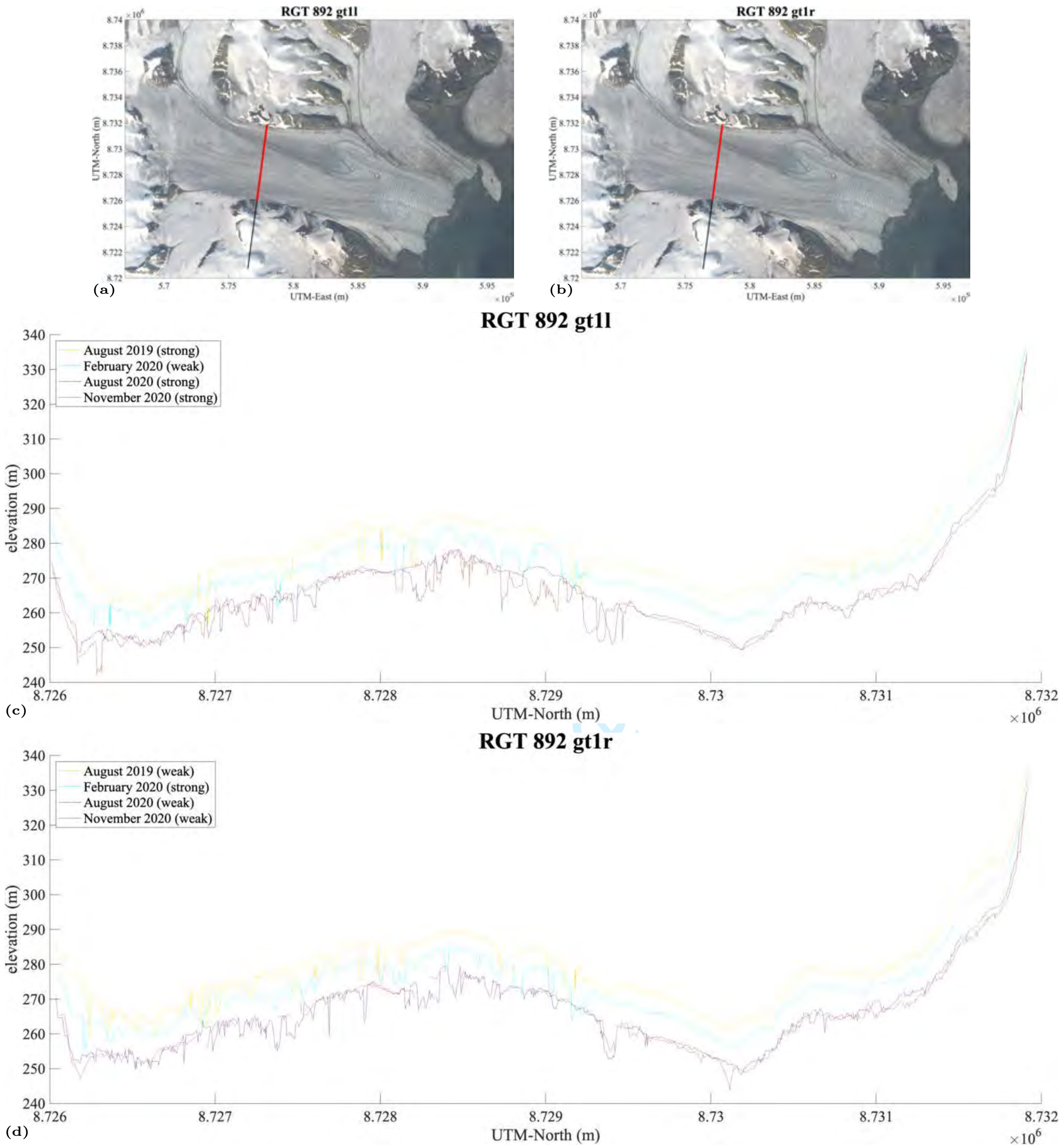

Figure 17: **ICESat-2/DDA-ice surface height time series for RGT 892 beam pair 1 over Negribreen, 2019-2020.** (a) Location of RGT 892 gt1l segment over Negribreen, (b) Location of RGT 892 gt1r segment over Negribreen, (c) surface height time series of RGT 892 gt1l, and (d) surface height time series of RGT 892 gt1r.

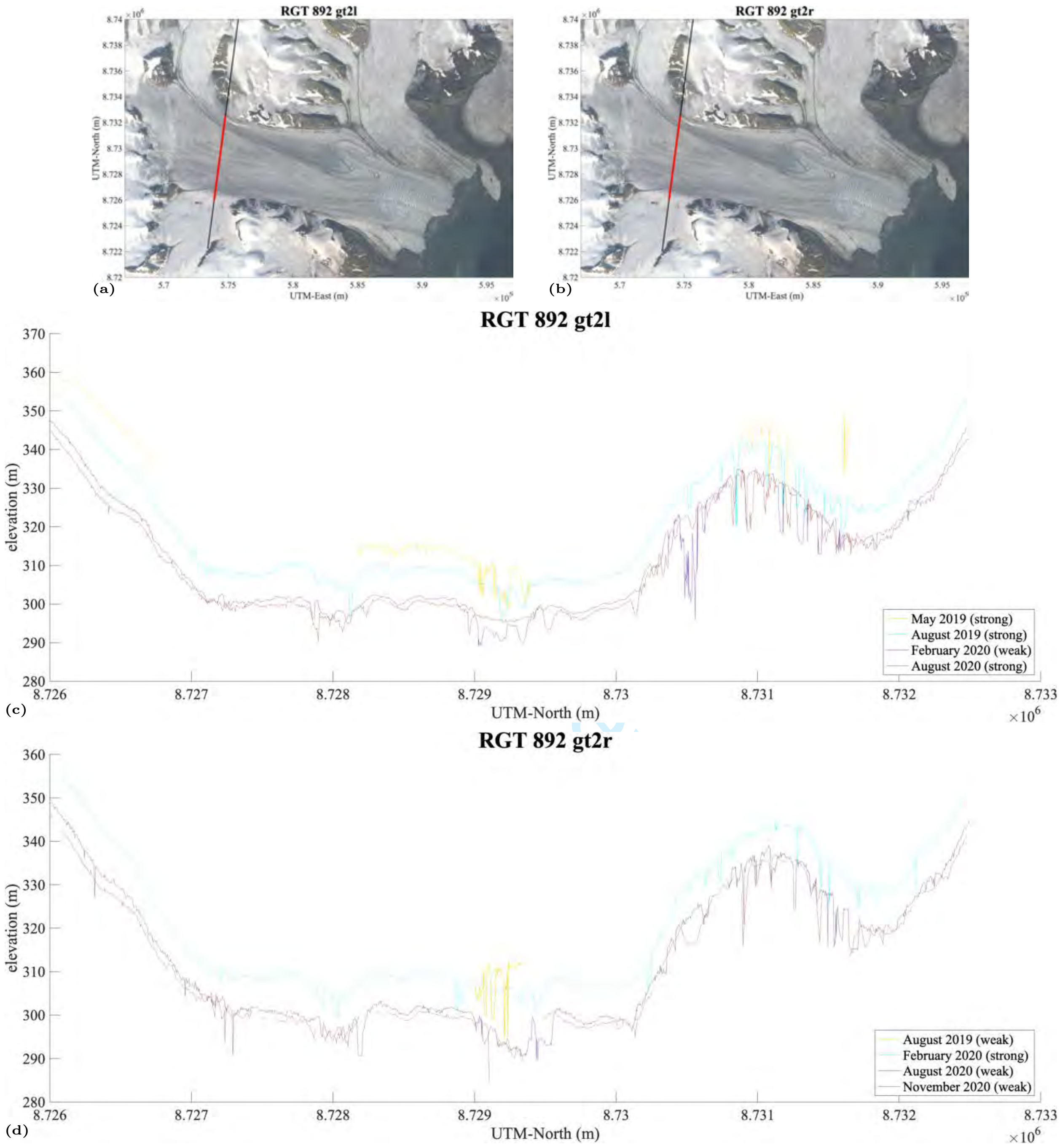

Figure 18: **ICESat-2/DDA-ice surface height time series for RGT 892 beam pair 2 over Negribreen, 2019-2020.** (a) Location of RGT 892 gt2l segment over Negribreen, (b) Location of RGT 892 gt2r segment over Negribreen, (c) surface height time series of RGT 892 gt2l, and (d) surface height time series of RGT 892 gt2r.

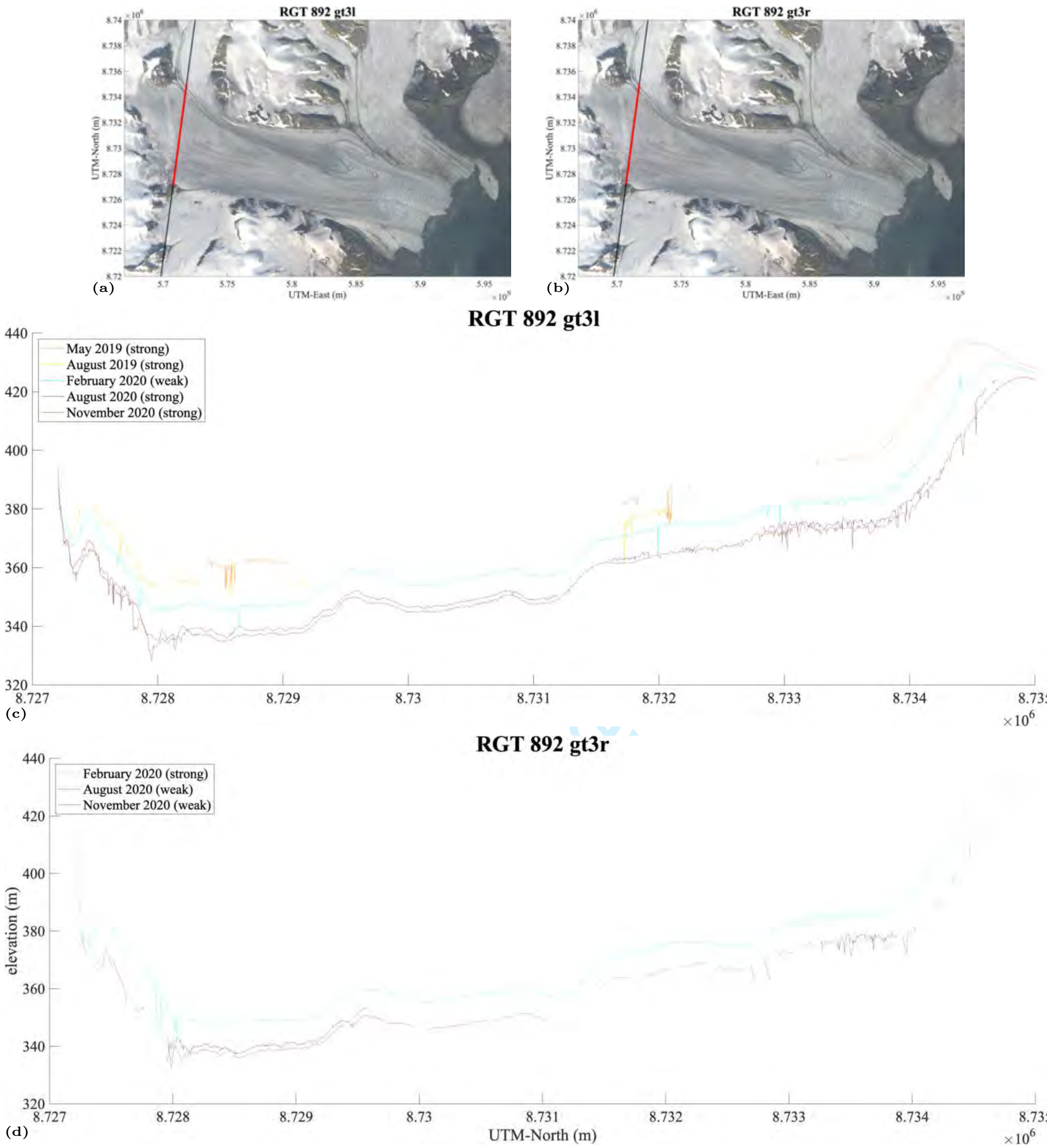

Figure 19: **ICESat-2/DDA-ice surface height time series for RGT 892 beam pair 3 over Negribreen, 2019-2020.** (a) Location of RGT 892 gt3l segment over Negribreen, (b) Location of RGT 892 gt3r segment over Negribreen, (c) surface height time series of RGT 892 gt3l, and (d) surface height time series of RGT 892 gt3r.

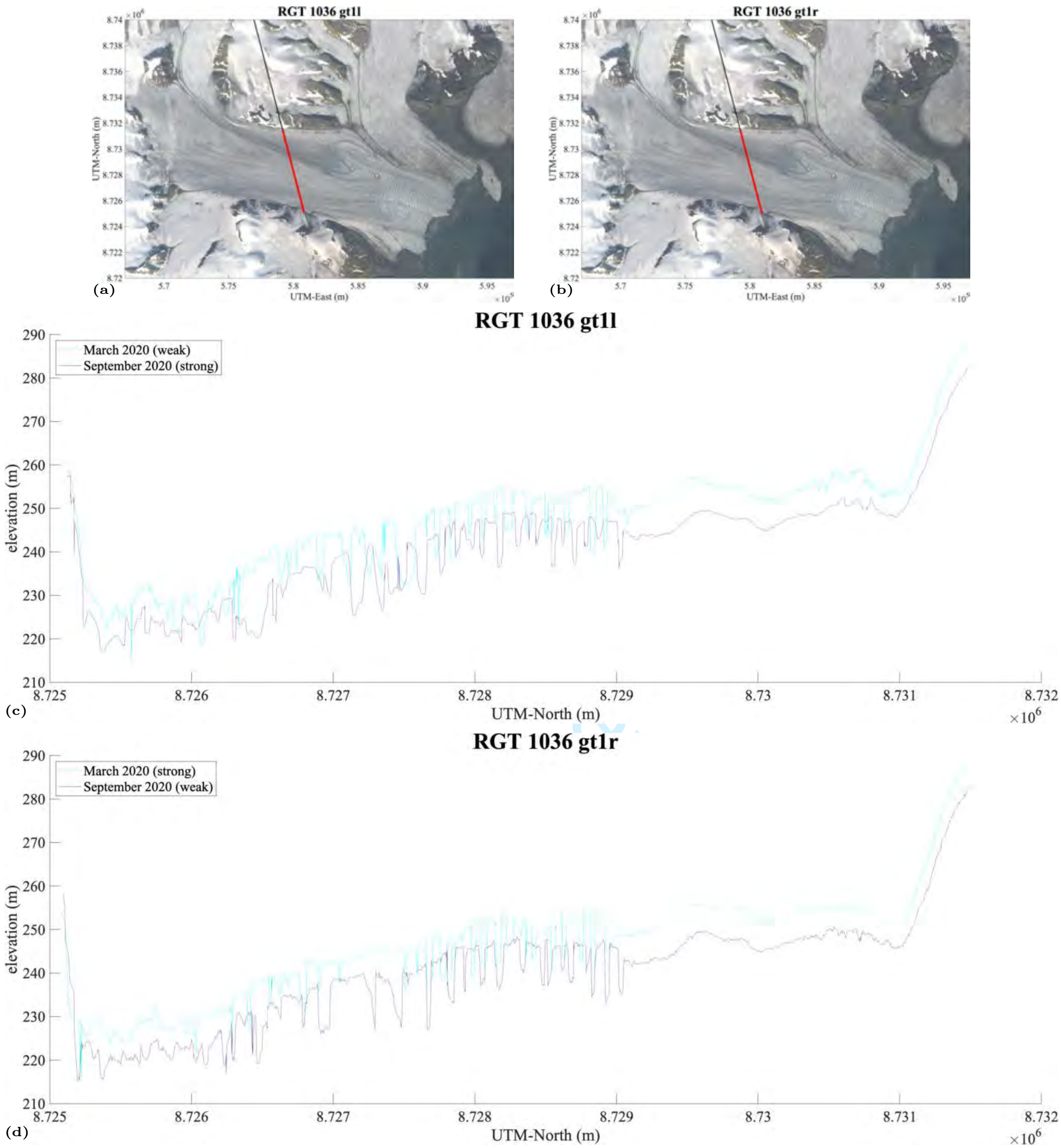

Figure 20: **ICESat-2/DDA-ice surface height time series for RGT 1036 beam pair 1 over Negribreen, 2019-2020.** (a) Location of RGT 1036 gt1l segment over Negribreen, (b) Location of RGT 1036 gt1r segment over Negribreen, (c) surface height time series of RGT 1036 gt1l, and (d) surface height time series of RGT 1036 gt1r.

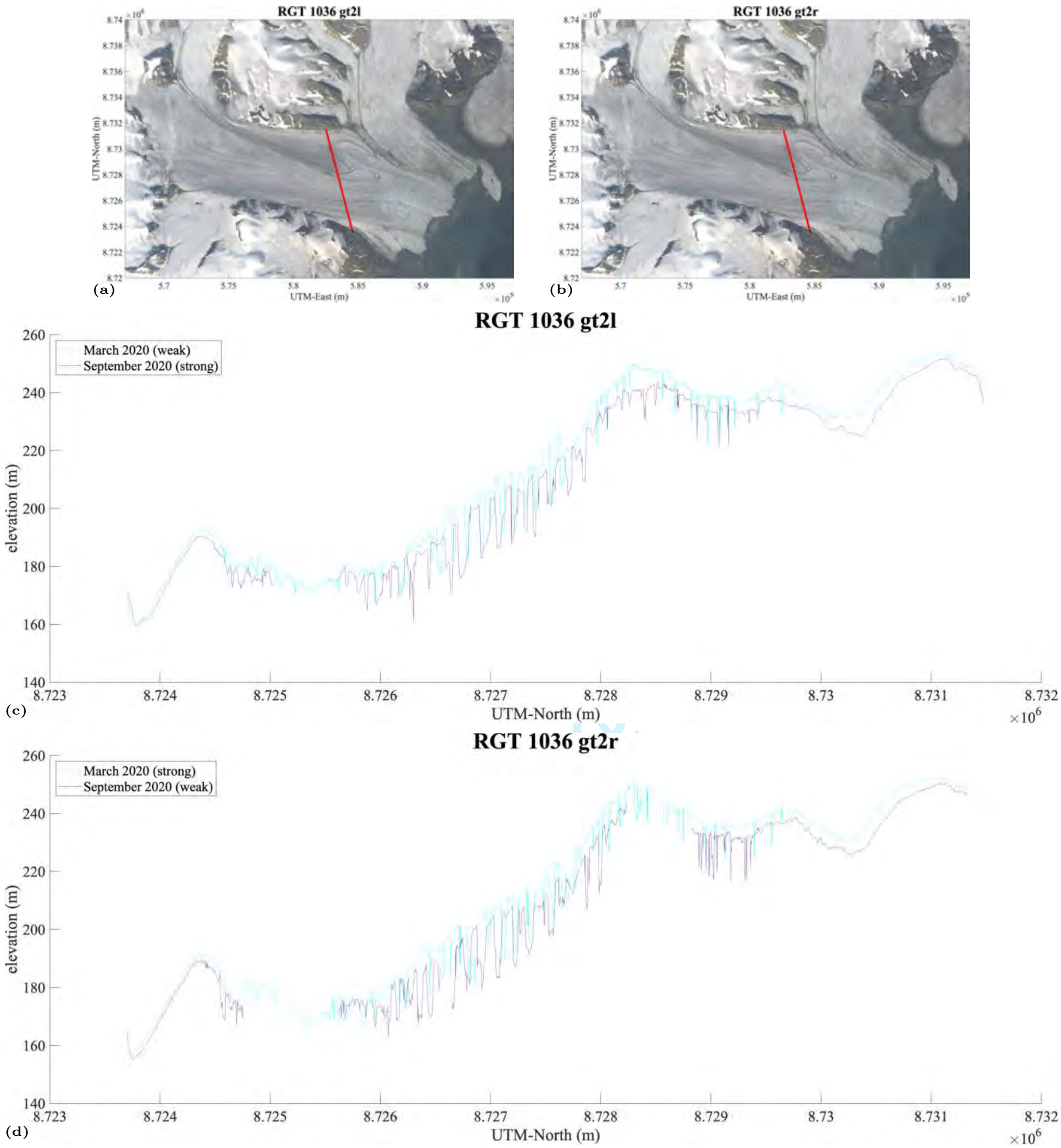

Figure 21: **ICESat-2/DDA-ice surface height time series for RGT 1036 beam pair 2 over Negribreen, 2019-2020.** (a) Location of RGT 1036 gt2l segment over Negribreen, (b) Location of RGT 1036 gt2r segment over Negribreen, (c) surface height time series of RGT 1036 gt2l, and (d) surface height time series of RGT 1036 gt2r.

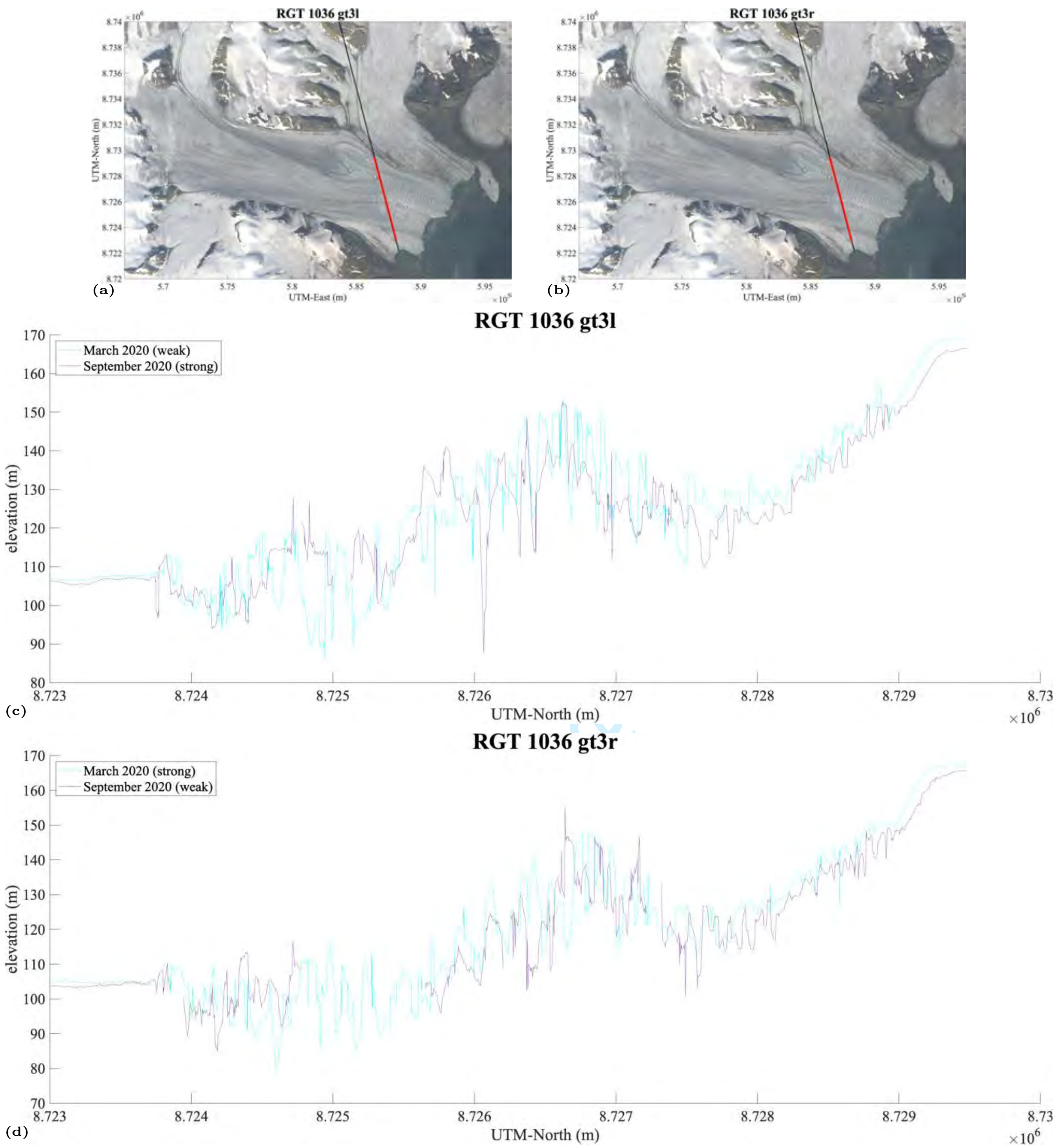

Figure 22: **ICESat-2/DDA-ice surface height time series for RGT 1036 beam pair 3 over Negribreen, 2019-2020.** (a) Location of RGT 1036 gt3l segment over Negribreen, (b) Location of RGT 1036 gt3r segment over Negribreen, (c) surface height time series of RGT 1036 gt3l, and (d) surface height time series of RGT 1036 gt3r.

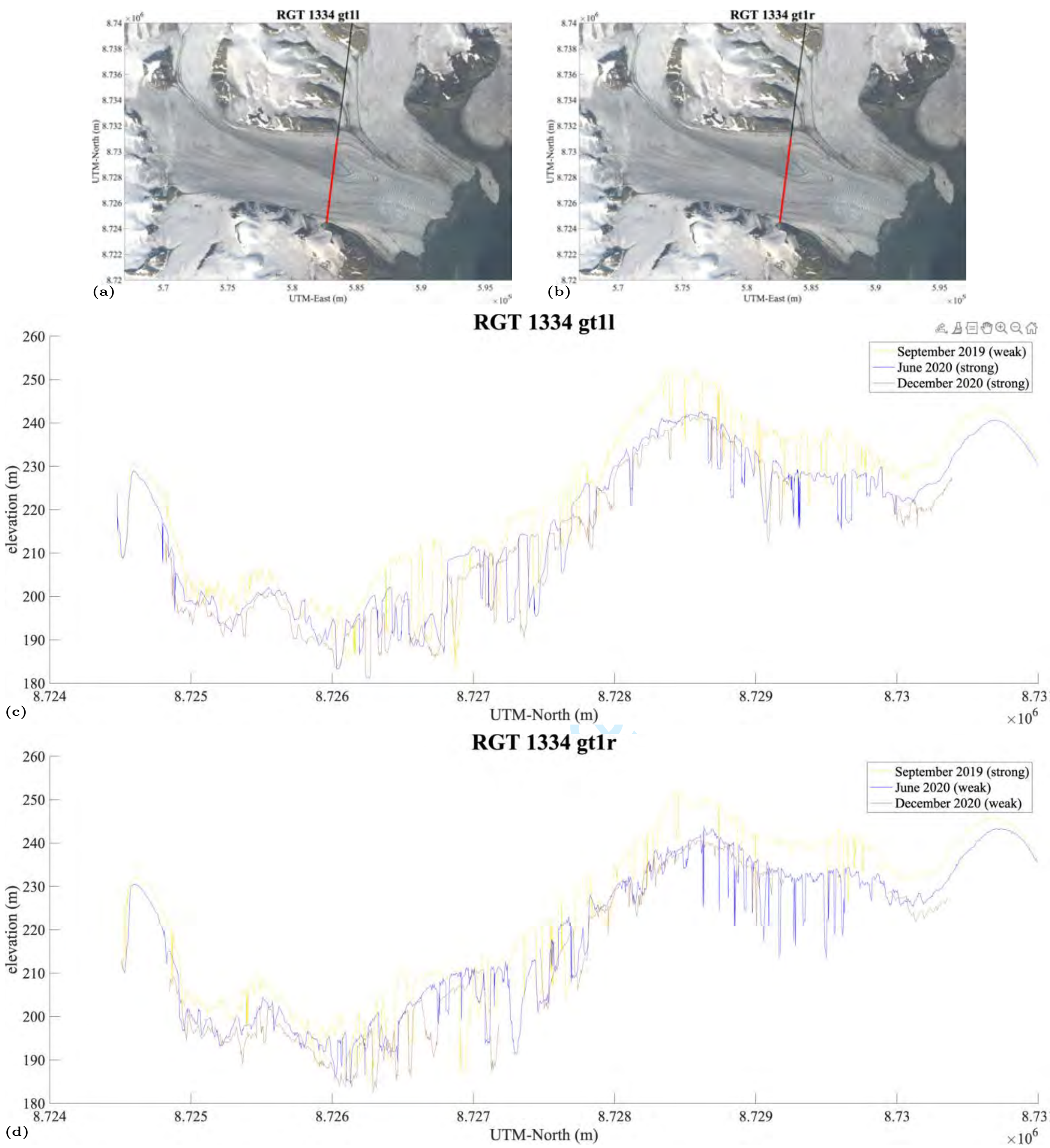

Figure 23: **ICESat-2/DDA-ice surface height time series for RGT 1334 beam pair 1 over Negribreen, 2019-2020.** (a) Location of RGT 1334 gt1l segment over Negribreen, (b) Location of RGT 1334 gt1r segment over Negribreen, (c) surface height time series of RGT 1334 gt1l, and (d) surface height time series of RGT 1334 gt1r.

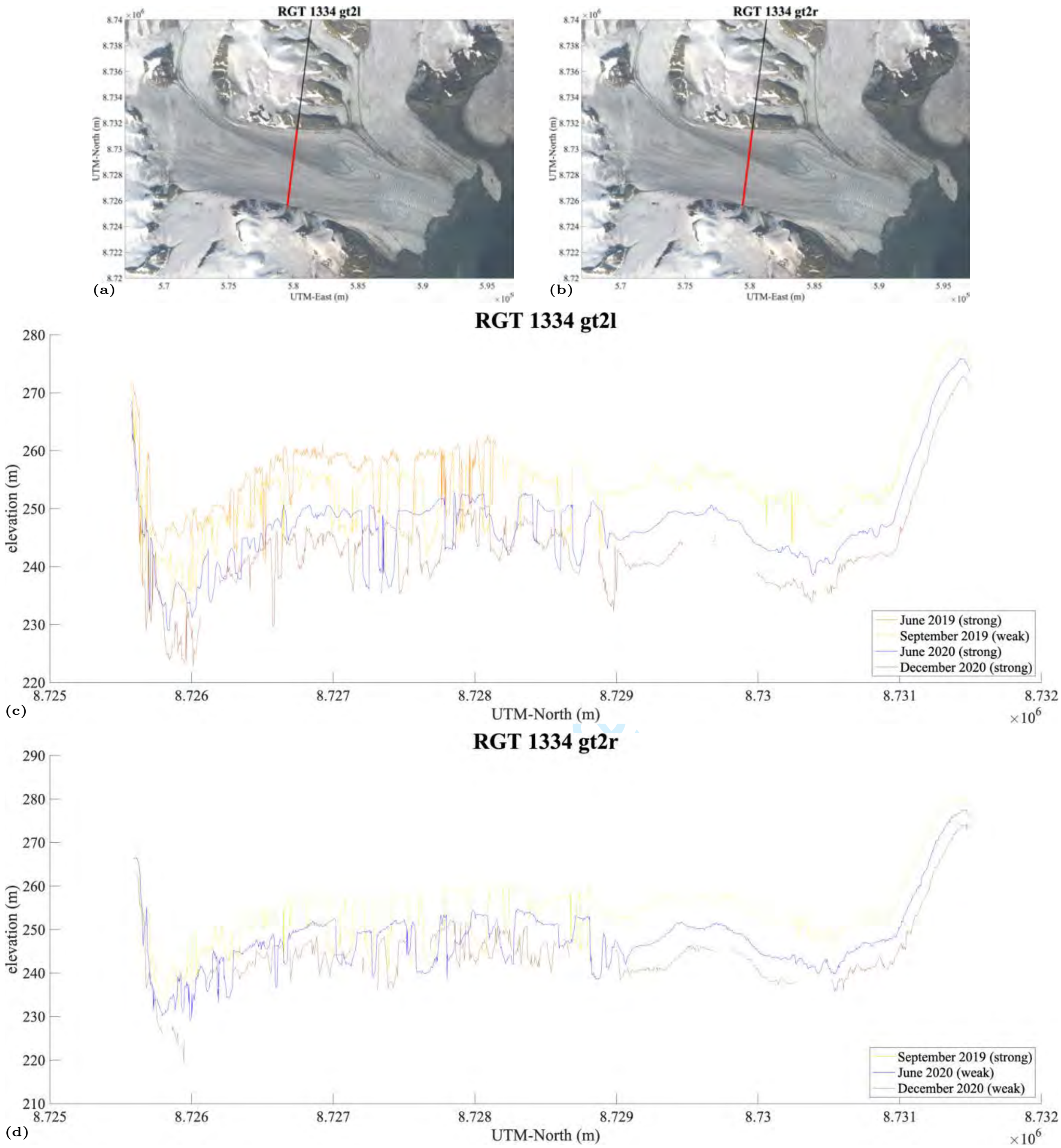

Figure 24: **ICESat-2/DDA-ice surface height time series for RGT 1334 beam pair 2 over Negribreen, 2019-2020.** (a) Location of RGT 1334 gt2l segment over Negribreen, (b) Location of RGT 1334 gt2r segment over Negribreen, (c) surface height time series of RGT 1334 gt2l, and (d) surface height time series of RGT 1334 gt2r.

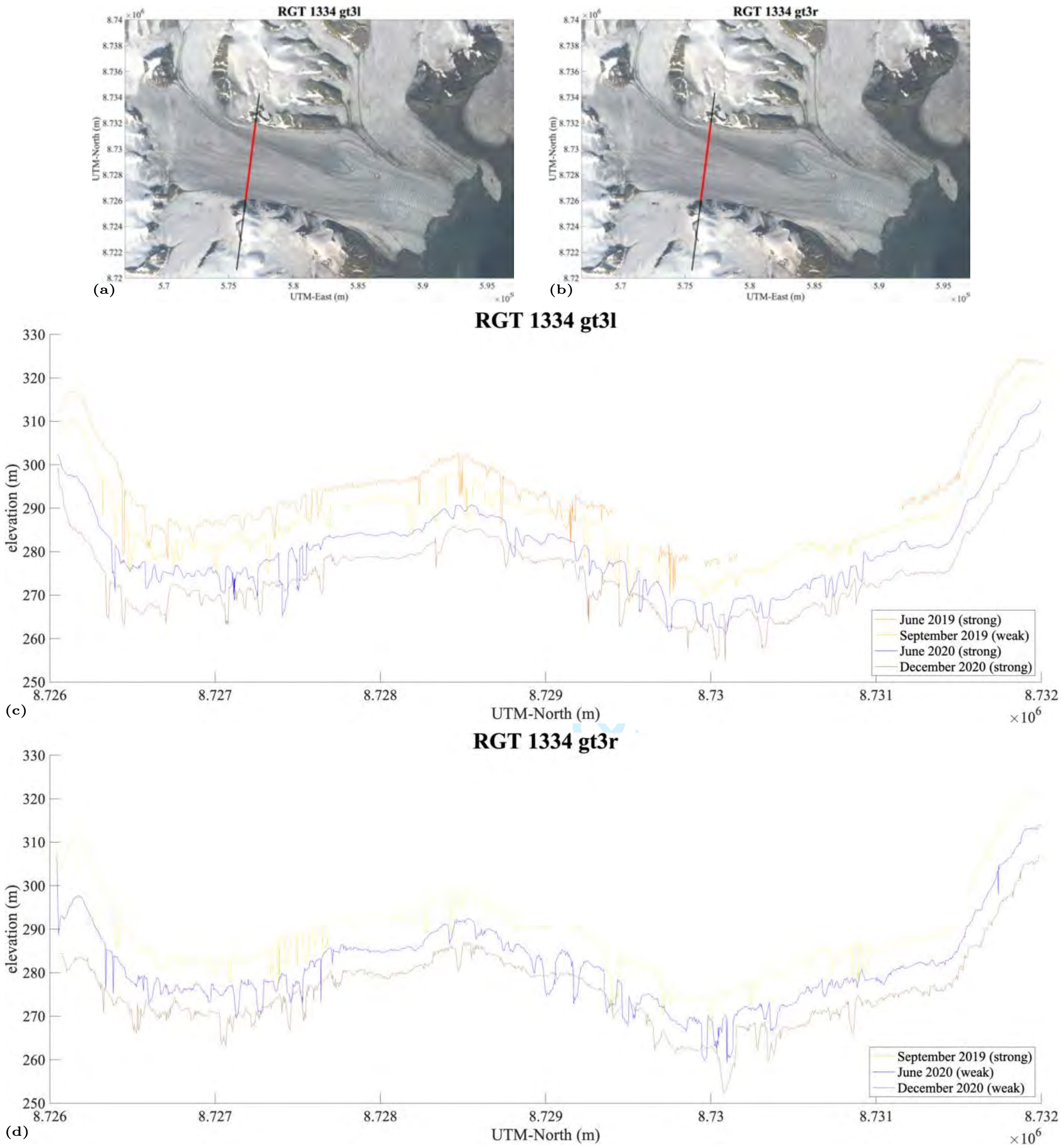

Figure 25: **ICESat-2/DDA-ice surface height time series for RGT 1334 beam pair 3 over Negribreen, 2019-2020.** (a) Location of RGT 1334 gt3l segment over Negribreen, (b) Location of RGT 1334 gt3r segment over Negribreen, (c) surface height time series of RGT 1334 gt3l, and (d) surface height time series of RGT 1334 gt3r.